

**SLICING THE EARTH:
A layer-stripping method employing a
causality-based imaging condition**

PROEFSCHRIFT

ter verkrijging van de graad van doctor
aan de Technische Universiteit Delft,
op gezag van de Rector Magnificus prof. dr. ir. J.T. Fokkema,
voorzitter van het College voor Promoties,
in het openbaar te verdedigen op dinsdag 17 mei 2004 om 15.30 uur

door

Hedi POOT

mijnbouwkundig ingenieur
geboren te Vlaardingen

Dit proefschrift is goedgekeurd door de promotoren:

Prof. dr. ir. J.T. Fokkema

Prof. dr. ir. C.P.A. Wapenaar

Samenstelling promotiecommissie:

Rector Magnificus	Voorzitter
Prof. dr. ir. J.T. Fokkema	Technische Universiteit Delft, promotor
Prof. dr. ir. C.P.A. Wapenaar	Technische Universiteit Delft, promotor
Prof. dr. ir. A. Gisolf	Technische Universiteit Delft
Prof. ir. C.P.J.W. van Kruijsdijk	Technische Universiteit Delft
Prof. dr. R. Klees	Technische Universiteit Delft
Dr. M. Sen	University of Texas, Austin
Dr. ir. E.C. Slob	Technische Universiteit Delft

Published and distributed by: DUP Science

DUP Science is an imprint of
Delft University Press
P.O. Box 98 2600 MG Delft
The Netherlands
Telephone: +31 15 27 85 678
Telefax: + 31 15 27 85 706
E-mail: info@library.tudelft.nl

ISBN 90-407-2490-3

Keywords: Inversion, Lateral heterogeneity, seismic velocities.

Copyright ©2004 by H. Poot, Section of Applied Geophysics, Department of Applied Earth Sciences, Delft University of Technology.

All rights reserved. No parts of this publication may be reproduced, stored in a retrieval system or transmitted, in any form or by any means, electronic, mechanical, photocopying, recording, or otherwise, without the prior written permission of the author.

Cover design by Jeroen Guldemon.

To Renée.

Contents

1	Introduction	1
1.1	Background	1
1.2	Seismic inversion methods	1
1.3	The layer-stripping method in this thesis	3
1.4	Time-lapse seismic monitoring	5
1.5	Outline of the thesis	6
2	Theory	9
2.1	General description	9
2.1.1	The summation convention	9
2.1.2	Acoustic equations in the space-time domain	10
2.1.3	Acoustic equations in the Laplace domain	10
2.1.4	The reciprocity theorem	12
2.2	Layer replacement	13
2.2.1	Theory of layer replacement for general 3D case.	13
2.3	A causality-based imaging condition	21
2.3.1	Derivation of imaging condition for laterally varying 3D media.	21
2.3.2	The layer-stripping procedure	24
3	The one-dimensional case	29
3.1	Theory for the two-dimensional case.	29

3.1.1	A horizontally layered medium.	31
3.2	Theory for the one-dimensional case.	33
3.2.1	Derivation of imaging condition in 1D.	34
4	Evaluation of the one-dimensional case	35
4.1	Results for the 1D-case	35
4.1.1	Implementation of the imaging condition.	35
4.1.2	Wavelet	38
4.1.3	Internal multiples	39
4.1.4	The influence of the thickness of stripped layers	43
4.1.5	The resolution of the method	43
4.1.6	Results for oblique incidence	46
4.2	Comparison to Schur-algorithm	51
4.2.1	The Schur algorithm for the normal incidence problem	51
4.2.2	Comparison of imaging results	52
5	The lack of the lowest frequencies in seismic data	55
5.1	Problem description	55
5.2	The envelope method	60
5.3	The absolute value method	63
5.4	Negative velocity contrasts	66
6	Some applications of the layer-stripping method.	75
6.1	An application in time-lapse seismic imaging	75
6.2	An example for a two-dimensional medium	84
7	Conclusions	91

A Proof of symmetry of pseudo-differential operator	95
B Proposed solution strategy for layer replacement	99
C Mathematical relations: Parseval's theorem and Hilbert transform	107
C.1 Parseval's theorem	107
C.2 The Hilbert transform	108
D The Schur algorithm	109
D.1 Inversion of a layered acoustic medium	109
D.2 Alternative Schur solution	111
Summary	123
Nederlandse Samenvatting	125
Acknowledgments	129
Curriculum Vitae	131

1

Introduction

1.1 Background

Seismic prospecting is one of the major players in the ongoing quest for oil. Sound waves propagating through the subsurface are used to collect information on the structure and material properties of this subsurface. Since the waves travel through many different formations of unknown shape and composition, finding these properties is everything but straightforward. One of the reasons for this is that the problem is not linear. The waves travelling through the subsurface are reflected back and forth between the layers in the subsurface and interfere with each other. Therefore, the data cannot be considered as the sum of data from many separate layers as would be the case for a linear problem. Another problem is the matter of uniqueness. Since the data are measured on the earth's surface at a limited number of positions, there is more than one solution matching the data. We call the problem where we try to find the properties of the earth by probing and measuring it from the outside the inverse problem.

In the 1980s the practise of geophysical data processing took a giant leap forward thanks to the increased computer speed and memory. The current techniques enable us to make three-dimensional images of the subsurface. Every existing processing technique however makes its own approximations and has its own drawbacks. Therefore the search for better and faster techniques is still very relevant. In this search we are not only looking for ways to image the structure of the subsurface but also for methods to recover detailed information on lithology and pore fill of the subsurface.

1.2 Seismic inversion methods

The different existing seismic inversion methods can roughly be divided into three classes: The direct approximate methods, the iterative (nonlinear) methods and the

direct nonlinear methods.

In direct approximate problems the nonlinear inverse problem is reduced to a linear problem by making approximations. Linear problems are mathematically much easier to be solved. The simplest method of linearizing the scattering problem is by using the Born approximation, as described by Morse and Feshbach [24]. Application of the Born approximation requires the reflectivity to be sufficiently weak, such that the transmitted downgoing wavefield is an approximation for the downgoing wavefield in a homogeneous medium. Linearized methods not only assume small variations of the medium parameters but they also neglect multiply reflected waves. Within the class of linearized methods many different solution methods can be distinguished. Some methods construct a direct approximate solution of the linearized equations, such as the method described by Claerbout [8] using the parabolic approximation of the wave equation. Others use schemes based on the wave equation itself. An overview of migration methods such as the Kirchhoff migration is given by Berkhouit [4]. Migration methods aim at producing a depth section without giving information on the material parameters. Migration methods make use of a background model based on a coarse estimation of the subsurface parameters. These migration methods use just the traveltimes (phase) information in the data to locate the reflection interfaces in time or depth sections. Velocity inversion methods also make use of the amplitude information in the data. The methods explained by Cohen and Bleistein in [11] and [12] show how velocity variations can be estimated using linearized techniques, still assuming small velocity variations. A different way of solving linearized problems is by using an iterative algorithm. Tarantola [31] describes a method to estimate the medium parameters iteratively, each step consisting of a Kirchhoff migration and a forward modelling step. This method makes use of a priori model information and then optimizes this model information to a model which is the best in a given, precise, sense.

The second class of inversion methods is the class of iterative nonlinear methods. This type of methods tries to construct a solution of the inverse scattering problem by sequentially updating a model. This model is generally an initial guess and a method is chosen to improve this guess by minimizing the error between model and measured data. Optimization methods tend to require much computation time. Another problem is the danger to end up with a 'local minimum' instead of with the real minimum error. An example to illustrate this problem is given by Cheney [7]: A person trying to minimize his altitude above sea level in a mountain range will have trouble determining whether a bottom of a valley is lower than the other valley bottoms. Many different optimization methods can be applied to inverse scattering problems. Tarantola [32] describes a method based on the least-squares criterion.

Each iterative loop in this inversion method requires the solution of two times as many forward problems as there are source locations. Another example of an inversion method in this class is the Extended Contrast Source Inversion by van den Berg *et al.* [34]. This method is based on the conjugate gradient method and does not require solving the forward problem for each iterative step. Sen and Stoffa [28] describe the class of global optimization methods. These methods do not have a problem with local minima but convergence of these methods to the optimal solution is not guaranteed for most methods. Examples are the Monte Carlo methods, Simulated Annealing and Genetic Algorithms. The advantage of iterative nonlinear methods compared to the linear methods is that strong variations of the medium parameters are handled much better. A disadvantage of these methods is the fact that an a priori model has to be estimated. The choice of this a priori model has influence on the inverted result.

The third class of inversion methods is the class of direct nonlinear methods. This class contains methods that give an explicit expression for the unknown in terms of the data and methods that use explicit algorithms to reconstruct the unknown in a finite number of steps. Most of these methods involve transforming the one-dimensional wave equation into the Schrödinger equation, which obviously cannot be applied directly to multi-dimensional problems. An overview of this class of methods for electromagnetic applications is given by Habashy and Mittra [19]. The most well-known direct nonlinear methods are 'layer-stripping' methods. First, the desired quantities are determined at the earth surface, then the measurements that would have been made if a thin layer below the surface had been absent are mathematically reconstructed. The desired quantities at this new surface are now determined and the method is repeated layer by layer. Examples of layer-stripping methods are described by Yagle and Levy [39] and Koster [21]. The advantage of layer-stripping methods is that they are generally fast and not constrained to small velocity perturbations. Since these methods are completely data driven, measurement errors and noise might result in unstable results. Unlike the optimization methods, layer-stripping does not guarantee that the final reconstructed image will be consistent with the measured data.

1.3 The layer-stripping method in this thesis

The inversion method described in this thesis falls in the class of direct nonlinear methods. The major advantage of this method in comparison with existing layer-stripping methods is the fact that it is applicable to laterally varying media.

Furthermore, we aim to make this method less sensitive to noise and errors in the data. The advantage of this method compared to linearized methods is the fact that multiples are treated correctly and there are no constraints on the velocity model. The advantage of our method compared to optimization methods is that no a priori velocity model has to be included.

Each layer-stripping step in our method consists of two actions: A layer replacement and a contrast determination. The layer replacement is performed by applying the reciprocity theorem. This theorem as described by Fokkema and van den Berg [17] relates two acoustic states to each other. It can be applied to many different acoustic problems such as wavefield decomposition, source deghosting and multiple removal. In our case, one state is the actual state and the other state has the same medium configuration except for the fact that the top layer was removed and replaced by a homogeneous layer with known wavespeed. Using the data measured in the first state we can determine the wavefield in the second state. In the next layer-stripping step this second state will become the new first state and the calculated wavefield will perform as the new 'measured' data. The second action is used to determine the contrast between the top layer and the layer beneath it. In order to determine this contrast we apply an imaging condition which relates the up- and downgoing wavefields just above an interface to the wavefield just below this interface in order to determine the velocity contrast over this interface. The derivation of the imaging condition uses the boundary conditions over an interface and the causality principle. The causality principle is the well-known principle that there will always be a lapse of time for a wave to travel from one position in space to another position. Our research strategy is to first derive the theory for the full three-dimensional case and then start to test the method for its behavior in one dimension. This is then extended to plane wave incidence on horizontally layered media and we invert synthetical data modelled in a two-dimensional laterally varying configuration using common-midpoint techniques. The implementation of the method for the three-dimensional case falls beyond the reach of this research and remains for future research.

As all methods described in the previous section the causality-based imaging method does make some common approximations and assumptions. First, it is assumed that the subsurface wave propagation is adequately described by the acoustic wave equation. By making use of the acoustic approximation we neglect shear wave energy. Second we assume the source wavelet and incident wavefield can be determined. An example of a source wavelet estimation method during removal of surface-related multiples is given by van Borselen [35]. Weglein *et al.* [38] has shown that an estimation of the source wavelet can be made by measuring the vertical derivative of the wavefield together with the wavefield. If we measure however both the pressure

and velocity wavefield we can decompose the pressure wavefield into an upgoing and a downgoing part and determine the wavelet from the downgoing part. Furthermore we focus only on the velocity variations and assume the density to be a constant. Although wave speed and density are related in nature it has been shown that density variations are not the main source of reflected waves [31]. Finally we assume the wave speed in the top layer can be determined. This is not unrealistic, especially not in marine surveys where the top layer is water. These assumptions are made in order to test the method for its ability to determine velocity profiles directly from measured data. The acoustic approximation and the assumption of constant density might be relaxed in further research.

1.4 Time-lapse seismic monitoring

In general, time-lapse measurements can be used to monitor the changes of the (sub-)surface caused by mankind or by environmental circumstances. Over the last decade the use of time-lapse seismic monitoring has advanced rapidly. The main goal of time-lapse seismic surveying is to monitor the changes in a reservoir during oil or gas production. Being able to monitor the fluid flow in a reservoir can significantly improve the recovery of a well. In time-lapse seismic monitoring multiple seismic surveys are acquired and analyzed. The seismic surveys are performed at different moments in time, where the lapse of time between the surveys is on calendar scale and much larger than the recording time. Time-lapse seismic methods are also referred to as 4D seismics where the fourth dimension is time. In reservoir monitoring it is assumed the geology does not change over time, just the reservoir properties do. When changes in fluid saturations or pressures in the reservoir occur, changes in the seismic reflection properties change accordingly. It is common practise in time-lapse seismics to invert the difference section between two seismic measurements. This difference section represents the difference that occurred in the subsurface over time. An overview of the application of time-lapse seismic reservoir monitoring is given by Lumley [23]. In order to obtain valuable 4D data the repeatability of the measurements has to be very high. Also required are very precise inversion methods since the changes in the reservoir are usually small compared to the resolution of the seismics.

The research project leading to this thesis was performed as a part of an inter-faculty research programme focussing on the observation of the earth's surface and subsurface. We aimed to develop an imaging method which is accurate enough to be applied to 4D-problems. Also, the layer-stripping format of our method makes

it possible to focus on the changes in the reservoir only, instead of having to invert entire difference sections.

1.5 Outline of the thesis

The aim of this thesis is to develop a direct inversion method that is applicable to laterally varying media and does not require a priori model information. The first chapters describe the theory behind the method, followed by some implementation results in the last chapters.

Chapter 2 gives the theory of the method in the three-dimensional case. It starts with the general description of some basic terms and principles such as the acoustic wave equations in the time and the space domain and the reciprocity theorem. This is followed by the theory behind the layer replacement method and the derivation of the causality-based imaging condition. We finish this chapter with an overview of the complete layer-stripping procedure.

In Chapter 3 the simplification of the general three-dimensional case to the one-dimensional case is given in steps. First the theory is adjusted for the general two-dimensional case, followed by the case for 2D wave propagation in a horizontally layered medium. From this case the 1D case is derived.

We have chosen to begin with the implementation of the one-dimensional case in order to evaluate the behavior and characteristics of the method, without considering too many influential factors at once. In Chapter 4 we discuss some testing results after implementation of the one-dimensional theory. We discuss how we use the energy of the wavelet to stabilize the method and how the multiples in the data are treated. We discuss how the thickness of the stripped layers influences the result and we give some remarks on the resolution of the layer-stripping method. This is followed by some imaging results for oblique plane-wave incidence. In section 4.2 we compare our method to another layer-stripping method based on the Schur algorithm, known as a fast algorithm applicable to one-dimensional problems.

Chapter 5 deals with the inherent limited bandwidth of the acoustic data. It shows why and how the imaging fails for data without the lowest frequency information. A solution method for this problem is proposed. This solution method uses the envelope or absolute value of the data and does not require background velocity model information. Taking the envelope or absolute value of a wavefield results in a loss of

the sign of the wavefield. We propose a method to deal with this problem, making use of median filters.

Some applications of the layer-stripping method are given in Chapter 6. The application of the layer-stripping method in time-lapse seismics is discussed. We image the velocity change in a reservoir by making use of a difference term based on the one-way reciprocity theorems. This method does not require the wavelets of the two separate measurements to be the same. We finish the chapter with the imaging result for some 2D laterally varying medium examples, using common-midpoint techniques.

The conclusions and some recommendations for further research are given in Chapter 7.

2

Theory

In this chapter the theory behind the layer-stripping method is given for the general 3-dimensional case. We will start by giving the definitions of some basic terms and principles. After that the method for wavefield extrapolation is explained; it is shown how a wavefield below a very thin layer can be determined using Rayleigh's reciprocity theorem, when the wavefield on top of this layer is known. This is followed by the derivation of an imaging condition for the 3-dimensional case. This imaging condition is used to determine the contrast over an interface. The derivation is based on the principle of causality. The wavefield extrapolation method together with the imaging condition are combined to form a layer-stripping method which can determine the acoustic wavespeed in a laterally varying medium layer by layer.

2.1 General description

In the following sections we will use a Cartesian coordinate system with a reference frame built of three mutually perpendicular unit vectors $\mathbf{i}_1, \mathbf{i}_2$ and \mathbf{i}_3 . A location in space is defined by the vector \mathbf{x} , which is specified by its coordinates x_1 , x_2 and x_3 such that

$$\mathbf{x} = x_1 \mathbf{i}_1 + x_2 \mathbf{i}_2 + x_3 \mathbf{i}_3. \quad (2.1)$$

Vectors \mathbf{i}_1 and \mathbf{i}_2 are both horizontally directed. The projection of these vectors will be denoted by \mathbf{x}_T such that $\mathbf{x}_T = x_1 \mathbf{i}_1 + x_2 \mathbf{i}_2$. The vector \mathbf{i}_3 is directed vertically downwards.

Partial differentiation with respect to x_q , where $q = \{1, 2, 3\}$, is denoted by ∂_q , differentiation to time t is denoted by ∂_t .

2.1.1 The summation convention

The summation convention is a shorthand notation to indicate the sum of products of arithmetic arrays. Let a_q and b_q denote one-dimensional arrays with $q = \{1, 2, 3\}$,

then:

$$a_q b_q \quad \text{stands for} \quad \sum_{q=1}^3 a_q b_q. \quad (2.2)$$

To denote the horizontal coordinates only, Greek subscripts are used, for example a_γ is a one-dimensional array with $\gamma = \{1, 2\}$.

2.1.2 Acoustic equations in the space-time domain

Fokkema and van den Berg [17] show how the well-known pair of linear acoustic wave equations can be derived from the equation of motion, a deformation equation and the constitutive relations. These basic acoustic wave equations are given by:

$$\partial_k p(\mathbf{x}, t) + \rho \partial_t v_k(\mathbf{x}, t) = f_k(\mathbf{x}, t), \quad (2.3)$$

$$\partial_k v_k(\mathbf{x}, t) + \kappa \partial_t p(\mathbf{x}, t) = q(\mathbf{x}, t), \quad (2.4)$$

where

$$\begin{aligned} p(\mathbf{x}, t) &= \text{acoustic pressure} & [\text{Pa}], \\ v_k(\mathbf{x}, t) &= \text{particle velocity} & [\text{m/s}], \\ f_k(\mathbf{x}, t) &= \text{volume source density of volume force} & [\text{N/m}^3], \\ q(\mathbf{x}, t) &= \text{volume source density of volume injection rate} & [\text{s}^{-1}], \\ \rho(\mathbf{x}) &= \text{volume density of mass} & [\text{kg/m}^3], \\ \kappa(\mathbf{x}) &= \text{compressibility} & [\text{Pa}^{-1}]. \end{aligned}$$

The compressibility and density are related to the wave speed c as follows:

$$c = (\kappa \rho)^{-\frac{1}{2}}. \quad (2.5)$$

Sources of the volume force type represent the action of acoustic sources of the dipole type, while source of the injection rate type represent the action of acoustic sources of the monopole type.

2.1.3 Acoustic equations in the Laplace domain

By carrying out a Laplace transformation, the time coordinate in the acoustic equations is eliminated, and a set of equations remains in which the transform parameter s occurs. We assume that the sources that generate the acoustic wavefields are

switched on at time instant $t_0 = 0$. In view of causality, we are interested in the behavior of the wavefields in the interval

$$T = (t \in \mathbb{R} | t > 0). \quad (2.6)$$

The one-sided Laplace transform on a signal $u(\mathbf{x}, t)$, defined in $t > 0$ is given by:

$$\hat{u}(\mathbf{x}, s) = \int_{t \in T} \exp(-st) u(\mathbf{x}, t) dt. \quad (2.7)$$

Since the sources under consideration generate wavefields of bounded magnitudes, the right-hand side of Eq. (2.7) converges if the complex Laplace transform parameter s satisfies the constraint $\text{Re}(s) > 0$. When we consider the limiting case $s = j\omega$, in which ω is the angular frequency, the Laplace transform is equivalent to the temporal Fourier transform. The acoustic equations in the Laplace domain have the following form:

$$\partial_k \hat{p}(\mathbf{x}, s) + s\rho \hat{v}_k(\mathbf{x}, s) = \hat{f}_k(\mathbf{x}, s), \quad (2.8)$$

$$\partial_k \hat{v}_k(\mathbf{x}, s) + s\kappa \hat{p}(\mathbf{x}, s) = \hat{q}(\mathbf{x}, s). \quad (2.9)$$

The $t = t_0$ contributions of the Laplace transform are incorporated in the source terms.

In seismic problems, it is common to use the spatial Fourier transformation with respect to x_1 and x_2 , which are the horizontal coordinates. This two-dimensional Fourier transformation is defined as:

$$\begin{aligned} \bar{u}(j s \alpha_1, j s \alpha_2, x_3, s) = & \quad (2.10) \\ & \int_{(x_1, x_2) \in \mathbb{R}^2} \exp(j s \alpha_1 x_1 + j s \alpha_2 x_2) \hat{u}(x_1, x_2, x_3, s) dA, \end{aligned}$$

where $\alpha_T = \{\alpha_1, \alpha_2\}$ is the angular slowness vector and we take $s\alpha_T$ to be real. dA is the elementary surface in \mathbb{R}^2 . The transformation back to the spatial domain is defined as:

$$\begin{aligned} \frac{1}{(2\pi)^2} \int_{(s\alpha_1, s\alpha_2) \in \mathbb{R}^2} & \exp(-j s \alpha_1 x_1 - j s \alpha_2 x_2) \bar{u}(j s \alpha_1, j s \alpha_2, x_3, s) dA \\ & = \hat{u}(x_1, x_2, x_3, s). \end{aligned} \quad (2.11)$$

2.1.4 The reciprocity theorem

In this section we will briefly show the derivation of Rayleigh's reciprocity theorem following Fokkema and van den Berg [17]. The reciprocity theorem relates two non-identical acoustic states in a three-dimensional bounded domain \mathbb{D} to each other. The domain \mathbb{D} is bounded by boundary surface $\partial\mathbb{D}$. The two different states inside the domain will be referred to as state A and state B. Table 2.1 shows how each state is characterized by the acoustic wavefield (\hat{p}, \hat{v}_k) , the constitutive parameters (ρ, κ) , and the source terms (\hat{f}_k, \hat{q}) . The acoustic wave equations in the Laplace domain (see (2.8) and (2.9)) for state A are now:

$$\partial_k \hat{p}^A + s\rho \hat{v}_k^A = \hat{f}_k^A, \quad (2.12)$$

$$\partial_k \hat{v}_k^A + s\kappa \hat{p}^A = \hat{q}^A, \quad (2.13)$$

and for state B:

$$\partial_k \hat{p}^B + s\rho \hat{v}_k^B = \hat{f}_k^B, \quad (2.14)$$

$$\partial_k \hat{v}_k^B + s\kappa \hat{p}^B = \hat{q}^B. \quad (2.15)$$

For simplicity of notation the dependence on (\mathbf{x}, s) is omitted. The interaction between the two states can be described by:

$$\partial_k (\hat{p}_A \hat{v}_k^B - \hat{p}^B \hat{v}_k^A) = \hat{v}_k^B \partial_k \hat{p}_A + \hat{p}_A \partial_k \hat{v}_k^B - \hat{v}_k^A \partial_k \hat{p}_B - \hat{p}_B \partial_k \hat{v}_k^A. \quad (2.16)$$

The interaction quantity (2.16) can be rewritten using the acoustic wave equations (2.12) to (2.15). The result is the local form of Rayleigh's reciprocity theorem:

$$\begin{aligned} \partial_k (\hat{p}^A \hat{v}_k^B - \hat{p}^B \hat{v}_k^A) &= s(\rho^B - \rho^A) \hat{v}_k^A \hat{v}_k^B - s(\kappa^B - \kappa^A) \hat{p}^A \hat{p}^B \\ &\quad + \hat{f}_k^A \hat{v}_k^B + \hat{q}^B \hat{p}^A - \hat{f}_k^B \hat{v}_k^A - \hat{q}^A \hat{p}^B. \end{aligned} \quad (2.17)$$

The global form of Rayleigh's reciprocity theorem can be found by integrating (2.17) over the domain \mathbb{D} and using Gauss' integral theorem in the left-hand side of the equation:

$$\begin{aligned} &\int_{\mathbf{x} \in \partial\mathbb{D}} (\hat{p}^A \hat{v}_k^B - \hat{p}^B \hat{v}_k^A) n_k dA \\ &= \int_{\mathbf{x} \in \mathbb{D}} [s(\rho^B - \rho^A) \hat{v}_k^A \hat{v}_k^B - s(\kappa^B - \kappa^A) \hat{p}^A \hat{p}^B] dV \\ &\quad + \int_{\mathbf{x} \in \mathbb{D}} [\hat{f}_k^A \hat{v}_k^B + \hat{q}^B \hat{p}^A - \hat{f}_k^B \hat{v}_k^A - \hat{q}^A \hat{p}^B] dV, \end{aligned} \quad (2.18)$$

	State A	State B
Field State	$\{\hat{p}^A, \hat{v}_k^A\}(\mathbf{x}, s)$	$\{\hat{p}^B, \hat{v}_k^B\}(\mathbf{x}, s)$
Material State	$\{\rho^A, \kappa^A\}(\mathbf{x})$	$\{\rho^B, \kappa^B\}(\mathbf{x})$
Source State	$\{\hat{q}^A, \hat{f}_k^A\}(\mathbf{x}, s)$	$\{\hat{q}^B, \hat{f}_k^B\}(\mathbf{x}, s)$
Domain \mathbb{D}		

Table 2.1: States in the field reciprocity theorem.

where n_k is the normal vector directed perpendicularly away from the boundary of the domain $\partial\mathbb{D}$. Note that the first and second term at the right-hand side of Eqs. (2.17) and (2.18) vanish when the constitutive parameters are chosen to be the same for state A and state B, meaning $\rho^A = \rho^B$ and $\kappa^A = \kappa^B$.

2.2 Layer replacement

2.2.1 Theory of layer replacement for general 3D case.

In this section we discuss how the wavefield just below a thin layer can be determined when the wavefield on top of this layer is known. The use of the reciprocity theorem is the foundation of the layer replacement method. Figure 2.1 shows the two states to which the reciprocity theorem is applied. These two states will from now on be referred to as state 0 and state 1. In both states we assume an upper ($x_3 < x_3^0$) and a lower half-space ($x_3 \geq x_3^0$). The upper half-space consists of a homogeneous background medium with known constant wave speed c_0 . Source and receiver are positioned in the upper half-space. The lower half-space in both states is divided into thin horizontal layers with thickness Δx_3 . The layers are thin enough to justify the assumption that the wave speed inside a layer does not vary in the vertical direction. The wave speed can however be variable in the lateral direction. The density ρ is assumed to be constant and identical in both half-spaces. State 0 represents the actual state in which the wavefield was measured. State 1 represents an almost

	State 0	State 1
Field State	$\{\hat{p}^0, \hat{v}_k^0\}(\mathbf{x} \mathbf{x}^S)$	$\{\hat{p}^1, \hat{v}_k^1\}(\mathbf{x} \mathbf{x}^R)$
Material State	$\{c_1(\mathbf{x}_T), c_2(\mathbf{x}_T), \dots, c_N(\mathbf{x}_T)\}$	$\{c_0, c_1(\mathbf{x}_T), \dots, c_N(\mathbf{x}_T)\}$
Source State	$\{ \hat{q}^S \delta(\mathbf{x} - \mathbf{x}^S), 0 \}$	$\{ \hat{q}^R \delta(\mathbf{x} - \mathbf{x}^R), 0 \}$
Domain \mathbb{D}		

Table 2.2: States in the field reciprocity theorem.

identical medium configuration except for the top layer which is replaced by a layer with the same properties as the homogeneous background medium. The properties of the acoustic states 0 and 1 are shown in Table 2.2. Since the compressibility κ and the wave speed c are related through $c = (\kappa\rho)^{-\frac{1}{2}}$ and the density ρ is a constant, we can use $c_n(\mathbf{x}_T)$ to describe the material state in the n th layer, where $x_3^{n-1} < x_3 \leq x_3^n$ and n can be any number between 1 and the desired number of stripped layers N . We will take for both states 0 and 1 a point source of volume injection (monopole source). Note the reversed source and receiver positions in state 1 with respect to state 0. Domain \mathbb{D} contains both the upper and the lower half-space. Application of Rayleigh's reciprocity theorem in global form, Eq.(2.18), to the states shown in Figure 2.1 leads to:

$$\begin{aligned}
 & \int_{\mathbf{x} \in \partial\mathbb{D}} (\hat{p}^0(\mathbf{x}|\mathbf{x}^S) \hat{v}_k^1(\mathbf{x}|\mathbf{x}^R) - \hat{p}^1(\mathbf{x}|\mathbf{x}^R) \hat{v}_k^0(\mathbf{x}|\mathbf{x}^S)) n_k dA \\
 &= \int_{\mathbf{x} \in \mathbb{D}} -s(\kappa^1 - \kappa^0) \hat{p}^0(\mathbf{x}|\mathbf{x}^S) \hat{p}^1(\mathbf{x}|\mathbf{x}^R) dV \\
 &+ \int_{\mathbf{x} \in \mathbb{D}} \hat{q}^S \delta(\mathbf{x} - \mathbf{x}^R) \hat{p}^0(\mathbf{x}|\mathbf{x}^S) - \hat{q}^R \delta(\mathbf{x} - \mathbf{x}^S) \hat{p}^1(\mathbf{x}|\mathbf{x}^R) dV. \tag{2.19}
 \end{aligned}$$

The dependency on s is still omitted for simplicity of notation.

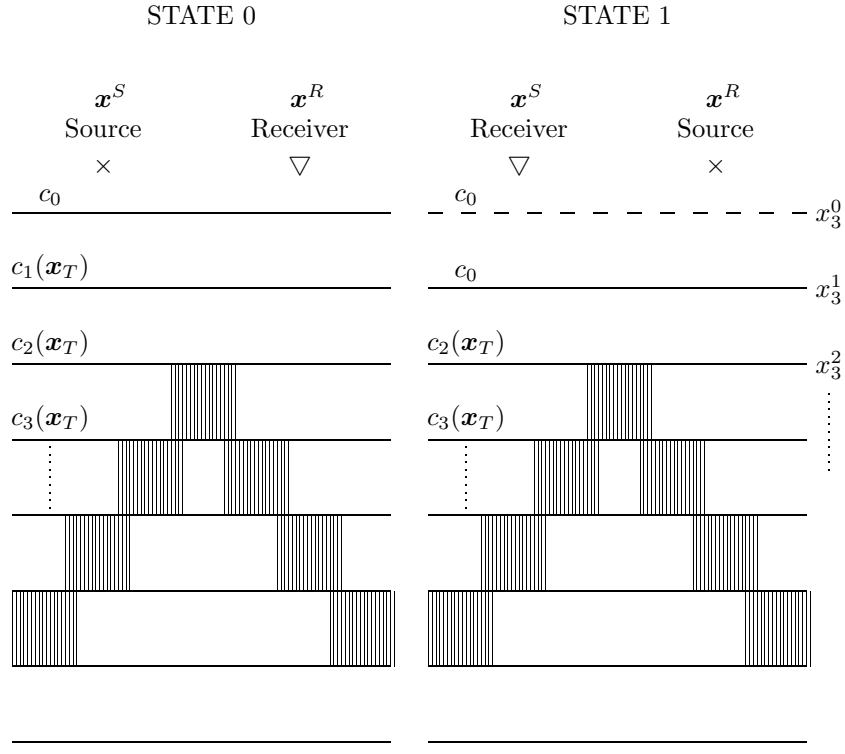


Figure 2.1: Configuration of the two states in Rayleigh's reciprocity theorem for the derivation of layer replacement.

In this notation $\{\hat{p}, \hat{v}_k\}(\mathbf{x}^R | \mathbf{x}^S)$ is the wavefield $\{\hat{p}, \hat{v}_k\}$, which was generated at source position \mathbf{x}^S and measured at receiver position \mathbf{x}^R . If we take domain \mathbb{D} to be a sphere with radius Δ , the left hand side of Eq. (2.19) vanishes in the limit $\Delta \rightarrow \infty$. In that case, the domain \mathbb{D} resembles an unbounded domain. Next, we substitute $\hat{q}^S(s) = \frac{\hat{W}(s)}{\rho s}$ where $\hat{W}(s)$ is the wavelet spectrum, and we define the laterally variable contrast $K(\mathbf{x}_T)$ as:

$$K(\mathbf{x}_T) = \frac{1}{c_0^2} - \frac{1}{c_1^2(\mathbf{x}_T)} = \rho \left(\frac{1}{\rho c_0^2} - \frac{1}{\rho c_1^2(\mathbf{x}_T)} \right) = \rho(\kappa_0 - \kappa_1(\mathbf{x}_T)) = \rho(\kappa^1 - \kappa^0), \quad (2.20)$$

where κ_n denotes the compressibility in *layer n* and κ^n represents the compressibility in *state n*. This results in the following expression:

$$\int_{\mathbf{x} \in \mathbb{D}^0} s^2 K(\mathbf{x}_T) \hat{p}^0(\mathbf{x}|\mathbf{x}^S) \hat{p}^1(\mathbf{x}|\mathbf{x}^R) dV = \hat{W} [\hat{p}^0(\mathbf{x}^R|\mathbf{x}^S) - \hat{p}^1(\mathbf{x}^S|\mathbf{x}^R)]. \quad (2.21)$$

The total wavefield in state 0, \hat{p}^0 , can be decomposed into an incident and a reflected wavefield, $\hat{p}^{0,i}$ and $\hat{p}^{0,r}$ respectively, according to:

$$\hat{p}^0(\mathbf{x}|\mathbf{x}^S) = \hat{p}^{0,i}(\mathbf{x}|\mathbf{x}^S) + \hat{p}^{0,r}(\mathbf{x}|\mathbf{x}^S), \quad x_3 \leq x_3^0. \quad (2.22)$$

The incident field can be expressed as:

$$\hat{p}^{0,i}(\mathbf{x}|\mathbf{x}^S) = \frac{\hat{W} \exp(-\frac{s}{c_0} |\mathbf{x} - \mathbf{x}^S|)}{4\pi |\mathbf{x} - \mathbf{x}^S|}, \quad (2.23)$$

where we made use of Green's function. The Laplace domain representation of the Green's function is given by:

$$\hat{G}(\mathbf{x} - \mathbf{x}', s) = \frac{\exp(-\frac{s}{c_0} |\mathbf{x} - \mathbf{x}'|)}{4\pi |\mathbf{x} - \mathbf{x}'|}. \quad (2.24)$$

Equation (2.24) is the expression for the spherical wave due to a point source in a homogeneous medium. The wavefield in state 1 can be decomposed in an incident and reflected part in a similar way:

$$\hat{p}^1(\mathbf{x}|\mathbf{x}^R) = \hat{p}^{1,i}(\mathbf{x}|\mathbf{x}^R) + \hat{p}^{1,r}(\mathbf{x}|\mathbf{x}^R), \quad x_3 \leq x_3^1. \quad (2.25)$$

Rewriting the reciprocity theorem as applied to state 0 and state 1, (Eq. (2.21)), and making use of Parseval's theorem (see appendix C.1) we find:

$$\begin{aligned} & \frac{1}{(2\pi)^2} \int_{s\alpha_T \in \mathbb{R}^2} dA \int_{x_3^0}^{x_3^1} \bar{p}^1(-js\alpha_T, x_3|\mathbf{x}^R) s^2 \mathcal{K}\{\bar{P}^0\}(js\alpha_T, x_3|\mathbf{x}^S) dx_3 \\ &= \hat{W} [\hat{p}^0(\mathbf{x}^R|\mathbf{x}^S) - \hat{p}^1(\mathbf{x}^S|\mathbf{x}^R)]. \end{aligned} \quad (2.26)$$

A spatial Fourier transformation was performed with respect to the horizontal receiver positions only. These spatial Fourier transformations are defined as:

$$\bar{p}^0(js\alpha_T, x_3|\mathbf{x}^S) = \int_{\mathbf{x}_T \in \mathbb{R}^2} \exp(js\alpha_T \cdot \mathbf{x}_T) \hat{p}^0(\mathbf{x}|\mathbf{x}^S) dA, \quad (2.27)$$

$$\bar{p}^1(-js\alpha_T, x_3|\mathbf{x}^R) = \int_{\mathbf{x}_T \in \mathbb{R}^2} \exp(-js\alpha_T \cdot \mathbf{x}_T) \hat{p}^1(\mathbf{x}|\mathbf{x}^R) dA. \quad (2.28)$$

The operator $\mathcal{K}\{\bar{p}^0\}$ is a compact way of writing the convolution operator in the transformed domain:

$$\begin{aligned} \mathcal{K}\{\bar{p}^0\}(js\alpha_T, x_3 | \mathbf{x}^S) = \\ \frac{1}{(2\pi)^2} \int_{s\alpha'_T \in \mathbb{R}^2} \bar{K}(js\alpha_T - js\alpha'_T) \bar{p}^0(js\alpha'_T, x_3 | \mathbf{x}^S) dA, \end{aligned} \quad (2.29)$$

where

$$\bar{K}(js\alpha_T) = \int_{\mathbf{x}_T \in \mathbb{R}^2} \exp(js\alpha_T \cdot \mathbf{x}_T) K(\mathbf{x}_T) dA. \quad (2.30)$$

Taking a closer look at Eq. (2.26) it is clear that the fields on the right hand side of the equation are not in the same domain as the fields on the left hand side. In order to evaluate this equation the wavefields should all be in the same domain. To accomplish this the following operator is applied:

$$\int_{\mathbf{x}_T^R \in \mathbb{R}^2} \exp(js\alpha_T^R \cdot \mathbf{x}_T^R) \int_{\mathbf{x}_T^S \in \mathbb{R}^2} \exp(-js\alpha_T^S \cdot \mathbf{x}_T^S) \cdots dAdA. \quad (2.31)$$

Application of this operator to the fields on the right-hand side of Eq. (2.26) corresponds to a transformation to the spatial Fourier domain for both source and receiver coordinates. To finally get all fields in the same domain, the forward spatial Fourier transform with respect to the source and receiver positions is performed on the left-hand side of the equation, and we find:

$$\begin{aligned} & \frac{1}{(2\pi)^2} \int_{s\alpha_T \in \mathbb{R}^2} dA \\ & \times \int_{x_3^0}^{x_3^1} \bar{\bar{p}}^1(-js\alpha_T, x_3 | js\alpha_T^R, x_3^R) s^2 \mathcal{K}\{\bar{p}^0\}(js\alpha_T, x_3 | js\alpha_T^S, x_3^S) dx_3 \\ & = \hat{W}[\bar{p}^0(js\alpha_T^R, x_3^R | js\alpha_T^S, x_3^S) - \bar{p}^1(-js\alpha_T^S, x_3^S | js\alpha_T^R, x_3^R)], \end{aligned} \quad (2.32)$$

where the double overbar indicates the double spatial Fourier transformation with respect to both source and receiver coordinates.

The physical reciprocity condition can now be applied. This condition says that for two states with the same medium parameters an interchange of source and receiver position in one state compared to the other means in the spatial Fourier domain an

interchange of the vertical source and receiver position and an opposite sign of the transform variables. The physical reciprocity condition is expressed as follows:

$$\bar{p}^1(-js\alpha_T^S, x_3^S | js\alpha_T^R, x_3^R) = \bar{p}^1(js\alpha_T^R, x_3^R | -js\alpha_T^S, x_3^S), \quad (2.33)$$

When we apply this to Eq. (2.32) we find:

$$\begin{aligned} & \frac{1}{(2\pi)^2} \int_{s\alpha_T \in \mathbb{R}^2} dA \\ & \times \int_{x_3^0}^{x_3^1} \bar{p}^1(js\alpha_T^R, x_3^R | -js\alpha_T, x_3) s^2 \mathcal{K}\{\bar{p}^0\}(js\alpha_T, x_3 | -js\alpha_T^S, x_3^S) dx_3 \\ & = \hat{W}[\bar{p}^0(js\alpha_T^R, x_3^R | -js\alpha_T^S, x_3^S) - \bar{p}^1(js\alpha_T^R, x_3^R | -js\alpha_T^S, x_3^S)]. \end{aligned} \quad (2.34)$$

The incident wavefield in a homogeneous medium in the transformed domain can be written as

$$\bar{p}^i(js\alpha_T, x_3 | -js\alpha_T^S, x_3^S) = (2\pi)^2 \frac{\hat{W}}{2s\Gamma_0^S} \delta(s\alpha_T - s\alpha_T^S) \exp(-s\Gamma_0^S |x_3 - x_3^S|), \quad (2.35)$$

which is the spatial Fourier domain version of Eq. (2.23) with the vertical slowness Γ_0^S :

$$\Gamma_0^S = \left(\frac{1}{c_0^2} + \alpha_T^S \cdot \alpha_T^S \right)^{1/2}, \quad \text{Re}\{\Gamma_0^S\} \geq 0. \quad (2.36)$$

The reflected wavefield in state 0 at depth x_3^R can be expressed in terms of the wavefield at depth x_3^0 by conducting a simple extrapolation step:

$$\begin{aligned} & \bar{p}^{0,r}(js\alpha_T^R, x_3^R | -js\alpha_T^S, x_3^S) = \\ & \exp(-s\Gamma_0^R(x_3^0 - x_3^R)) \bar{p}^{0,r}(js\alpha_T^R, x_3^0 | -js\alpha_T^S, x_3^S), \quad x_3^R \leq x_3^0. \end{aligned} \quad (2.37)$$

with the vertical slowness Γ_0^R :

$$\Gamma_0^R = \left(\frac{1}{c_0^2} + \alpha_T^R \cdot \alpha_T^R \right)^{1/2}, \quad \text{Re}\{\Gamma_0^R\} \geq 0. \quad (2.38)$$

Analogously to Eq. (2.37) the reflected wavefield in state 1 at the receiver position can be written in terms of the reflected wavefield in state one at depth x_3^1 by:

$$\begin{aligned} & \bar{p}^{1,r}(js\alpha_T^R, x_3^R | -js\alpha_T^S, x_3^S) = \\ & \exp(-s\Gamma_0^R(x_3^1 - x_3^R)) \bar{p}^{1,r}(js\alpha_T^R, x_3^1 | -js\alpha_T^S, x_3^S), \quad x_3^R \leq x_3^1. \end{aligned} \quad (2.39)$$

Now we rewrite Eq. (2.34) by decomposing the wavefield in state 1 on the left-hand side into an incident and a reflected part following Eq. (2.25). The wavefields on the right hand side are decomposed in a similar manner leading to:

$$\begin{aligned} & \frac{s^2}{(2\pi)^2} \int_{s\alpha_T \in \mathbb{R}^2} dA \int_{x_3^0}^{x_3^1} [\bar{p}^{1,i}(js\alpha_T^R, x_3^R) - js\alpha_T, x_3) + \\ & \quad \bar{p}^{1,r}(js\alpha_T^R, x_3^R) - js\alpha_T, x_3)] \times \mathcal{K}\{\bar{p}^0\}(js\alpha_T, x_3) - js\alpha_T^S, x_3^S) dx_3 \\ & = \hat{W}[\bar{p}^{0,i}(js\alpha_T^R, x_3^R) - js\alpha_T^S, x_3^S) - \bar{p}^{1,i}(js\alpha_T^R, x_3^R) - js\alpha_T^S, x_3^S) \\ & \quad + \bar{p}^{0,r}(js\alpha_T^R, x_3^R) - js\alpha_T^S, x_3^S) - \bar{p}^{1,r}(js\alpha_T^R, x_3^R) - js\alpha_T^S, x_3^S)]. \end{aligned} \quad (2.40)$$

Now we substitute the expression for the incident wavefield, Eq. (2.35). Note that the incident wavefields on the righthand side will drop out because the incident field in state 1 is equal to the incident field in state 0:

$$\bar{p}^{1,i}(\mathbf{x}^R | \mathbf{x}^S) = \bar{p}^{0,i}(\mathbf{x}^R | \mathbf{x}^S). \quad (2.41)$$

This is the case since source and receiver are both positioned in the same homogeneous background medium ($x_3^{(S,R)} \leq x_3^0$). Next, we extrapolate the receiver position to the first interface, x_3^0 , by applying Eqs. (2.37) and (2.39) and we find:

$$\begin{aligned} & s^2 \hat{W} \int_{x_3^0}^{x_3^1} \frac{\exp(-s\Gamma_0^R(x_3 - x_3^0))}{2s\Gamma_0^R} \mathcal{K}\{\bar{p}^0\}(js\alpha_T^R, x_3) - js\alpha_T^S, x_3^S) dx_3 \\ & + \frac{\exp(-s\Gamma_0^R \Delta x_3)}{(2\pi)^2} \int_{s\alpha_T \in \mathbb{R}^2} \bar{p}^{1,r}(js\alpha_T^R, x_3^1) - js\alpha_T, x_3^S) dA \times \\ & s^2 \int_{x_3^0}^{x_3^1} \exp(s\Gamma_0(x_3 - x_3^S)) \mathcal{K}\{\bar{p}^0\}(js\alpha_T, x_3) - js\alpha_T^S, x_3^S) dx_3 \\ & = \hat{W}[\bar{p}^{0,r}(js\alpha_T^R, x_3^0) - js\alpha_T^S, x_3^S) \\ & \quad - \bar{p}^{1,r}(js\alpha_T^R, x_3^1) - js\alpha_T^S, x_3^S) \exp(-s\Gamma_0^R \Delta x_3)], \end{aligned} \quad (2.42)$$

with

$$\Gamma_0 = \left(\frac{1}{c_0^2} + \alpha_T \cdot \alpha_T \right)^{1/2}, \quad \text{Re}\{\Gamma_0\} \geq 0, \quad (2.43)$$

and $\Delta x_3 = x_3^1 - x_3^0$. We will use this equation to calculate the reflected wavefield in state 1 measured at depth x_3^1 . In order to do this we need to know the total wavefield in state 0 at the same depth. We now perform a similar procedure to Eq. (2.34), by

extrapolating the receiver to one thin layer below the first interface, x_3^1 , this yields:

$$\begin{aligned}
& s^2 \hat{W} \int_{x_3^0}^{x_3^1} \frac{\exp(-s\Gamma_0^R |x_3 - x_3^1|)}{2s\Gamma_0^R} \mathcal{K}\{\bar{p}^0\}(js\alpha_T^R, x_3 | - js\alpha_T^S, x_3^S) dx_3 \\
& + \frac{1}{(2\pi)^2} \int_{s\alpha_T \epsilon \mathbb{R}^2} \bar{p}^{1,r}(js\alpha_T^R, x_3^1 | - js\alpha_T^S, x_3^S) dA \times \\
& s^2 \int_{x_3^0}^{x_3^1} \exp(s\Gamma_0(x_3 - x_3^S)) \mathcal{K}\{\bar{p}^0\}(js\alpha_T, x_3 | - js\alpha_T^S, x_3^S) dx_3 \\
& = \hat{W} [\bar{p}^0(js\alpha_T^R, x_3^1 | - js\alpha_T^S, x_3^S) \\
& - \bar{p}^{1,i}(js\alpha_T^R, x_3^1 | - js\alpha_T^S, x_3^S) - \bar{p}^{1,r}(js\alpha_T^R, x_3^1 | - js\alpha_T^S, x_3^S)]. \tag{2.44}
\end{aligned}$$

In this case the incident fields on the right-hand side of the equation do not cancel, since in state 0 the incident field travels through a layer with wave speed $c_1(\mathbf{x}_T)$, and in state 1 it does not. Multiplying the right- and left-hand side of Eq. (2.42) with $\exp(s\Gamma_0^R \Delta x_3)$ and subtracting the result from Eq. (2.44) we find:

$$\begin{aligned}
& \bar{p}^0(js\alpha_T^R, x_3^1 | - js\alpha_T^S, x_3^S) = \bar{p}^{0,r}(js\alpha_T^R, x_3^0 | - js\alpha_T^S, x_3^S) \exp(s\Gamma_0^R \Delta x_3) \\
& + \bar{p}^{0,i}(js\alpha_T^R, x_3^0 | - js\alpha_T^S, x_3^S) \exp(-s\Gamma_0^R \Delta x_3) \\
& + s^2 \int_{x_3^0}^{x_3^1} \frac{\sinh(s\Gamma_0^R(x_3 - x_3^1))}{s\Gamma_0^R} \mathcal{K}\{\bar{p}^0\}(js\alpha_T^R, x_3 | - js\alpha_T^S, x_3^S) dx_3, \tag{2.45}
\end{aligned}$$

where

$$\sinh(x) = \frac{\exp(x) - \exp(-x)}{2}. \tag{2.46}$$

We call Eqs. (2.42) and (2.45) the two basic equations, where Eq. (2.45) is the consistency equation, which is used to determine the total wavefield in state 0 recorded at position x_3^1 . Once this wavefield is known, Eq. (2.42) is used to determine the reflected field in state 1 at depth x_3^1 . After the top layer has been replaced by a layer with the homogeneous background medium properties, the source can be moved downwards over Δx_3 and state 1 becomes the actual state (state 0) for the next layer-stripping step. In both basic equations, Eqs. (2.42) and (2.45), the velocity $c(\mathbf{x}_T)$ in the top layer has to be known. In order to determine this velocity we use an imaging condition based on the causality principle. The derivation of this imaging condition is shown in the next section.

2.3 A causality-based imaging condition

2.3.1 Derivation of imaging condition for laterally varying 3D media.

In this section we derive an imaging condition which relates the up- and downgoing waves just above an interface to the velocity contrast over this interface. The term imaging condition is a term known from migration, where in the imaging condition the $t = 0$ -value is used to determine the reflectivity. This principle was first introduced by Claerbout [8]. Our imaging condition resembles the imaging condition in migration in the sense that we also use the $t = 0$ -value of the wavefields. A difference is however the fact that we use the imaging condition to directly determine the medium parameter wavespeed as opposed to determining the reflectivity.

We consider a medium consisting of two half-spaces, a homogeneous upper half-space and a heterogeneous lower half-space. The lower half-space is heterogeneous in the horizontal direction but not in the vertical direction. The medium configuration is shown in Figure 2.2.

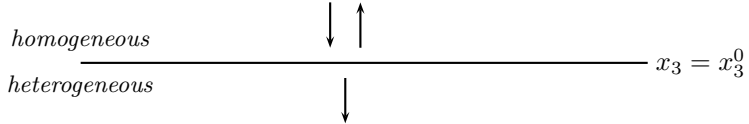


Figure 2.2: Medium configuration for derivation of imaging condition.

When a wave travels downwards the two boundary conditions across the interface between the two half-spaces are:

$$\lim_{\epsilon \downarrow 0} \partial_3 \bar{p} \Big|_{x_3^0 - \epsilon} = \lim_{\epsilon \downarrow 0} \partial_3 \bar{p} \Big|_{x_3^0 + \epsilon}, \quad (2.47)$$

$$\lim_{\epsilon \downarrow 0} \bar{p} \Big|_{x_3^0 - \epsilon} = \lim_{\epsilon \downarrow 0} \bar{p} \Big|_{x_3^0 + \epsilon}, \quad (2.48)$$

where the wavefields are written in the single spatial Fourier domain and \bar{p} is short-hand for $\bar{p}(js\alpha_T, x_3 | \mathbf{x}^S)$. The first boundary condition states that the component of the particle velocity normal to the interface is continuous across this interface. We will write this boundary condition in a short hand notation:

$$\partial_3^{\uparrow} \bar{p} \Big|_{x_3^0} = \partial_3^{\downarrow} \bar{p} \Big|_{x_3^0}, \quad (2.49)$$

where the term $\partial_3^\uparrow \bar{p}|_{x_3^0}$ denotes the vertical derivative of the pressure wavefield very close to the interface when approaching the interface from the side of the upper half-space (from small x_3 to large x_3). A solution for the partial derivative in the x_3 direction approaching the interface from above is known:

$$\partial_3^\uparrow \bar{p}|_{x_3^0} = s\Gamma_0^R(\bar{p}^r - \bar{p}^i), \quad (2.50)$$

where $\bar{p} = \bar{p}^i + \bar{p}^r$. This solution accounts for the opposite direction of propagation of the upgoing wavefield \bar{p}^r and the downgoing wavefield \bar{p}^i by the minus sign. From the Helmholtz equation it follows that the second derivative in the vertical direction over the pressure wavefield shows a jump across the interface which is proportional to the velocity contrast over this interface. The Helmholtz equation for constant density is defined as:

$$\partial_3^2 \hat{p} = \left(\frac{s^2}{c^2} - \partial_\gamma \partial_\gamma\right) \hat{p}. \quad (2.51)$$

From this it follows directly that:

$$\{(\partial_3^\uparrow)^2 - (\partial_3^\downarrow)^2\} \hat{p} = \left(\frac{s^2}{c_0^2} - \frac{s^2}{c_1^2(\mathbf{x}_T)}\right) \hat{p} = s^2 K \hat{p}. \quad (2.52)$$

In the spatial Fourier domain this corresponds to:

$$\{(\partial_3^\uparrow)^2 - (\partial_3^\downarrow)^2\} \bar{p} = s^2 \mathcal{K} \bar{p}. \quad (2.53)$$

The same follows from the Taylor expansions shown in appendix B, (see Eq. (B.17)). Note that \mathcal{K} is a convolutional operator similar to the one in Eq (2.29). Eq (2.53) can be rewritten as:

$$(\partial_3^\downarrow)^2 \bar{p} = (\partial_3^\uparrow)^2 \bar{p} - s^2 \mathcal{K} \bar{p}, \quad (2.54)$$

The second derivative of the wavefield in a homogeneous medium is known, so we can write for the upper half-space:

$$(\partial_3^\uparrow)^2 \bar{p} = s^2 (\Gamma_0^R)^2 \bar{p}. \quad (2.55)$$

Substituting this in Eq. (2.54) we find for the lower half-space:

$$(\partial_3^\downarrow)^2 \bar{p} = s^2 ((\Gamma_0^R)^2 - \mathcal{K}) \bar{p}. \quad (2.56)$$

When there are only downgoing waves below the interface we can write:

$$(\partial_3^\downarrow)^2 \bar{p} = -s \sqrt{(\Gamma_0^R)^2 - \mathcal{K}} \bar{p} \quad (2.57)$$

Note that the term $\sqrt{(\Gamma_0^R)^2 - \mathcal{K}}$ is a pseudo-differential operator. Substituting this term in Eq. (2.49) together with Eq. (2.50) yields:

$$\Gamma_0^R(\bar{p}^r - \bar{p}^i) = -\sqrt{(\Gamma_0^R)^2 - \mathcal{K}} \bar{p}. \quad (2.58)$$

Now write, multiplying $\bar{p} = \bar{p}^i + \bar{p}^r$ by Γ_0^R :

$$\Gamma_0^R \bar{p}^r + \Gamma_0^R \bar{p}^i = \Gamma_0^R \bar{p}, \quad (2.59)$$

and add these equations:

$$2\Gamma_0^R \bar{p}^r = (-\sqrt{(\Gamma_0^R)^2 - \mathcal{K}} + \Gamma_0^R) \bar{p}. \quad (2.60)$$

Subtracting the same two equations results in:

$$2\Gamma_0^R \bar{p}^i = (\sqrt{(\Gamma_0^R)^2 - \mathcal{K}} + \Gamma_0^R) \bar{p}. \quad (2.61)$$

In the next step we will make use of the inner product which is defined as:

$$\langle \bar{f}, \bar{g} \rangle = \frac{1}{2\pi} \int_{-\infty}^{\infty} \bar{f}(\alpha) \bar{g}(-\alpha) d\alpha. \quad (2.62)$$

For the inner product between the terms for the up- and downgoing wavefield we can write:

$$\begin{aligned} \langle 2\Gamma_0^R \bar{p}^r, 2\Gamma_0^R \bar{p}^i \rangle = & \\ & [\langle \Gamma_0^R \bar{p}, \Gamma_0^R \bar{p} \rangle + \langle \Gamma_0^R \bar{p}, \sqrt{(\Gamma_0^R)^2 - \mathcal{K}} \bar{p} \rangle - \langle \sqrt{(\Gamma_0^R)^2 - \mathcal{K}} \bar{p}, \Gamma_0^R \bar{p} \rangle \\ & - \langle \sqrt{(\Gamma_0^R)^2 - \mathcal{K}} \bar{p}, \sqrt{(\Gamma_0^R)^2 - \mathcal{K}} \bar{p} \rangle]. \end{aligned} \quad (2.63)$$

We will now make use of the fact that the pseudo-differential operator is symmetric, as shown in appendix A. Note that the operator is only proven to be symmetric when we meet the condition $s = j\omega$. The two middle terms on the right hand side drop out and we can write for the remaining two terms:

$$\begin{aligned} [\langle \Gamma_0^R \bar{p}, \Gamma_0^R \bar{p} \rangle] - \langle \sqrt{(\Gamma_0^R)^2 - \mathcal{K}} \bar{p}, \sqrt{(\Gamma_0^R)^2 - \mathcal{K}} \bar{p} \rangle = & \\ [\langle \bar{p}, (\Gamma_0^R)^2 \bar{p} \rangle - \langle \bar{p}, ((\Gamma_0^R)^2 - \mathcal{K}) \bar{p} \rangle] = \langle \bar{p}, \mathcal{K} \bar{p} \rangle. \end{aligned} \quad (2.64)$$

We have now found the following result:

$$4\langle \Gamma_0^R \bar{p}^r, \Gamma_0^R \bar{p}^i \rangle = \langle \bar{p}, \mathcal{K} \bar{p} \rangle. \quad (2.65)$$

Note that this equation is only valid when there is no upgoing wavefield below the interface, only a downgoing wavefield. If this is not the case, Eq. (2.57) does not hold. When the lower half-space is heterogeneous in the vertical direction as well as in horizontal direction, as is would be in a realistic earth model, there will be an upgoing wavefield below the interface. We now use the causality principle: since it

will always take a lapse of time for a wave to travel from one position in space to another position in space, there will always be a time interval where the upgoing waves in the lower half-space have not reached the area just below the interface yet. During this short time interval there are only downgoing waves just below the interface and the imaging condition is valid. In order to meet this condition we define our imaging condition to be valid for time $t = 0$ only. This leaves us the desired imaging condition:

$$\mathcal{F}_t^{-1} [4\langle \Gamma_0^R \bar{p}^r, \Gamma_0^R \bar{p}^i \rangle] = \mathcal{F}_t^{-1} [\langle \bar{p}, \mathcal{K} \bar{p} \rangle], \quad t = 0, \quad (2.66)$$

where \mathcal{F}_t^{-1} stands for the inverse temporal Fourier transform, where we use $s = j\omega$. The imaging condition shows that the contrast over an interface can be determined once the up- and downgoing parts of the pressure wavefield are known.

2.3.2 The layer-stripping procedure

The layer-stripping procedure combines the wavefield extrapolation method explained in section 2.2.1 and the causality-based imaging condition as explained in section 2.3.1. When both pressure and velocity wavefields are measured, the pressure wavefield can be decomposed in an upgoing and a downgoing part. This is shown by Fokkema and van den Berg in [17]. The wavefields are measured above a medium which is divided in thin horizontal layers. These layers are virtual, meaning that they do not necessarily coincide with the actual interfaces in the subsurface. Using the decomposed pressure wavefield the contrast over the first virtual horizontal interface can be defined by applying the imaging condition (2.66):

$$\mathcal{F}^{-1} [4\langle \Gamma_0^R \bar{p}^r, \Gamma_0^R \bar{p}^i \rangle] = \mathcal{F}^{-1} [\langle \bar{p}, \mathcal{K} \bar{p} \rangle], \quad t = 0, \quad (2.67)$$

where

$$\begin{aligned} \mathcal{K}\{\bar{p}\}(js\alpha_T, x_3 | \mathbf{x}^S) &= \\ \frac{1}{(2\pi)^2} \int_{s\alpha'_T \in \mathbb{R}^2} \bar{K}(js\alpha_T - js\alpha'_T) \bar{p}(js\alpha'_T, x_3 | \mathbf{x}^S) dA, \end{aligned} \quad (2.68)$$

$$\bar{K}(js\alpha_T) = \int_{\mathbf{x}_T \in \mathbb{R}^2} \exp(j s \alpha_T \cdot \mathbf{x}_T) K(\mathbf{x}_T) dA. \quad (2.69)$$

and

$$K(\mathbf{x}_T) = \frac{1}{c_0^2} - \frac{1}{c_1^2(\mathbf{x}_T)}. \quad (2.70)$$

The imaging condition is solved by determining the inner product of the wavefields per frequency in the frequency domain, performing an inverse Laplace transform on the inner products, and solving for K in the time domain. The horizontal layers are defined to be thin enough to justify the assumption that they are homogeneous in the vertical direction (but not necessarily in the lateral direction). Once the contrast over the first interface is known and therefore also the propagation velocity in the top layer, we can determine the wavefield just below this layer using the first basic equation (2.45):

$$\begin{aligned} \bar{\bar{p}}^0(j s \alpha_T^R, x_3^1 | -j s \alpha_T^S, x_3^S) &= \bar{\bar{p}}^{0,r}(j s \alpha_T^R, x_3^0 | -j s \alpha_T^S, x_3^S) \exp(s \Gamma_0^R \Delta x_3) \\ &+ \bar{\bar{p}}^{0,i}(j s \alpha_T^R, x_3^0 | -j s \alpha_T^S, x_3^S) \exp(-s \Gamma_0^R \Delta x_3) \\ &+ s^2 \int_{x_3^0}^{x_3^1} \frac{\sinh(s \Gamma_0^R(x_3 - x_3^1))}{s \Gamma_0^R} \mathcal{K}\{\bar{\bar{p}}^0\}(j s \alpha_T^R, x_3 | -j s \alpha_T^S, x_3^S) dx_3. \end{aligned} \quad (2.71)$$

Note that it is not necessary to write the wavefields in the imaging condition in the double spatial Fourier domain. The imaging can be derived by considering only one Fourier transform, in particular with respect to the receiver coordinate, while for performing the layer replacement the information from all source and receiver locations is required. The integral over x_3 in Eq 2.72 is solved using the trapezoidal rule. This wavefield is then used in the determination of wavefield $\bar{\bar{p}}^{1,r}(j s \alpha_T^R, x_3^1 | -j s \alpha_T^S, x_3^S)$. This is the upgoing pressure wavefield measured at depth x_3^1 when the top layer is replaced by a layer with the same properties as the homogeneous background medium (state 1 in Rayleigh's reciprocity theorem). This wavefield after 'stripping' the top layer is calculated using the second basic equation, Eq. (2.42):

$$\begin{aligned} &s^2 \hat{W} \int_{x_3^0}^{x_3^1} \frac{\exp(-s \Gamma_0^R(x_3 - x_3^0))}{2s \Gamma_0^R} \mathcal{K}\{\bar{\bar{p}}^0\}(j s \alpha_T^R, x_3 | -j s \alpha_T^S, x_3^S) dx_3 \\ &+ \frac{\exp(-s \Gamma_0^R \Delta x_3)}{(2\pi)^2} \int_{s \alpha_T \in \mathbb{R}^2} \bar{\bar{p}}^{1,r}(j s \alpha_T^R, x_3^1 | -j s \alpha_T^S, x_3^S) dA \times \\ &s^2 \int_{x_3^0}^{x_3^1} \exp(s \Gamma_0(x_3 - x_3^S)) \mathcal{K}\{\bar{\bar{p}}^0\}(j s \alpha_T, x_3 | -j s \alpha_T^S, x_3^S) dx_3 \\ &= \hat{W}[\bar{\bar{p}}^{0,r}(j s \alpha_T^R, x_3^0 | -j s \alpha_T^S, x_3^S) \\ &\quad - \bar{\bar{p}}^{1,r}(j s \alpha_T^R, x_3^1 | -j s \alpha_T^S, x_3^S) \exp(-s \Gamma_0^R \Delta x_3)], \end{aligned} \quad (2.72)$$

After discretization in the frequency and wavenumber domain we can write this integral equation as a matrix equation of the following form:

$$\bar{\bar{\mathbf{P}}}^{1,r}(\bar{\bar{\mathbf{I}}} + \bar{\bar{\mathbf{K}}}) = \bar{\bar{\mathbf{T}}}^{data}, \quad (2.73)$$

where $\bar{\bar{\mathbf{P}}}^{1,r}$ is the matrix to be solved, $\bar{\bar{\mathbf{T}}}^{data}$ is a term containing known wavefields, $\bar{\bar{\mathbf{I}}}$ is the unit matrix and $\bar{\bar{\mathbf{K}}}$ is the discretized kernel. In order to solve this matrix equation, the sampling rate in the source and receiver direction must be equal and the equation has to be solved for each frequency. The matrix equations can be solved using a standard matrix inversion method. A solution method for the integral equations using Taylor series and Neumann iterations is given in appendix B. Once the wavefield $\bar{\bar{p}}^{1,r}(js\alpha_T^R, x_3^1 | -js\alpha_T, x_3^S)$ is known, the entire procedure can be repeated. The imaging condition is used to determine the contrast over the next (virtual) interface and the wavefield as determined in the second basic equation (Eq. (2.73)) becomes the wavefield in the new state 0, see Figure 2.1. The entire procedure can be repeated until the desired depth is reached and a velocity profile of the lower half-space is determined. The procedure is referred to as a 'layer-stripping'-procedure since the medium is evaluated layer by layer and once the information concerning one layer is used, this layer is replaced and not considered anymore in the further evaluation of the medium. An overview of the total procedure is shown in Figure 2.3. Note that before the layer-stripping can be applied the data has to be preprocessed such that a configuration with a homogeneous upper half-space and a heterogeneous lower half-space is simulated. This means for example that surface-related multiples in the marine case should be removed.

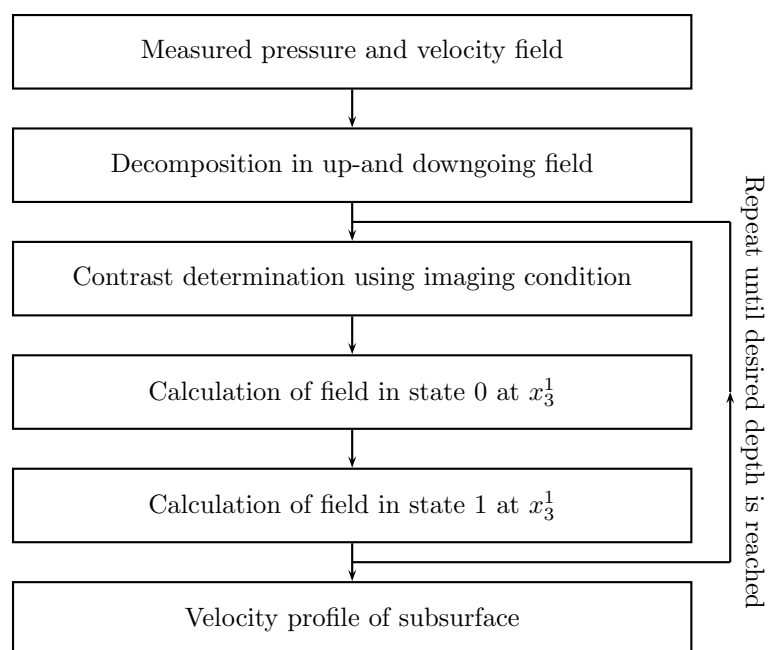


Figure 2.3: Flow diagram of layer-stripping algorithm.

3

The one-dimensional case

The theory for the laterally varying, three-dimensional case has been fully derived in Chapter 2. Solving the basic equations, Eqs. (2.42) and (2.45) and the imaging condition, Eq. (2.66), in this case involves solving pseudo-differential equations and large matrix manipulations. In order to analyze the theory, we start with the computationally much more simple one-dimensional case, where both medium and wavefield are one-dimensional. First we simplify the theory derived in Chapter 2 to the case where both medium and wavefield are two-dimensional, the two-dimensional case. Then we simplify this to the horizontally layered case, where the wavefield is two-dimensional and the medium is one-dimensional, and finally to the one-dimensional case. We also show the derivation of the imaging condition for the one dimensional case.

3.1 Theory for the two-dimensional case.

In the two-dimensional case we consider a two-dimensional wavefield generated by a monopole line source along the x_2 direction. The medium does not vary in the x_2 direction. To find the expression for a monopole line source, the expression for a monopole point source is integrated with respect to x_2 . The wavefield in the Laplace domain, generated by a monopole point source at point \mathbf{x}_S in a homogeneous medium is written as:

$$\hat{p}^i(\mathbf{x}, s) = \hat{W}(s) \hat{G}(\mathbf{x} - \mathbf{x}^S, s), \quad (3.1)$$

where $\hat{G}(\mathbf{x}, s)$ is the Green's function (Eq. (2.24)). For a monopole line source we write:

$$\hat{p}^i(x_1, x_3, s) = \hat{W}(s) \int_{x_2 \in \mathbb{R}} \hat{G}(x_1 - x_1^S, x_2, x_3 - x_3^S, s) dx_2. \quad (3.2)$$

It follows:

$$\hat{p}^i(x_1, x_3, s) = \hat{W}(s) \hat{G}^{(2)}(x_1 - x_1^S, x_3 - x_3^S, s), \quad (3.3)$$

where $\hat{G}^{(2)}$ is the two-dimensional Green's function, which can be expressed as:

$$\hat{G}^{(2)}(x_1, x_3, s) = \frac{1}{2\pi} \int_{s\alpha_1 \in \mathbb{R}} \frac{\exp(j s(\alpha_1 x_1 - s\Gamma_0 |x_3|)}{2s\Gamma_0} d(s\alpha_1), \quad (3.4)$$

where the vertical slowness Γ_0 is:

$$\Gamma_0 = \left(\frac{1}{c_0^2} + \alpha_1^2 \right)^{1/2}, \quad \text{Re}\{\Gamma\} \geq 0. \quad (3.5)$$

The incident wavefield in the spatial Fourier domain for the two-dimensional case in a homogeneous medium can now be written as:

$$\bar{p}^i(j s \alpha_1^R, x_3^R | - j s \alpha_1^S, x_3^S) = (2\pi) \frac{\hat{W}}{2s\Gamma_0^S} \delta(s\alpha_1^R - s\alpha_1^S) \exp(-s\Gamma_0^S |x_3^R - x_3^S|). \quad (3.6)$$

Consider the first of our basic equations, Eq. (2.42) before substitution of the expression for the incident field:

$$\begin{aligned} & \frac{1}{(2\pi)^2} s^2 \int_{x_3^0}^{x_3^1} \int_{s\alpha_T \in \mathbb{R}^2} \bar{p}^{1,i}(j s \alpha_T^R, x_3^R | - j s \alpha_T^S, x_3^S) \\ & \times \mathcal{K}\{\bar{p}^0\}(j s \alpha_T^R, x_3^R | - j s \alpha_T^S, x_3^S) dA dx_3 \\ & + \frac{\exp(-s\Gamma_0^R \Delta x_3)}{(2\pi)^2} \int_{s\alpha_T \in \mathbb{R}^2} \bar{p}^{1,r}(j s \alpha_T^R, x_3^1 | - j s \alpha_T^S, x_3^S) dA \times \\ & s^2 \int_{x_3^0}^{x_3^1} \exp(s\Gamma_0(x_3 - x_3^S)) \mathcal{K}\{\bar{p}^0\}(j s \alpha_T^R, x_3^R | - j s \alpha_T^S, x_3^S) dx_3 \\ & = \hat{W}[\bar{p}^{0,r}(j s \alpha_T^R, x_3^0 | - j s \alpha_T^S, x_3^S) \\ & - \bar{p}^{1,r}(j s \alpha_T^R, x_3^1 | - j s \alpha_T^S, x_3^S) \exp(-s\Gamma_0^R \Delta x_3)] \end{aligned} \quad (3.7)$$

Since there is no variation in the x_2 direction we can write:

$$\bar{K}(j s \alpha_T) = (2\pi) \delta(j s \alpha_2) \bar{K}(j s \alpha_1). \quad (3.8)$$

Substituting this in the expression for the convolutional operator , Eq (2.68), we find:

$$\begin{aligned} & \mathcal{K}\{\bar{p}^0\}(j s \alpha_1, x_3^R | - j s \alpha_1, x_3^S) = \\ & \frac{1}{(2\pi)} \int_{s\alpha'_1 \in \mathbb{R}} \bar{K}(j s \alpha_1 - j s \alpha'_1) \bar{p}^0(j s \alpha'_1, x_3^R | - j s \alpha_1, x_3^S) d(s\alpha'_1). \end{aligned} \quad (3.9)$$

Further, when the fields are independent of x_2 we can write:

$$\bar{p}(js\alpha_T, x_3) = (2\pi)\delta(js\alpha_2)\bar{p}(js\alpha_1, x_3). \quad (3.10)$$

Substituting Eq. (3.10) in the first basic equation, Eq. (3.7), the integrals over $s\alpha_T$ on the left hand side of the equation will reduce to integrals over $s\alpha_1$ as a result of the delta function in Eq. (3.10). Now substitute Eq. (3.6) for the incident field and the integral in the first term will cancel entirely as a result of the delta term in this expression. The delta terms that are still left in the equation cancel on both sides of the equality-sign. We have now arrived at the 2D-expression of the first basic equation:

$$\begin{aligned} s^2 \hat{W} \int_{x_3^0}^{x_3^1} \frac{\exp(-s\Gamma_0^R(x_3 - x_3^0))}{2s\Gamma_0^R} \mathcal{K}\{\bar{p}^0\}(js\alpha_1^R, x_3| - js\alpha_1^S, x_3^S) dx_3 \\ + \frac{1}{2\pi} \exp(-s\Gamma_0^R \Delta x_3) \int_{s\alpha_1 \in \mathbb{R}} \bar{p}^{1,r}(js\alpha_1^R, x_3^1| - js\alpha_1^S, x_3^S) d(s\alpha_1) \\ \times s^2 \int_{x_3^0}^{x_3^1} \exp(s\Gamma_0(x_3 - x_3^S)) \mathcal{K}\{\bar{p}^0\}(js\alpha_1, x_3| - js\alpha_1^S, x_3^S) dx_3 \\ = \hat{W} [\bar{p}^{0,r}(js\alpha_1^R, x_3^0| - js\alpha_1^S, x_3^S) \\ - \bar{p}^{1,r}(js\alpha_1^R, x_3^1| - js\alpha_1^S, x_3^S) \exp(-s\Gamma_0^R \Delta x_3)], \end{aligned} \quad (3.11)$$

Substituting Eq. (3.10) in Eq. (2.45), we find the 2D version of the consistence equation, the second basic equation:

$$\begin{aligned} \bar{p}^0(js\alpha_1^R, x_3^1| - js\alpha_1^S, x_3^S) = \\ \bar{p}^{0,r}(js\alpha_1^R, x_3^0| - js\alpha_1^S, x_3^S) \exp(s\Gamma_0^R \Delta x_3) \\ + \bar{p}^{0,i}(js\alpha_1^R, x_3^0| - js\alpha_1^S, x_3^S) \exp(-s\Gamma_0^R \Delta x_3) \\ + s^2 \int_{x_3^0}^{x_3^1} \frac{\sinh(s\Gamma_0^R(x_3 - x_3^1))}{s\Gamma_0^R} \mathcal{K}\{\bar{p}^0\}(js\alpha_1^R, x_3| - js\alpha_1^S, x_3^S) dx_3. \end{aligned} \quad (3.12)$$

3.1.1 A horizontally layered medium.

In case of a horizontally layered medium the operator $\mathcal{K}\{\bar{p}\}$ is no longer a convolutional operator but a simple multiplication of the field by scalar K . Since in this

case the contrast does not vary in the x_1 -direction we can write:

$$\bar{K}(js\alpha_1 - js\alpha'_1, x_3) = (2\pi)\delta(js\alpha_1 - js\alpha'_1)K(x_3). \quad (3.13)$$

Substituting this in Eq. (3.10) it is clear the integral vanishes as a result of the delta function and a simple multiplication is left. The contrast is now defined as:

$$K = \frac{1}{\rho c_0^2} - \frac{1}{\rho c_1^2}. \quad (3.14)$$

In case of such a so-called 1-D configuration, the data are shift invariant with respect to the horizontal source coordinate, x_1^S , and depend only on the lateral distance $(x_1^R - x_1^S)$ between source and receiver position. Consequently we can write:

$$\hat{p}(x_1^R, x_3^R | x_1^S, x_3^S) = \hat{p}(x_1^R - x_1^S, x_3^R | 0, x_3^S). \quad (3.15)$$

Now apply the forward Fourier transformation with respect to both source and receiver position:

$$\bar{p}(js\alpha_1^R, x_3^R | js\alpha_1^S, x_3^S) = (2\pi)\delta(s\alpha_1^R - s\alpha_1^S)\bar{p}(js\alpha_1^R, x_3^R | 0, x_3^S). \quad (3.16)$$

Applying this to the 2D-version of our first basic equation, Eq. (3.11), we find:

$$\begin{aligned} & s^2 K \hat{W} \int_{x_3^0}^{x_3^1} \frac{\exp(-s\Gamma_0^R(x_3 - x_3^0))}{2s\Gamma_0^R} \bar{p}^0(js\alpha_1^R, x_3 | x_3^S) dx_3 \\ & + \exp(-s\Gamma_0^R \Delta x_3) \bar{p}^{1,r}(js\alpha_1^R, x_3^1 | x_3^S) \times \\ & s^2 K \int_{x_3^0}^{x_3^1} \exp(s\Gamma_0(x_3 - x_3^S)) \bar{p}^0(js\alpha_1^R, x_3 | x_3^S) dx_3 \\ & = \hat{W} [\bar{p}^{0,r}(js\alpha_1^R, x_3^0 | x_3^S) - \bar{p}^{1,r}(js\alpha_1^R, x_3^1 | x_3^S) \exp(-s\Gamma_0^R \Delta x_3)]. \end{aligned} \quad (3.17)$$

The integral over $s\alpha_1$ has dropped out as a result of the delta function and the term (2π) has been cancelled with the same term in front of the integral. The term $(2\pi)\delta(s\alpha_1^R + s\alpha_1^S)$ showed up on both the right- and left-hand side of the equation, so this term was cancelled as well. Also note that the term $s^2 K$ can be written in front of the integral since it is an integration over the small area x_3^0 to x_3^1 only, in which area the contrast is a constant now. For convenience of notation we have written: $\bar{p}(js\alpha_1^R, x_3^R | 0, x_3^S) = \bar{p}(js\alpha_1^R, x_3^R | x_3^S)$.

Application of Eq. (3.16) to Eq. (3.12) leads to a similar cancellation of the $(2\pi)\delta(s\alpha_1^R + s\alpha_1^S)$ term. We find:

$$\begin{aligned} \bar{p}^0(j s \alpha_1^R, x_3^1 | x_3^S) &= \\ \bar{p}^{0,r}(j s \alpha_1^R, x_3^0 | x_3^S) \exp(s \Gamma_0^R \Delta x_3) + \bar{p}^{0,i}(j s \alpha_1^R, x_3^0 | x_3^S) \exp(-s \Gamma_0^R \Delta x_3) \\ + s^2 K \int_{x_3^0}^{x_3^1} \frac{\sinh(s \Gamma_0^R (x_3 - x_3^1))}{s \Gamma_0^R} \bar{p}^0(j s \alpha_1^R, x_3 | x_3^S) dx_3. \end{aligned} \quad (3.18)$$

3.2 Theory for the one-dimensional case.

The last step is the simplification to a one-dimensional wavefield as well as a one-dimensional medium. In this case $\alpha = 0$. As a result the expression for Γ_0 (see Eq.(3.5)) reduces to $\Gamma_0 = \frac{1}{c_0}$. The two basic equations now become:

$$\begin{aligned} s^2 K \hat{W} \int_{x_3^0}^{x_3^1} \frac{c_0}{2s} \exp\left(-\frac{s}{c_0}(x_3 - x_3^0)\right) \hat{p}^0(x_3 | x_3^S) dx_3 + \\ \exp\left(-\frac{s}{c_0} \Delta x_3\right) \hat{p}^{1,r}(x_3^1 | x_3^S) s^2 K \int_{x_3^0}^{x_3^1} \exp\left(\frac{s}{c_0}(x_3 - x_3^S)\right) \hat{p}^0(x_3 | x_3^S) dx_3 \\ = \hat{W}[\hat{p}^{0,r}(x_3^0 | x_3^S) - \hat{p}^{1,r}(x_3^1 | x_3^S) \exp(-\frac{s}{c_0} \Delta x_3)], \end{aligned} \quad (3.19)$$

and:

$$\begin{aligned} \hat{p}^0(x_3^1 | x_3^S) &= \hat{p}^{0,r}(x_3^0 | x_3^S) \exp\left(\frac{s}{c_0} \Delta x_3\right) + \hat{p}^{0,i}(x_3^0 | x_3^S) \exp\left(-\frac{s}{c_0} \Delta x_3\right) + \\ s^2 K \int_{x_3^0}^{x_3^1} \frac{c_0}{s} \sinh\left(\frac{s}{c_0}(x_3 - x_3^1)\right) \hat{p}^0(x_3 | x_3^S) dx_3. \end{aligned} \quad (3.20)$$

These equations can be solved easily by using the trapezoidal rule for the integrals over the area from x_3^0 to x_3^1 .

3.2.1 Derivation of imaging condition in 1D.

Consider the medium shown in figure 2.2, but with a laterally invariant lower half-space. Following the procedure explained in the first part of section 2.3.1 we can write for a one-dimensional wavefield in a horizontally layered 2-D medium:

$$\frac{s}{c_0}(\bar{p}^r - \bar{p}^i) = -sF\bar{p}, \quad (3.21)$$

where the operator F is defined as:

$$F = \sqrt{(\frac{1}{c_0})^2 - K}. \quad (3.22)$$

Note that the expression for Γ_0 has reduced to $\frac{1}{c_0}$. Again following section 2.3.1 we write:

$$\bar{p}^r + \bar{p}^i = \bar{p}. \quad (3.23)$$

Multiplying Eq. (3.23) by $\frac{1}{c_0}$ and adding the result to Eq. (3.21) leads to:

$$\frac{2}{c_0}\bar{p}^r = (\frac{1}{c_0} - F)\bar{p}. \quad (3.24)$$

Subtracting the same two equations leads to:

$$-\frac{2}{c_0}\bar{p}^i = -(F + \frac{1}{c_0})\bar{p}. \quad (3.25)$$

Multiplying Eq. (3.24) and Eq. (3.25) results in:

$$4(\frac{1}{c_0})^2\bar{p}^i\bar{p}^r = ((\frac{1}{c_0})^2 - F^2)(\bar{p})^2. \quad (3.26)$$

Substituting the expression for F we find the following imaging condition:

$$(\frac{1}{c_0})^2\bar{p}^r\bar{p}^i = \frac{1}{4}K(\bar{p})^2. \quad (3.27)$$

The imaging condition will now take the following form:

$$\hat{p}^r\hat{p}^i = \frac{c_0^2}{4}K(\hat{p})^2. \quad (3.28)$$

Since the imaging condition has to be applied at time $t = 0$ we write:

$$\mathcal{F}_t^{-1}[\hat{p}^r\hat{p}^i] = \frac{c_0^2}{4}K \times \mathcal{F}_t^{-1}[(\hat{p})^2], \quad t = 0, \quad (3.29)$$

where \mathcal{F}_t^{-1} stands for the inverse temporal Fourier transform. We assume $s = j\omega$. The numerical solution of Eq. (3.29) for the contrast function K is straightforward.

4

Evaluation of the one-dimensional case

In this chapter, some imaging results for synthetic 1D-data are given after which we will focus on several aspects of the layer-stripping method such as the wavelet, multiples and layer thickness and resolution. Some imaging results for oblique plane-wave incidence on a horizontally layered medium are given, followed by a comparison is made to a layer-stripping method based on the Schur algorithm.

4.1 Results for the 1D-case

The layer-stripping scheme was tested on a one-dimensional earth model shown in Figure 4.1. The earth model consists of several layers with a propagation velocity varying from 1500 m/s to 3200 m/s. The density is taken to be constant. The 1D synthetic data were generated in matlab using an acoustic reflectivity method, as developed by Kennett [20]. A Gaussian wavelet was used for modelling the reflected wavefield, a closer look at the wavelet will be taken in section 4.1.1. The synthetically generated reflected wavefield together with the imaging result is shown in Figure 4.2. The correspondence between the calculated velocities and the velocity model is very high. In the next sections we will treat several aspects of the layer-stripping method such as wavelet and multiples by zooming in on parts of the earth model.

4.1.1 Implementation of the imaging condition.

The imaging condition, Eq. (3.29) is valid only for the short period of time that there are only downgoing waves below the interface over which the contrast is calculated. In order to meet this requirement the imaging condition is defined as follows:

$$\mathcal{F}_t^{-1}[\hat{p}^r \hat{p}^i] = \frac{c_0^2}{4} K \times \mathcal{F}_t^{-1}[(\hat{p})^2], \quad t = 0. \quad (4.1)$$

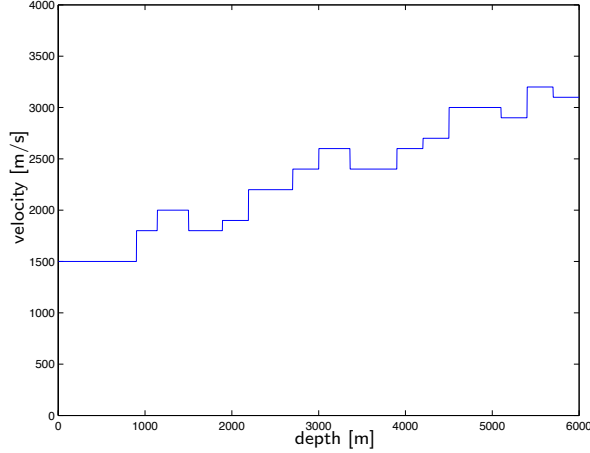


Figure 4.1: Propagation velocities for 1D earth model. The density does not vary.

In practice, taking only the value of the wavefields at time $t = 0$ when calculating the contrast from the imaging condition, does not give very accurate results. This is visible in Figure 4.3, which shows the velocities calculated using this method. The actual velocity model is denoted by the dashed line. In order to improve the accuracy of the method we decided to use a shifted causal wavelet. We assume that the sources that generate the acoustic wavefields are switched on at time instant t_0 , where $t_0 < 0$. The energy of the wavelet between $t = t_0$ and $t = 0$ is now taken into account in the evaluation of the imaging condition. We define:

$$\int_{-ws}^0 \mathcal{F}_t^{-1}[\hat{p}^r \hat{p}^i] dt = \frac{c_0^2}{4} K \times \int_{-ws}^0 \mathcal{F}_t^{-1}[(\hat{p})^2] dt, \quad (4.2)$$

where ws is the window size used for calculating the energy of the wavefield. To find the results in Figure 4.2 a window size of 1.4 s was used. The width of the non-causal part of the wavelet, t_0 , is approximately 0.04 s. Using a larger window size proved to give more accurate results than when using $ws = t_0$. Figure 4.4 shows a part of the calculated upgoing wavefields at increasing source and receiver depth. Note that as source and receiver are virtually moved downwards with every layer that is being stripped, the events in the data move towards time $t = 0$. When source and receiver have reached the same depth as a certain velocity contrast, the event caused by this contrast will keep its position at $t = 0$. The negative part of the t-axis is the part

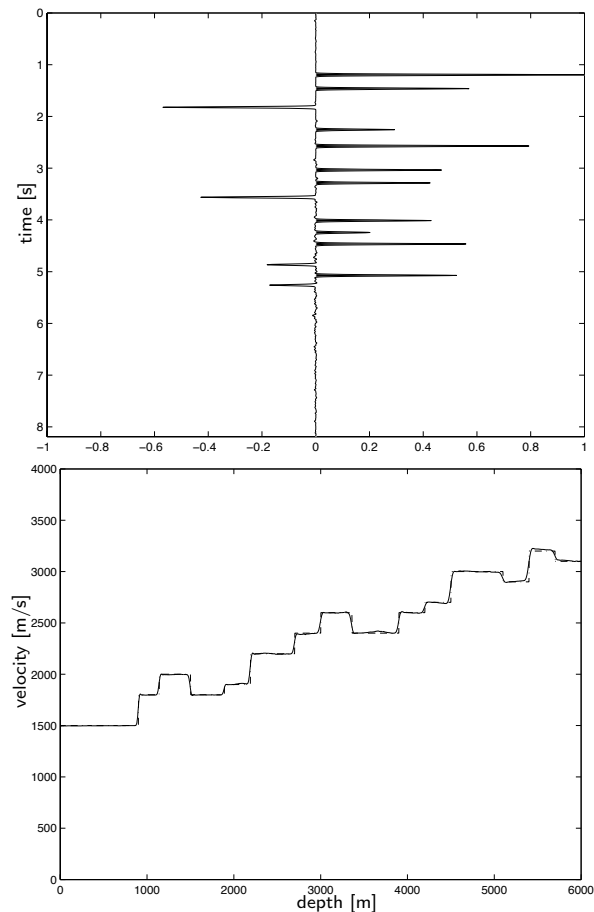


Figure 4.2: On the top the modelled upgoing wavefield and on the bottom the imaging result together with the earth model. (dashed).

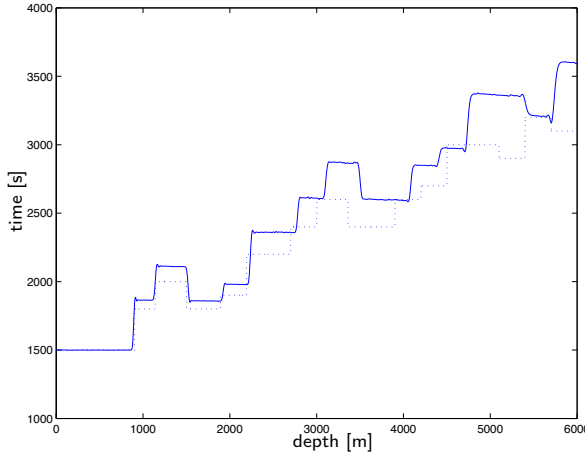


Figure 4.3: The imaging result together with the actual model (dashed). The values of the wavefields at time $t = 0$ were used to evaluate the imaging condition

used in the integral of the imaging condition, Eq. (4.2). A cosine taper is applied to the window over the wavefield. The value of the taper is 1 at $t = 0$ and 0 at $t = -ws$ where ws is the size of the noncausal window. This prevents artifacts to occur when the small events that travel through the noncausal part of the data reach the edge of the window. The contribution of these small events, results of the small mistakes in the layer extrapolation, is however not negligible. They play a major role in the stabilization of the method and considering them prevents the stack of mistakes as is common for most known layer-stripping methods. This stack of mistakes is visible in figure 4.3 where these events were not considered.

4.1.2 Wavelet

The wavelet was chosen such that its time rate of volume injection \hat{q}^s has a Gaussian distribution. \hat{q}^s is related to the wavelet \hat{W} as follows:

$$\hat{W}(s) = s\rho\hat{q}^s(s). \quad (4.3)$$

For convenience we will from now on refer to \hat{q}^s as the wavelet.

Figure 4.5 shows the wavelet in the time domain together with its frequency spectrum. Note that the frequency spectrum has a dc-component. This dc-component

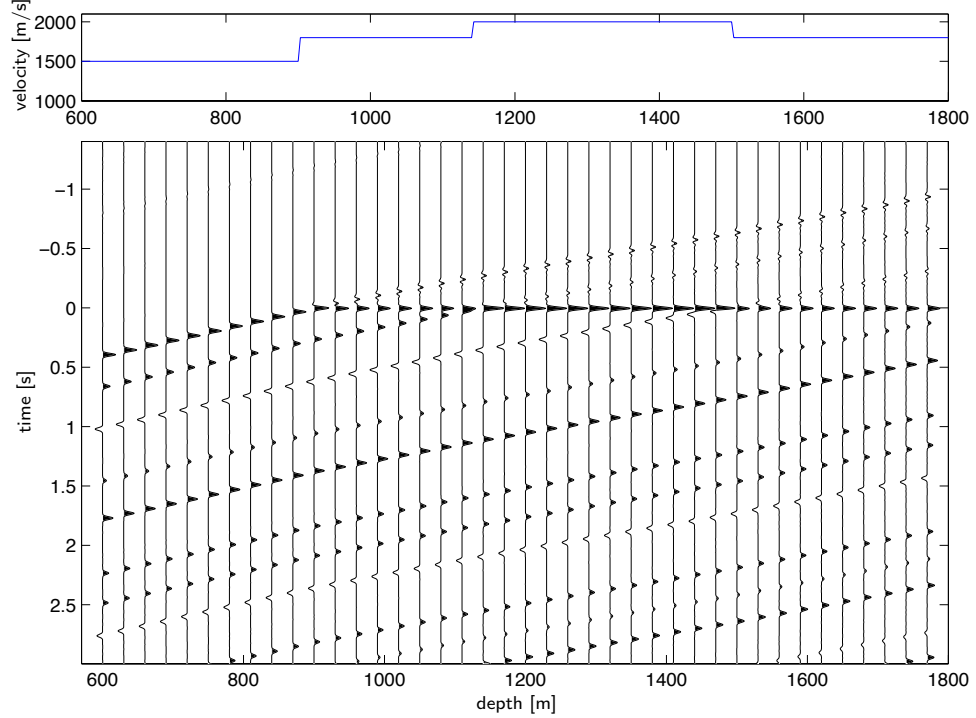


Figure 4.4: Calculated upgoing wavefields at increasing source and receiver depth.

has turned out to be crucial for the performance of the layerstripping method. A closer look at this property is taken in Chapter 5.

4.1.3 Internal multiples

In order to investigate how the layer-stripping method deals with the internal multiple reflections in the data we take a look at a velocity model with two interfaces, one at 300m and one at 900m depth. The synthetic data was modelled using the Gaussian wavelet shown in Figure 4.5. The imaging result is shown in Figure 4.6 together with the actual velocity model. The behavior of the multiple reflection while stripping the layers is made visible in Figure 4.7. The multiple at the start of the procedure is at about 1.4s. The more layers stripped, the closer both the multiple and the primary event that caused it move towards the $(t = 0)$ -axis. At a source

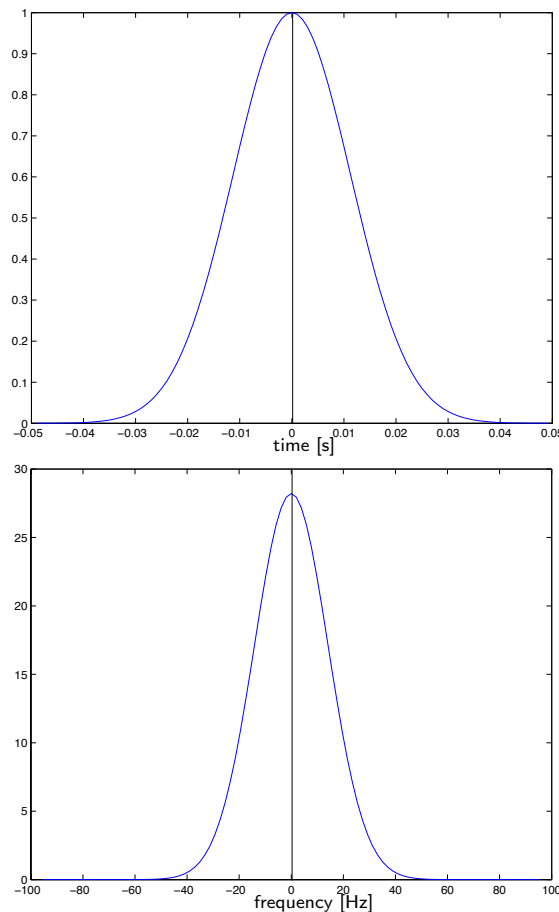


Figure 4.5: Gaussian wavelet in time (top) and frequency (bottom) domain.

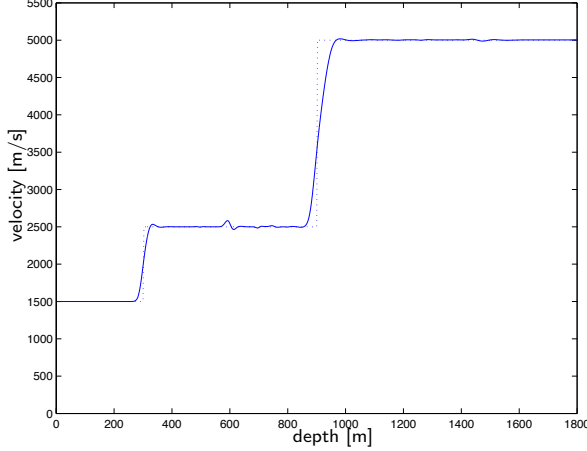


Figure 4.6: Velocity model with two reflecting interfaces (dashed line) together with the calculated velocities (solid line)

and receiver depth of 600 m the multiple is at 0.5 s. The multiple and its primary event reach the ($t = 0$)-axis at the same moment, after about 900 m of layers have been stripped. Had they not reached the axis at the same time, the multiple would have been treated as a separate event when applying the imaging condition. For means of visibility the amplitude of the multiple is enlarged in the wiggle plot of Figure 4.7. The size of the multiple in the separate traces shown below the wiggle plot is the actual size. The top picture shows the velocity model When we take a closer look at the first of our basic equations, Eq (2.42):

$$\begin{aligned}
 & s^2 K \hat{W} \int_{x_3^0}^{x_3^1} \frac{c_0}{2s} \exp\left(-\frac{s}{c_0}(x_3 - x_3^0)\right) \hat{p}^0(x_3 | x_3^S) dx_3 + \\
 & \exp\left(-\frac{s}{c_0} \Delta x_3\right) \hat{p}^{1,r}(x_3^1 | x_3^S) s^2 K \int_{x^0}^{x^1} \exp\left(\frac{s}{c_0}(x_3 - x_3^S)\right) \hat{p}^0(x_3 | x_3^S) dx_3 \\
 & = \hat{W}[\hat{p}^{0,r}(x_3^0 | x_3^S) - \hat{p}^{1,r}(x_3^1 | x_3^S) \exp(-\frac{s}{c_0} \Delta x_3)], \tag{4.4}
 \end{aligned}$$

the second and third term on the left-hand side can be recognized as a multiple generator term as described by van Borselen [35]. This term takes care of the correct handling of the multiples in the data. The small event at 600 m depth in Figure 4.6

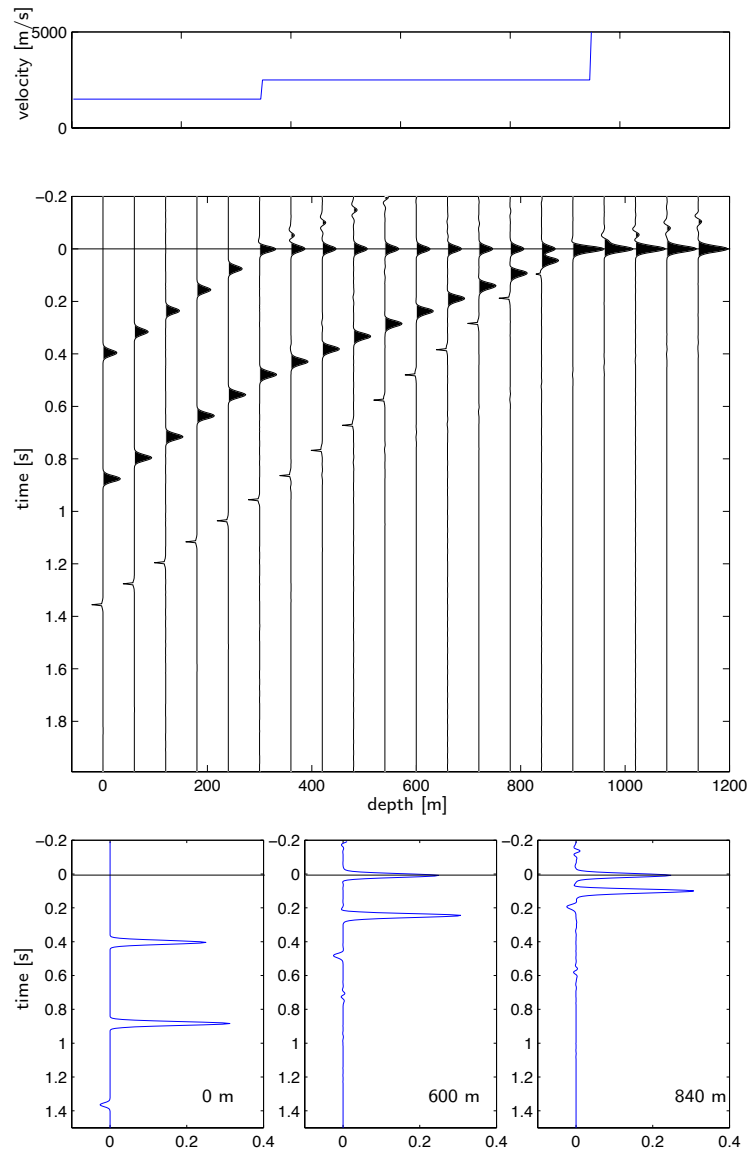


Figure 4.7: The upgoing wavefield at different source and receiver depths. At the top the velocity model.

is caused by miscalculations in the imaging procedure starting at about 300 m depth, when the first interface has reached the $t = 0$ -axis. The event caused by the second velocity contrast now starts to propagate towards $t = 0$ with a different speed than before. The small miscalculation however travels towards $t = 0$ with the old speed and causes the event visible at 600 m. The event does not result in a lasting change of the imaged velocity.

4.1.4 The influence of the thickness of stripped layers

Since the fields are sampled in time with time step Δt it is to be expected there is a relation between the thickness of the stripped layers, Δx_3 and Δt . It was found that for any time step the best results were achieved using:

$$\Delta x_3 = \frac{1}{2}(c_0 \times \Delta t) \quad (4.5)$$

This can be explained by the fact that when source and receiver are both moved downwards over Δx the travel distance of the wavefield is reduced by $2 \times \Delta x$. The layerstripping procedure is not extremely sensitive to the correct choice for Δx . Figure 4.8 shows the imaging result for 4 different layer thicknesses: $\Delta x = 1, 3, 6$ and 15 m. The time step used is 0.004 s, so the optimal layer thickness is 3m. For a layer thicknesses of 1m the difference is hardly visible and for a thickness of 6m only small deviations are visible at greater depths. For a layer thickness of 15m the mistake is much larger.

4.1.5 The resolution of the method

The resolution of the layer-stripping method is mainly determined by the resolution of the data and the width of the wavelet. In surface seismic surveys the frequency bandwidth is usually about 5-50 Hz, and the sound speed varies from about 2500 to 5000 m/s. This means the wavelengths of the acoustic waves, which determine the resolution in seismic images, are about 50 m or more. Figure 4.9 shows the imaging result for different velocity models. The model has four velocity interfaces: at 600m, 1200m, 1800m and 2400m respectively. The velocity varies from 2000m/s to 2200m/s, back to 2000m/s and 1800m/s, and then back to 2000m/s again. The wavelet used is the same as in the previous sections, shown in Figure 4.5. The figure top left shows this situation. In the figure at the top right, all velocity steps are divided in two steps of 100 m/s. These steps are also visible in the imaging result. Note that the small lobes in the imaging result at the interfaces are reduced in size. These lobes can be recognized as the 'ears' that occur as the result of Gibb's

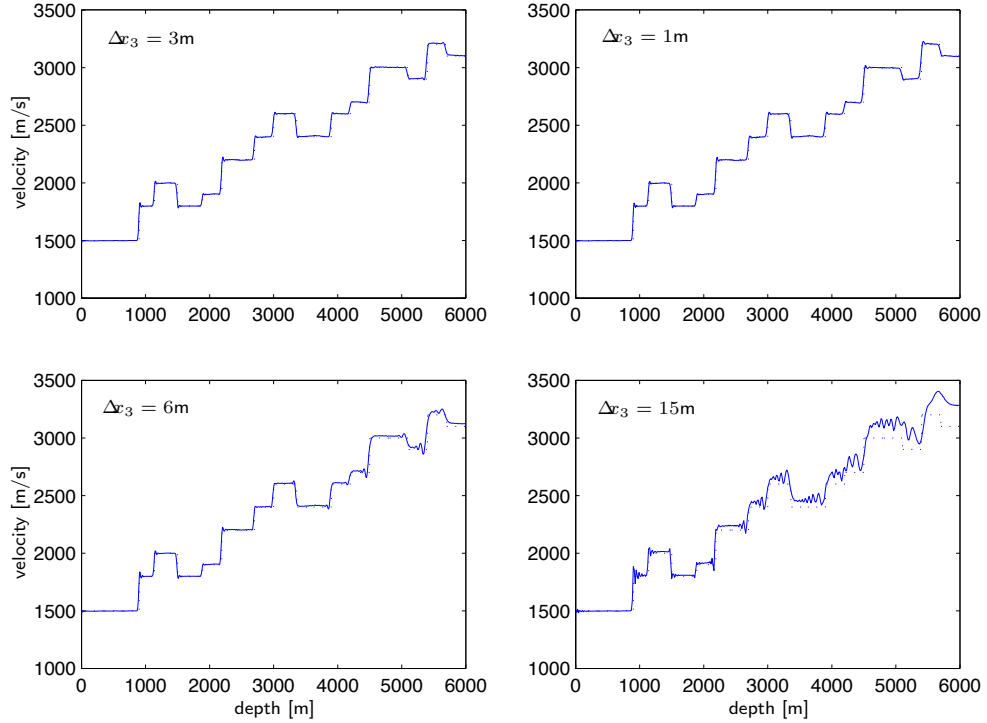


Figure 4.8: Imaging result together with actual model (dashed) for different layer thicknesses. Top left: $\Delta x_3 = 3\text{m}$, which is the optimal thickness. Top right: $\Delta x_3 = 1\text{m}$, bottom left: $\Delta x_3 = 6\text{m}$, bottom right: $\Delta x_3 = 15\text{m}$.

phenomenon. The figure on the middle left shows the case where the velocity step is divided in five steps. The individual steps are not recognizable anymore in the imaging result. The ears in the data have decreased even more. The figure on the middle right shows the case where the steps are taken at once again, but the thickness of the two layers with velocity 2200m/s and 1800m/s is much smaller. For a thickness of 150m the imaging result is still good as is the case for a layer thickness of 90m shown in the figure at the bottom left. When the layer thickness decreases to 60 m the imaging result does not reach the actual velocity anymore, especially for the higher velocities. This can be explained by the fact that for higher propagation velocities the events are closer to each other in time and will interfere sooner. Figure 4.10 shows the imaging result for the same velocity model as in Figure 4.9

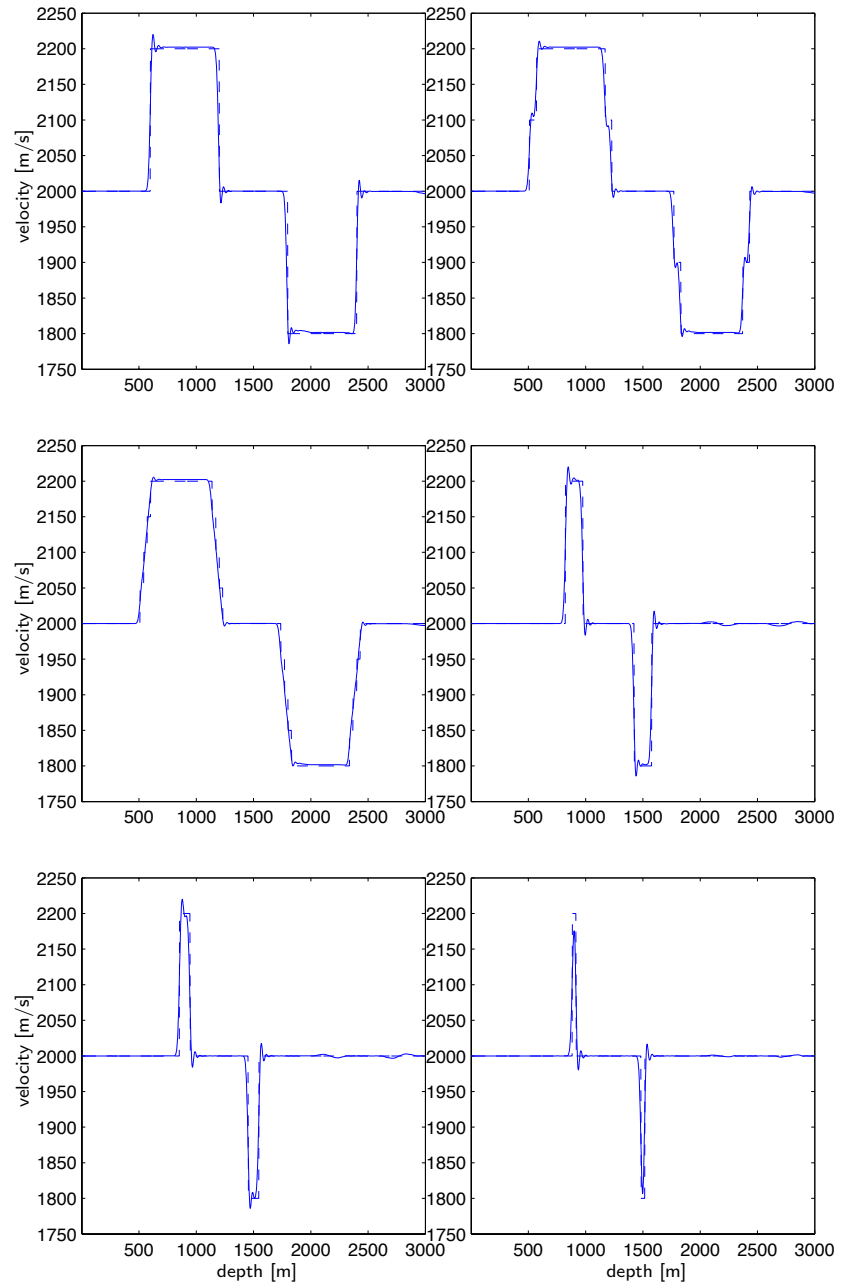


Figure 4.9: Imaging result together with actual model (dashed) for different velocity models.

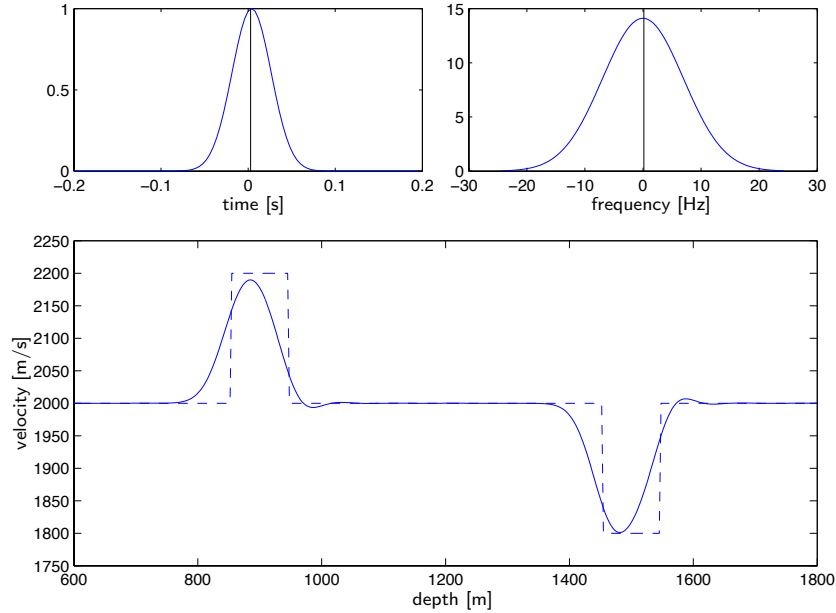


Figure 4.10: Imaging result together with actual model (dashed) for lower frequent wavelet. Top left: the wavelet in the time domain, top right: wavelet in the frequency domain.

bottom left, but for a different wavelet. As shown in Figure 4.10 this wavelet is has a smaller bandwidth and is therefore broader in the time domain. When a wavelet has a broader bandwidth the separate events will influence each other more, so the velocity results are less accurate then for the wavelet with smaller bandwidth used in Figure 4.9.

4.1.6 Results for oblique incidence

We will now take a look at an obliquely incident plane wave on a horizontally stratified two-dimensional medium. In Figure 4.11 a plane downgoing wave with propagation velocity c_0 has a wavefront making an angle ϕ with the horizontal axis. The direction of the ray normal makes the same angle ϕ with the vertical axis. The ray parameter, or horizontal slowness, p is defined as:

$$p = \frac{\Delta t}{\Delta x_1} = \frac{\sin \phi}{c_0}, \quad (4.6)$$

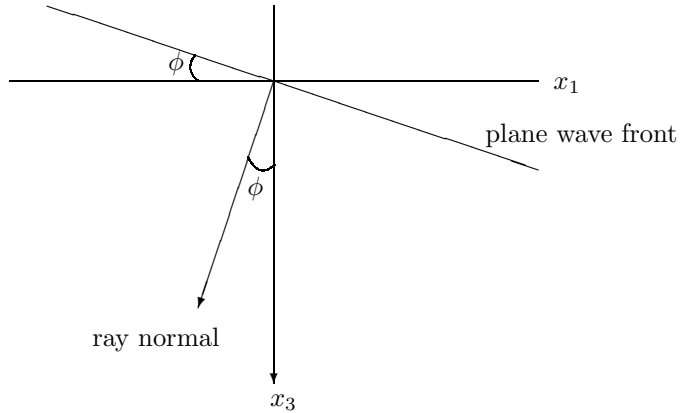


Figure 4.11: Obliquely incident plane wave.

where Δx_1 is the horizontal distance the wavefront propagates in a time increment Δt . The term $\frac{\Delta t}{\Delta x_1}$ is also known as the stepout per trace. Figure 4.12 shows the imaging results for different angles of incidence together with the model velocities. The synthetically generated reflected wavefields for the different angles of incidence that were used as input for the layer-stripping procedure are also shown. The imaging results were obtained considering the special case $s = j\omega$, where s is the Laplace parameter. In this case the slowness α must be taken imaginary. We therefore define the real slowness p which is related to α as:

$$p = j\alpha. \quad (4.7)$$

The spatial Fourier transform pair in a two dimensional medium is defined as:

$$\bar{u}(js\alpha, x_3, s) = \int_{x_1 \in \mathbb{R}} \exp(j s \alpha x_1) \hat{u}(x_1, x_3, s) dA, \quad (4.8)$$

$$\frac{1}{(2\pi)} \int_{s\alpha \in \mathbb{R}} \exp(-js\alpha x_1) \bar{u}(js\alpha, x_3, s) dA = \hat{u}(x_1, x_3, s). \quad (4.9)$$

When $s = j\omega$ and $p = j\alpha$ we can rewrite this as follows:

$$\bar{u}(sp, x_3, s) = \int_{(x_1) \in \mathbb{R}} \exp(spx_1) \hat{u}(x_1, x_3, s) dA, \quad (4.10)$$

$$\frac{\omega}{(2\pi)} \int_{(p_1) \in \mathbb{R}^2} \exp(-spx_1) \bar{u}(sp, x_3, s) dA = \hat{u}(x_1, x_3, s). \quad (4.11)$$

Equation (4.10) can be recognized as the temporal Fourier transform of the Radon transform. Application of this transform to the theory as described in section 3.1.1 is straightforward. From the results in Figure 4.12 it can be concluded that the imaging procedure gives good results for oblique incidence. Note that for postcritical incidence the method does not hold. This is the case when

$$\frac{1}{(c_n)^2} < \frac{(\sin\phi)^2}{(c_0^2)}, \quad (4.12)$$

where c_n is the velocity in the n -th layer. For an angle of incidence of 27 degrees the 'critical velocity' is 3300 m/s. As shown by Leyds and Fokkema [22], non-causal noise is generated when postcritical reflection occurs. This non-causal effect can be explained by the fact that the evanescent wave travels faster horizontally than the propagating wave and therefore creates a scattered field before the incident wave arrives. Since the derivation of our imaging condition is based on the causality principle, our method will fail for postcritical incidence. In Figure 4.12 the imaging result for an angle of incidence of 27 degrees becomes unstable before the critical point has been reached. This is a result of noise being generated during the layer-stripping procedure. The noise occurs as a result of the fact that the events in the data are very close together for higher angles of incidence, while the thickness of the stripped layers stays the same. If we reduce the thickness of the stripped layer from 3 meter to 0.5 meter, the result is improved and the noise is reduced. This is shown in Figure 4.13. The imaging result is less accurate for the deeper layers. In Figure 4.14 the imaging result, again for an angle of incidence of 27 degrees, is shown but now for lower model velocities and a thickness of the stripped layers of 3 meter. In this case the instability as a result of noise does not occur, and the imaging result is still accurate for deeper layers.

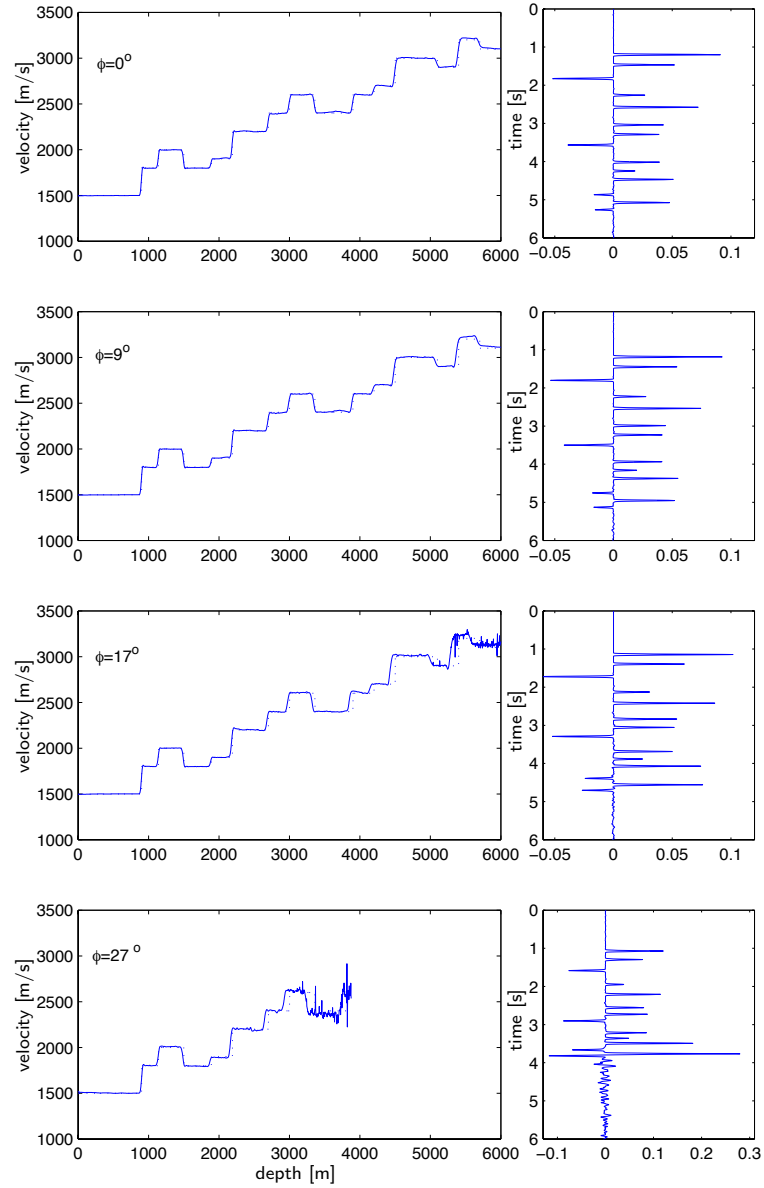


Figure 4.12: Imaging results together with actual model (dashed) for different angles of incidence ϕ .

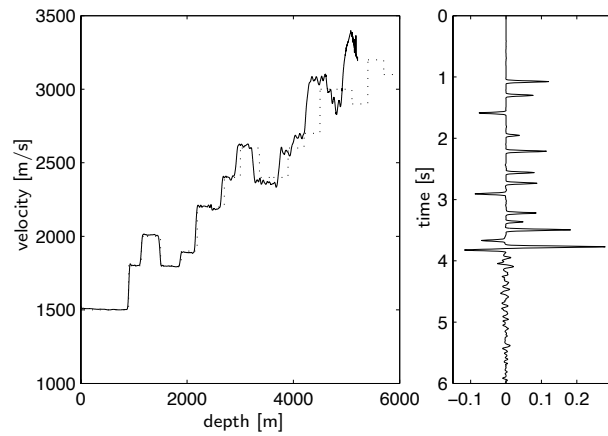


Figure 4.13: Imaging results together with actual model (dashed) for an angle of incidence of 27 degrees. The imaging result was achieved by reducing the thickness of the stripped layers to 0.5 m.

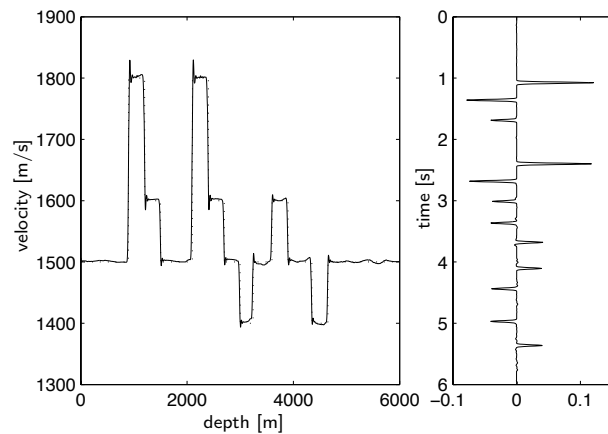


Figure 4.14: Imaging results together with actual model (dashed) for an angle of incidence of 27 degrees. The model velocities are lower than in the previous picture.

4.2 Comparison to Schur-algorithm

In order to evaluate the layer-stripping method using a causality-based imaging condition the method was compared to another layer-stripping algorithm, the Schur algorithm. The time domain version of this algorithm, also known as the fast Cholesky recursion, is known as a fast and efficient method. It is also known, as most layer-stripping methods, for its habit to stack mistakes at each layer-stripping step and increase the mistake with each step.

4.2.1 The Schur algorithm for the normal incidence problem

The Schur algorithm can be used to solve the inverse problem for a one-dimensional acoustic medium probed with plane waves. We will consider the case of plane waves at normal incidence. Following the derivation by Yagle and Levy [39], a two-component wave system is found:

$$\begin{aligned}\partial_\tau p^{\text{down}} + \partial_t p^{\text{down}} &= -rp^{\text{up}}, \\ \partial_\tau p^{\text{up}} + \partial_t p^{\text{up}} &= -rp^{\text{down}},\end{aligned}\quad (4.13)$$

where the reflectivity function $r(\tau)$ is given by

$$r(\tau) = \frac{1}{2}\partial_\tau \ln Z. \quad (4.14)$$

Z is the acoustic impedance and τ is the travel time. In the system of equations (4.13) p^{down} is the downgoing wave and p^{up} is the upgoing wave. Let the downgoing wave contain a probing impulse. By causality, both the upgoing and downgoing waves must be zero for $t < \tau$. The up- and downgoing waves can now be written as:

$$p^{\text{down}} = \delta(t - \tau) + \tilde{p}^{\text{down}}\chi(t - \tau) \quad (4.15)$$

$$p^{\text{up}} = \tilde{p}^{\text{up}}\chi(t - \tau), \quad (4.16)$$

where the tilde denotes smooth functions, and $\chi(t)$ denotes the unit step function. When Eqs (4.13) are combined with

$$r(\tau) = 2p^{\text{up}}(\tau, \tau), \quad (4.17)$$

the equations can be solved recursively. This system is known as the Fast Cholesky recursion. The derivation of the Fast Cholesky recursions following Yagle and Levy [39] is shown in appendix D, together with an alternative solution of the Schur algorithm.

4.2.2 Comparison of imaging results

The Fast Cholesky recursions were run on synthetic data with the same velocity profile as in Figure 4.1. In order to meet the requirements on the wavefield we used the wavelet shown in Figure 4.15. The imaging results together with the actual model for both methods are shown in Figure 4.16. The results for the causality-based imaging method are the same as in section 4.1. To investigate the performance of

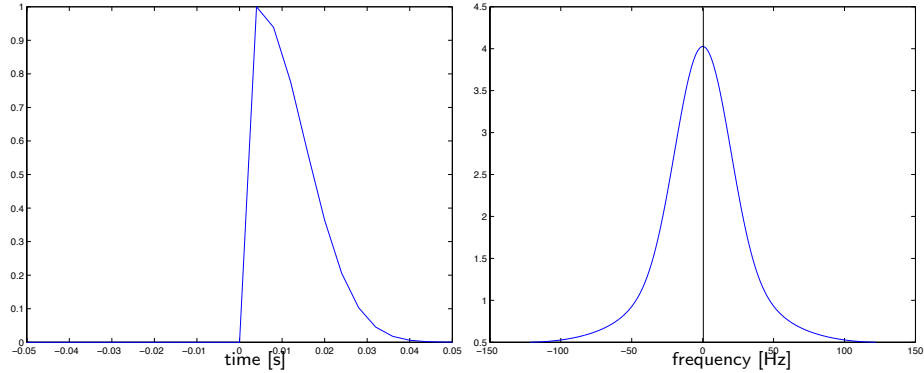


Figure 4.15: Wavelet used for generating synthetic data for Schur algorithm, in time domain (left) and in frequency domain (right).

both methods in case of the presence of noise, noise was added to the synthetic data. The signal to noise ratio is about 78. The imaging results for both methods are shown in Figure 4.17. On top are the reflected wavefields used as input for both methods. The difference between those wavefields is the wavelet used for generating the synthetic data. The wavelets used are the ones shown in Figures 4.15 and 4.5. Below the wavefields is the imaging result shown together with the actual velocities. Both methods seem not to have much problems with the noise, although the Schur method shows some deviations for greater depths. The causality-based method is only a fraction less accurate than when the data was noise-free, see Figure 4.2. Note that both methods are completely data driven methods, so if there are large discrepancies in the data, they will occur in the imaging result as well.

The biggest difference between the Schur-method and the causality-based imaging method is the fact that the latter method can be applied to media that are inhomogeneous both in the horizontal and the vertical direction, while the Schur-method

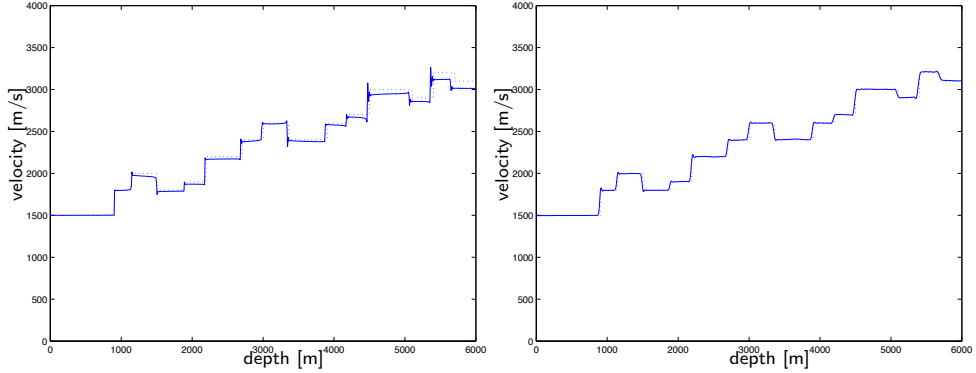


Figure 4.16: Imaging result obtained with Schur algorithm (left) and with causality-based imaging condition (right). The dashed line is the actual velocity model.

is only valid for 1D problems. Another difference is connected to the definition of the wavelet. While the causality-based imaging method can handle any wavelet containing low frequencies, the wavelet for the Schur-method is defined to contain a probing impulse. The value of this probing pulse in the reflected wavefield is used to determine the reflectivity function. This is in contrast with the causality-based method where the size of the reflected wavefield related to the incident and total wavefield gives the desired velocity. Since only the true value of the reflected wavefield is used in the Schur-method, using the energy of the wavefield as we explained in section 4.1.1 is not possible for this method. The use of the energy of the wavefield results in a stabilization of the layer-stripping which is missing in the Schur method. Another explanation for the stability of the results using the causality-based imaging method is the large window we use in the evaluation of the imaging condition. As visible in Figure 4.4 small miscalculations in the layer extrapolation are still considered in the imaging condition. When these miscalculations are not considered, we recognize in the imaging result the stacking of mistakes common for layer-stripping methods. This is visible in Figure 4.3.

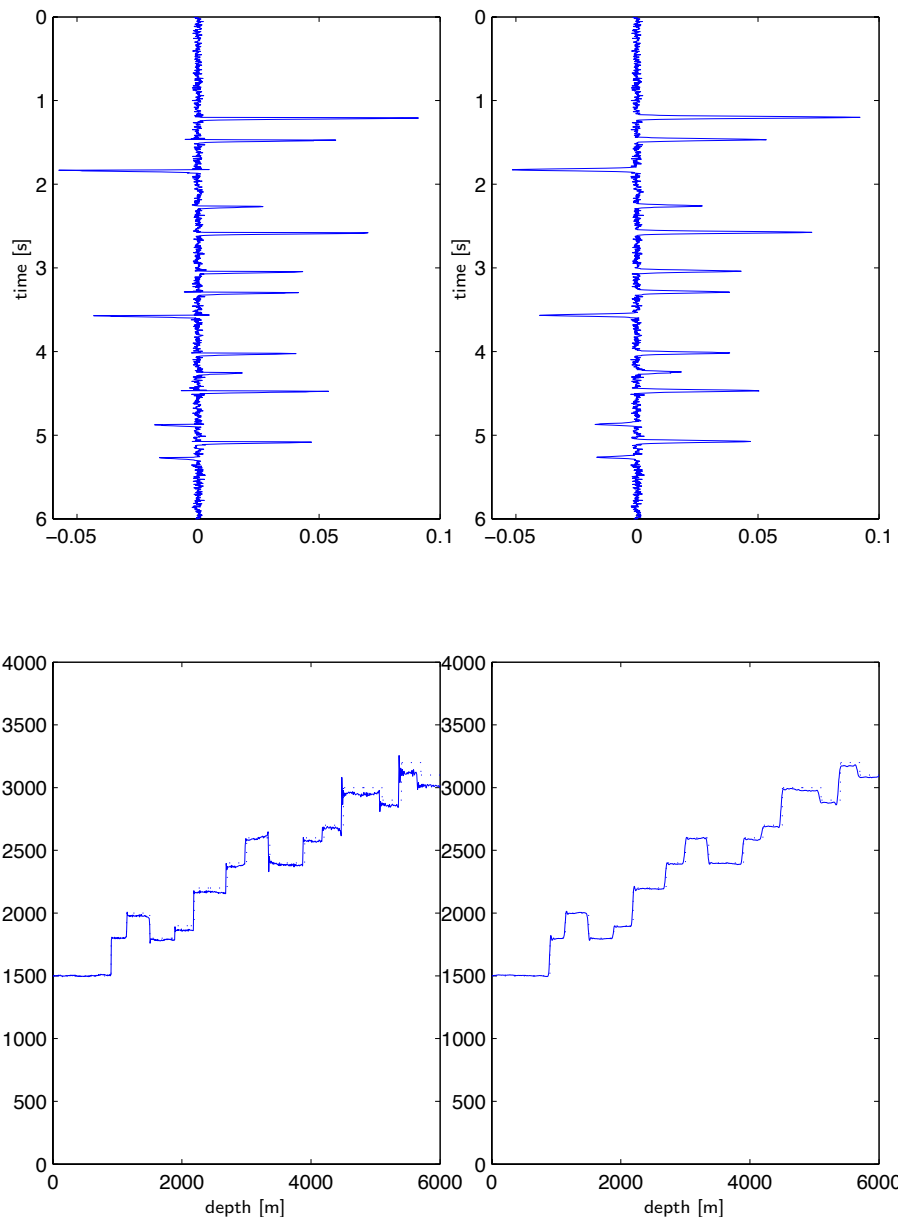


Figure 4.17: Imaging result for noisy data. Top left is the synthetically generated upgoing field used as input for the Schur method. The imaging result for this method are shown bottom left. The actual velocities are denoted by the dashed line. Top right is the upgoing wavefield used as input for the causality-based imaging method, the imaging result together with the actual velocities for this method are shown on the bottom right.

5

The lack of the lowest frequencies in seismic data

In the previous chapter we have used a Gaussian wavelet, containing all low frequencies, to model and image our data. Such a wavelet is however not realistic for seismic data since the lowest frequencies cannot be produced by the seismic source. When testing the imaging procedure for more realistic wavelets, we encountered the problem that these low frequencies are extremely important to the quantitative interpretation of seismic data. In this chapter a description of the problem is given and a solution method is proposed.

5.1 Problem description

In this section we will show what happens when the data lacks low frequency information. Figure 5.1 shows two different wavelets both in time and frequency domain. The Gaussian wavelet has a frequency spectrum containing all low frequencies, while the derivative of the Gaussian wavelet has a spectrum which is zero for 0 Hz, in other words which has no dc-component. Using these two wavelets, synthetic data were modelled. For simplicity, we will take a look at the first two interfaces of the velocity model we used so far (see Figure 4.1). The new input velocity model has two contrasts, one at 900 m and one at 1140 m depth. The velocity varies from 1500 m/s to 1800 m/s and 2000 m/s. Imaging using the causality-based imaging method gives good results for the Gaussian wavelet and no usable results when the derivative of a Gaussian wavelet was used. This is visible in Figure 5.2. The imaging result for the derivative of a Gaussian becomes very large at a depth of about 70 m, long before the first interface is reached. The reason for this instability is that when using the energy of the wavefield in the imaging condition, a division by the wavelet is performed when evaluating this imaging condition. This corresponds to a division by zero when the dc-component is missing. To illustrate the problem further, we use

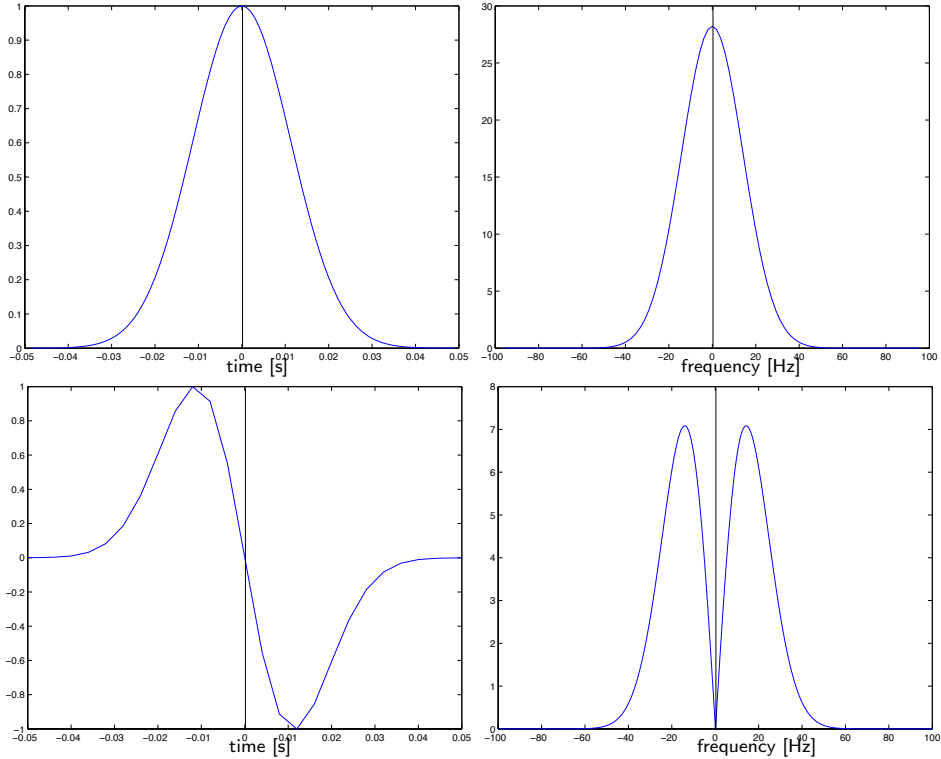


Figure 5.1: Top: Gaussian wavelet in time (left) and frequency (right) domain. Bottom: Derivative of Gaussian wavelet in time and frequency domain.

a very small window size for calculating the energy of the wavefields, as described in section 4.1.1. The window size used in Figure 5.3 is 0.02 s. The window size used to find the results shown in Figure 5.2 is 1.4 s. The results for the wavelet that does not contain the zero-frequency are less accurate than when a larger window was used, but the wavelet that does not have all low frequencies now at least gives a stable result. This result is however not satisfactory since although the velocity contrasts cause a response in the imaging result, the imaged velocity between the contrasts is the same as the background velocity. To further illustrate the problem we use a wavelet that has roughly the same shape in the time domain as the derivative of a Gaussian wavelet. It has a positive peak in the non-causal part and a negative peak in the causal part of the time domain. The wavelet is composed by computing

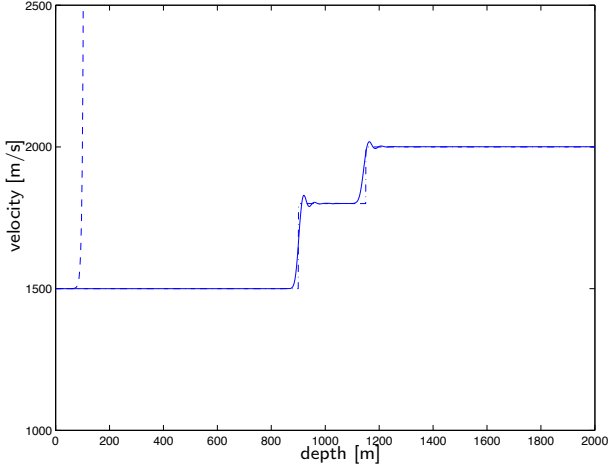


Figure 5.2: Imaging result for synthetic data modelled using a wavelet that contains all low frequencies (Gaussian) and a wavelet that does not (derivative of Gaussian). The wavelet without dc-component does not give a stable result (dashed line), while the results for the wavelet that does have a dc-component are good (solid line). The true velocity model is given by the dash-dotted line.

the Hilbert transform of the Gaussian wavelet (see appendix C.2), therefore the frequency content of both wavelets is comparable. The wavelet is shown both in time and frequency domain in Figure 5.4. The imaging result shown in Figure 5.5 does not encounter the same problem as is the case for the derivative of the Gaussian wavelet. A window size of 1.4 s was used in the evaluation of the imaging condition. The imaging result is less accurate than for a Gaussian wavelet because of the large width of this particular wavelet in the time domain. This result is consistent with our assumption that the cause of the problems is the lack of the dc-component in the wavelet and not the shape of the wavelet in the time domain. This is in spite of the fact that the actual imaging is performed using the energy of the wavefields in the time domain. The reason for failure of the method when the lowest frequencies are missing can be found in the spectral information of the desired velocity function. This spectral information contains a broad range of wavenumbers, including small wavenumber components. It is not possible to recover these small wavenumber components from the data when the data does not contain low frequency information. Some theoretical inversion methods ignore this problem, such as the method described by Raz [25]. In those cases it is assumed that the data can be properly de-

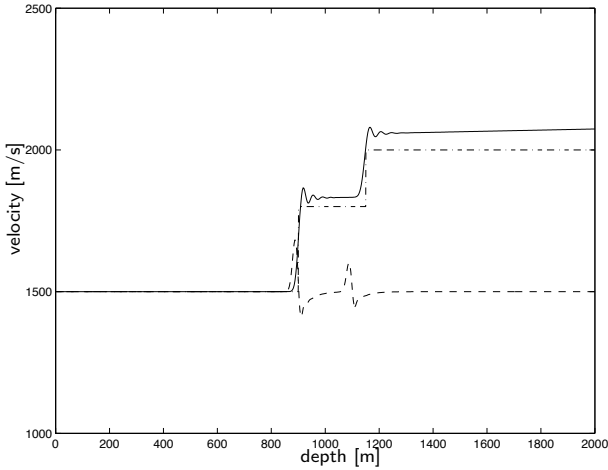


Figure 5.3: Imaging result for synthetic data modelled using a wavelet that contains all low frequencies (solid line) and a wavelet that does not (dashed line). A very small window (0.02 s) was used to evaluate the imaging condition. When the wavelet has no dc-component, the imaging procedure 'sees' the interface, but does not reach the correct velocity. The true velocity model is given by the dash-dotted line.

convolved in order to recover the reflectivity sequence. This is explained by Treitel, Lines and Ruckgaber [33]. An ideal wavelet deconvolution corresponds to the case where we have a full-band zero-phase wavelet. The method by Schur, described in the previous chapter, requires a wavelet initiated by an impulse containing the low frequencies. The velocity inversion procedure described by Cohen and Bleistein [11] makes an estimate of the velocity deviation from a certain background velocity by considering only the available frequency bandwidth. They assume that the velocity variations in the subsurface are small. They use a technique that determines the derivative of the velocity deviation from the background velocity. This derivative is band-limited. Some inversion methods use background velocity information to add the missing frequencies to the inversion result. One of those methods is the method described by Carrion and Kuo [6], where a minimization technique is used to find the critical path of the wave field in the $\tau - p$ domain. Low-frequency information can be derived from for instance well log-data, as described by Treitel [33], or time migration velocities. We performed experiments where a background velocity model was included in the imaging procedure but this did not lead to satisfactory results. In the following sections we propose a method that does not make use of a back-

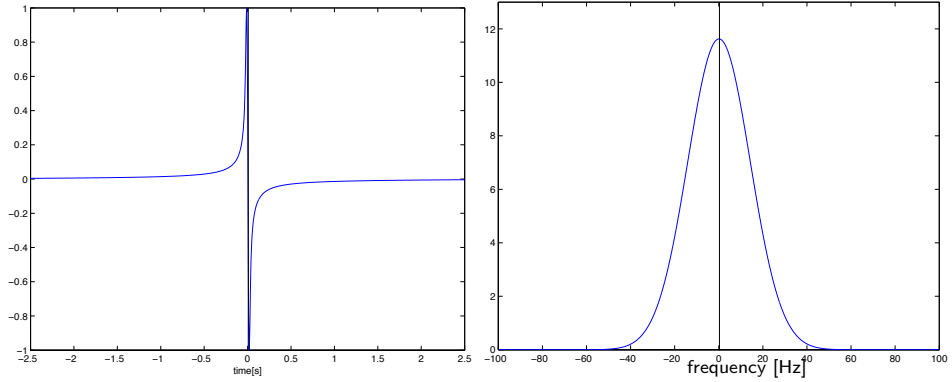


Figure 5.4: Wavelet based on the Hilbert transform of a Gaussian in the time (left) and frequency (right) domain.

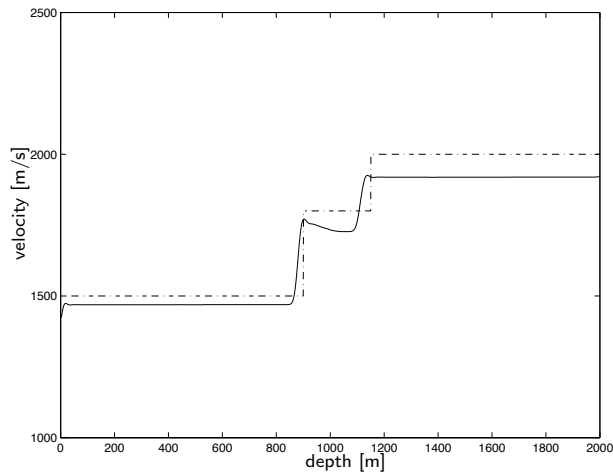


Figure 5.5: Imaging result for synthetic data modelled using a wavelet based on the Hilbert transform of a Gaussian. The true velocity model is given by the dash-dotted line.

ground velocity model, but does take care of the required frequency content of the data.

5.2 The envelope method

In this section we propose a method to add low-frequency content to the data without using a background velocity model. To do this, we use the envelope of the data in the imaging procedure. The envelope of a wavelet W is defined as follows:

$$\text{envelope}(t) = \sqrt{W(t)^2 + \mathcal{H}[W(t)]^2}, \quad (5.1)$$

where $W(t)$ is the wavelet and \mathcal{H} denotes the Hilbert transform. We will take another look at the case where the derivative of a Gaussian is used for the wavelet.

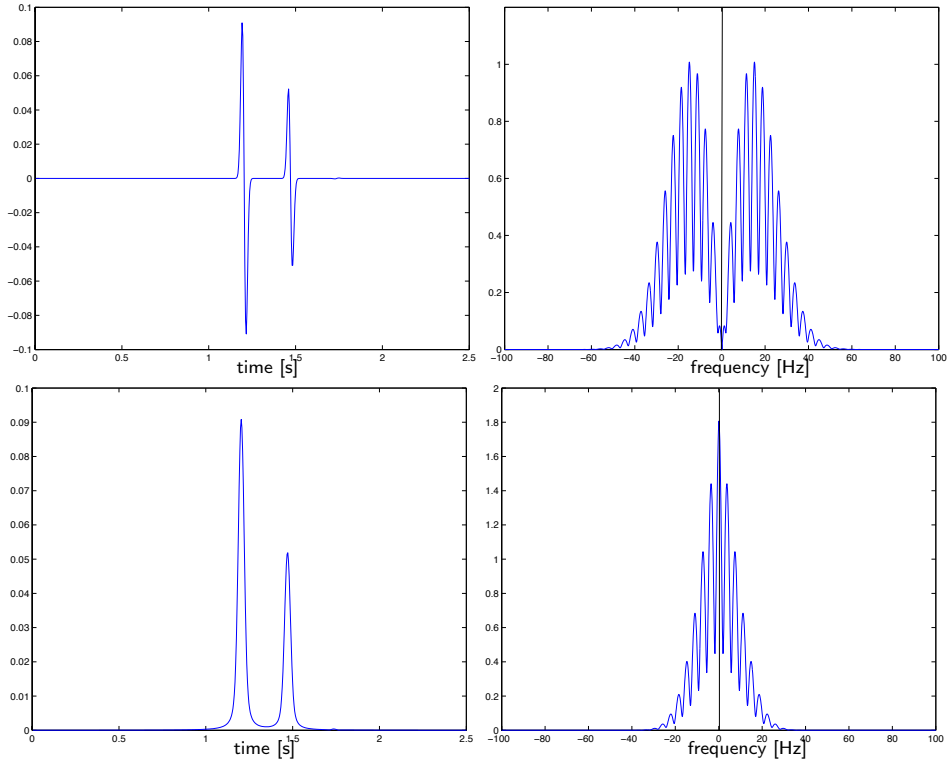


Figure 5.6: The synthetic upgoing wavefield, used as input for the layer-stripping process, both in time and frequency domain. Top: the original wavefield. Bottom: the upgoing wavefield after the envelope was taken. The two events correspond to the two interfaces in the velocity model.

The synthetically generated upgoing wavefield in the time and frequency domain using this wavefield and the same for its envelope are shown in Figure 5.6. When the envelope of the wavefield is taken, its frequency spectrum contains the desired dc-component. The velocity model used for modelling the data is the same as the one used in the previous section. The velocity results after taking the envelope of the wavefields are shown in Figure 5.7. The dashed line denotes the actual model velocities. Note that the final value of the calculated velocity is approximately correct, but the exact position of the interfaces is not as clear as in previous results. This loss of resolution is a result of the fact that the wavelet is much broader in the time domain after the envelope is taken. Using a wavelet with a broader frequency band results in higher resolution. Also note that the imaged velocity starts to rise again at about 1800 m depth. This is the result of the fact that the internal multiples have been given a positive sign after taking the envelope of the wavefields. This will be explained in section 5.4. Testing of the envelope method on other wavelets such as a Ricker wavelet also gave good results.

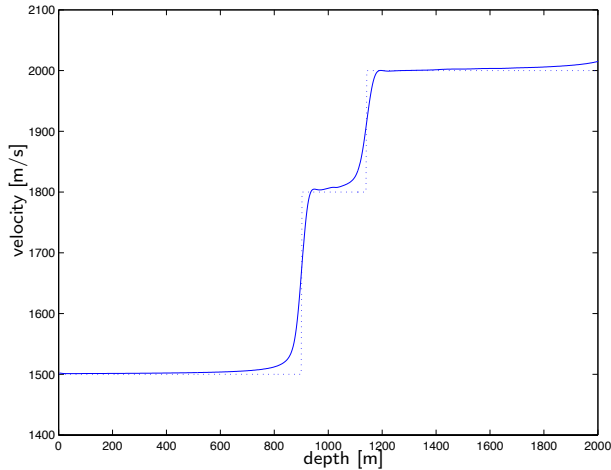


Figure 5.7: Results for the envelope method, calculated velocities together with the actual velocity model (dashed).

When applying this method we take the envelope of the measured wavefields and perform both the imaging and the wavefield extrapolation using these adjusted wavefields. A slightly different method is to take the envelope of the wavefields before

calculating the imaging condition and after extrapolation of the fields. After calculation of the contrast the original wavefields (without taking the envelope) are extrapolated over the next layer. Then the envelope is taken again and the new contrast determined, etc. The velocity results for this method however are unsatisfactory. This can be explained by the fact that the imaged velocity and the wavefield extrapolation method are very closely related. The wavefield is propagated using the imaged velocity. If the imaged velocity is based on properties that the wavefield to be extrapolated does not have, the wavefield will not be propagated appropriately and the method will fail.

A different way of dealing with the lack of low frequency problem might be by the following method: First, low-resolution velocity information could be found by taking the envelope of the wavefield. Then, this low-resolution information could be used as background velocity information when imaging with the original wavefields. Since experimenting with this method so far did not lead to satisfactory results this should be a subject of further research.

5.3 The absolute value method

An alternative for the envelope method, based on the same principle, is given in this section. Good results are obtained when the absolute value of the measured wavefields is taken at the beginning of the layer-stripping procedure. Like with the envelope method, both the extrapolation of the wavefields and the calculation of the contrast with the imaging condition is performed with the absolute value of the wavefields. The absolute value of the upgoing wavefield together with its frequency spectrum is shown in Figure 5.8. Note that the frequency spectrum now contains the desired dc-component. We used the same velocity model as in the previous section. The imaging result of this method is shown in Figure 5.9. An improvement of the

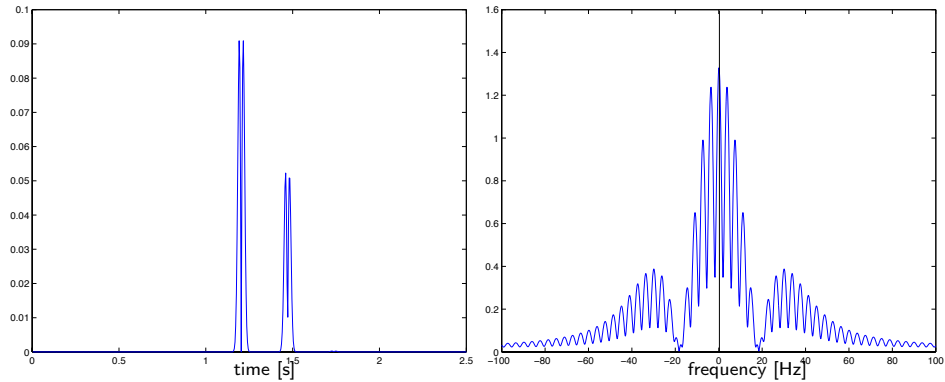


Figure 5.8: The absolute value of the (synthetic) upgoing wavefield, used as input for the layer-stripping process, both in time and frequency domain. The two events correspond to the two interfaces in the velocity model.

resolution can be seen in comparison to the envelope method. The little 'ear' at the velocity steps is now bigger than for the envelope method. This is related to the fact that the velocity step is now more sudden. This behavior can be recognized as Gibb's phenomenon. Testing of the absolute value method on other wavelets such as a Ricker wavelet gave good results.

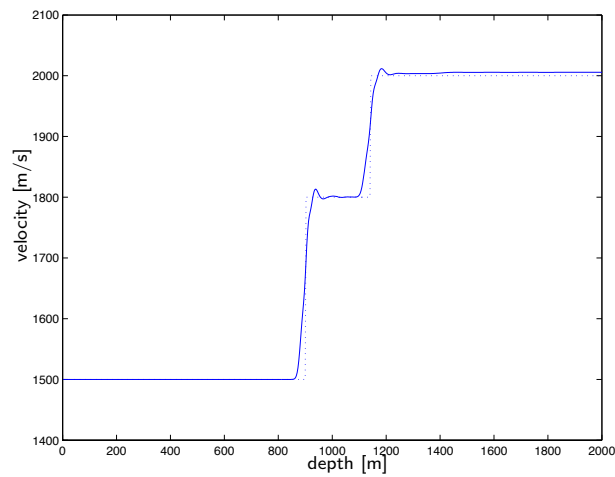


Figure 5.9: Results for the absolute value-method, calculated velocities together with the actual velocity model (dashed). The absolute value of the wavefields was taken at the beginning of the layer-stripping procedure. The derivative of a Gaussian was used as input wavelet.

As we stated before, the reason for failure of the imaging method when the lowest frequencies are missing is that the spectral information of the desired velocity profile contains small wavenumber components. This means that the desired low-frequency information somehow has to be added to the data or to the imaging result. The common method in seismics is to add this information to the imaging result by using background velocity information. The absolute-value or envelope method however adds low-frequency information directly to the data. The underlying assumption is that the events in the data are separate events. For this reason, the method will fail for overlapping events, as is shown in Figure 5.10. The imaging method is performed on a velocity model with three interfaces at 900, 910 and 920 m. depth. Due to the bandwidth of the wavelet, the events in the synthetic data that correspond to these interfaces will overlap. The imaging result of the reflection response modelled with a Gaussian wavelet, containing low frequencies, is very good, while the imaging result of the reflection response modelled with the derivative of a Gaussian in combination with the envelope and absolute-value method does not reach the correct velocity.

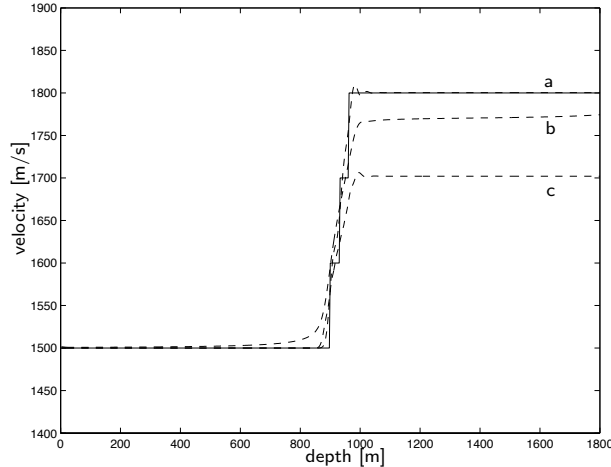


Figure 5.10: Imaging result for a Gaussian wavelet (a), for the derivative of a Gaussian using the envelope method (b) and for the derivative of a Gaussian using the absolute value method (c). The solid line denotes the true velocities.

5.4 Negative velocity contrasts

Because both the envelope and the absolute value method result in a loss of the sign of the events in the data, these methods fail for negative velocity contrasts. The multiple reflections in the data will no longer be handled correctly either. In this section we propose a solution method for this problem.

After the absolute value or envelope of the wavefield is taken the method sees a negative contrast as a positive one. The imaging result for a velocity model which has a negative contrast is shown in Figure 5.11. The true velocity varies from 1500 m/s to 1800 m/s and 2000 m/s and then back to 1800 m/s. The imaged velocity however varies from 1500 m/s to 1800 m/s to about 2230 m/s. The negative velocity contrast was interpreted as a positive one.

To show what happens when an internal multiple in the data does not have the correct sign we take another look at the velocity model used in section 4.1.3. The velocity varies from 1500 m/s to 2500 m/s at 300 m depth to 5000 m/s at 900 m depth. Figure 5.12 gives the imaging result using the absolute value of the wavefields. The actual velocity is given by the dotted line. The multiple now has the wrong sign, resulting in the imaged contrast at 2200m. When the multiple is manually given the correct sign, the imaging result as shown in Figure 5.13 is found. The faulty contrast at 2200 m is no longer there. We will take a closer look at the behavior of the multiple in Figure 5.14. Shown are the calculated upgoing wavefields at 660 m and 1200 m depth for the case where the sign of the multiple was not corrected (top) and for the case that the multiple was given the correct sign (bottom). When the sign of the multiple is not correct, the event at 0.7 s was not recognized by the imaging procedure as a multiple, but is treated as a primary. The same event is visible at about 0.4 seconds at 1200 m depth (top right) and will cause the faulty contrast at about 2200 m when it reaches the $t = 0$ -axis. The event at 0.4 s in the picture top left is generated by the multiple generator in the imaging procedure as a compensation for the missing multiple. The timing of this event corresponds to the timing of the multiple that was given the correct (negative) sign as visible in the picture bottom left. The small event still visible at 0.7 s is the result of slight miscalculations in the imaging procedure. As shown by the figure on the bottom right, at 1200 m depth this event has faded away and will hardly influence the imaging result.

A solution method for this problem is to determine the sign of the events before taking the envelope or the absolute value, and then to apply this sign to the resulting data. We use a median filter to determine the sign of the events. Median filters are commonly used in seismics in order to despike the data, as described by Claer-

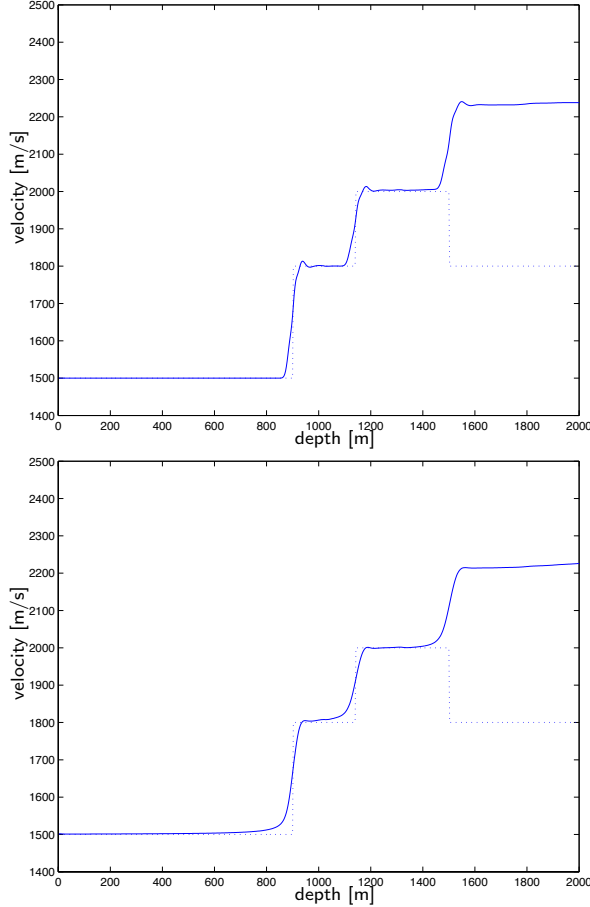


Figure 5.11: Imaging result for both the absolute value-method (top) and envelope method (bottom) together with the actual velocity model (dashed) which contains a negative velocity contrast. The derivative of a Gaussian was used as input wavelet.

about and Muir [9]. Other applications are the attenuation of coherent wavefields, described by Duncan and Beresford [15], or upgoing-downgoing wavefield separation in VSP data processing as described by Reiter *et al.* [26]. A median filter sorts the data points inside a certain window in ascending order. The median value of the numbers inside this window is simply the central value. Filtering of a trace is performed by passing the window over this trace and replacing each data point in

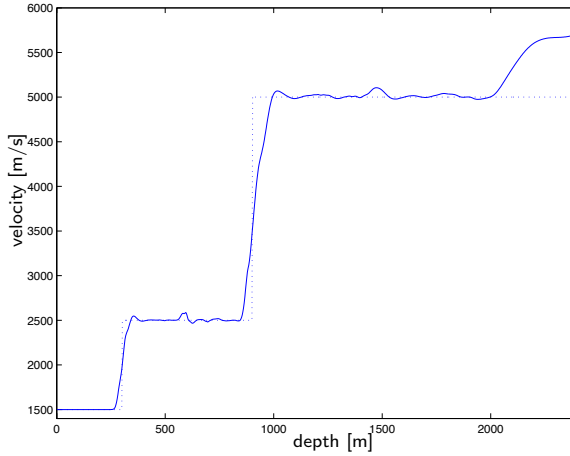


Figure 5.12: Imaging result using the absolute value method. The event at 2200 m depth is caused by the incorrect sign of the internal multiple. The actual velocity is given by the dotted line. The derivative of a Gaussian was used as input wavelet.

the trace with the median value of the points within the window centered on the current point. The window is shifted over the entire length of the trace, leaving a new, filtered trace. Before applying the median filter we transform the wavefield such that the events are symmetric (zero-phasing). For an anti-symmetric wavelet such as the derivative of a Gaussian we use a Hilbert transform for this. The next step is to apply the median filter to this zero-phased upgoing wavefield. A trace containing the sign of the events in the original data is now computed by assigning the value -1 or +1 to every negative or positive point in the filtered trace respectively. The absolute-value data or envelope data are now multiplied by this trace in order to assign the correct sign to the events in this data. Using a median filter proved to give better results than using a mean filter. The choice of the width of the median filter window is important. If the window is chosen too wide, the events will overlap and if the window is chosen too small, the result will almost be the same as the original data. This is shown in Figure 5.15. Shown from left to right are the synthetic upgoing wavefield, the wavefield after zero-phasing, the filtered result for a window size of 0.12 s, the filtered result for a window size of 0.04 s and on the right the filtered result for a window size of 0.28 s. The filtered result, from which we compute the trace containing the sign of the original data, is best for a window size of 0.12 s. Note that we expect a positive event to lead to a positive

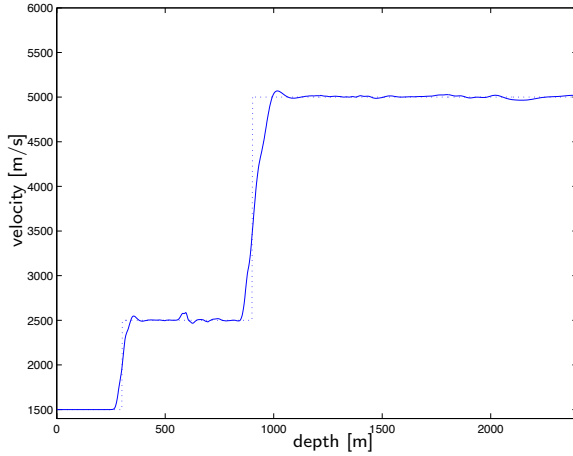


Figure 5.13: Imaging result using the absolute value method. The sign of the multiple was corrected manually. The actual velocity is given by the dotted line. The derivative of a Gaussian was used as input wavelet.

sign. In this case it's the other way around, which is a result of the shape of the wavelet after zero-phasing. This can easily be corrected for by median filtering the zero-phased wavelet and checking the sign of the result. The trace containing the sign of the original data, together with the result of application of this trace to both the absolute value and the envelope of the data is shown in Figure 5.16. The data after application of the trace give the imaging results shown in Figure 5.17. Since the absolute value method has higher resolution we will just use this method in the following example. Figure 5.18 shows the imaging result for the multi-layered depth model we used in the previous chapter. Figure 5.19 shows the synthetic upgoing wavefield after manipulation with the trace containing the sign of the events in the original data, which is also shown in this figure. The result is slightly less accurate than the result shown in Figure 4.1. This is the consequence of very small events or artifacts being given the wrong sign. The high amount of sign changes in the last second of the data is a result of the very small changes around zero in this part of the data. Since these changes are very small, the sign changes will hardly affect the imaging result. Note that the method to determine the sign of each event in the data will fail when events with an opposite sign are overlapping. Also note that, as stated in section 5.3, by using the envelope or absolute value of the data the assumption was made that the events are not overlapping, so this makes two reasons for the

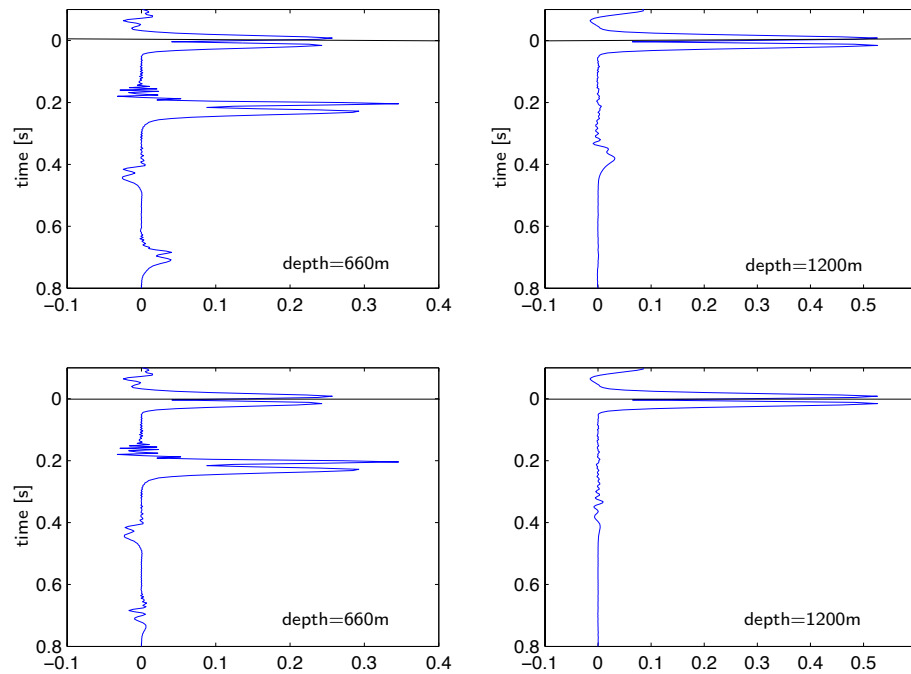


Figure 5.14: Calculated upgoing wavefields at 660 m (left) and 1200 m (right). In the two top pictures the sign of the internal multiple has not been corrected, in the two bottom pictures it has been given the correct (negative) sign.

method to fail in case of overlapping events.

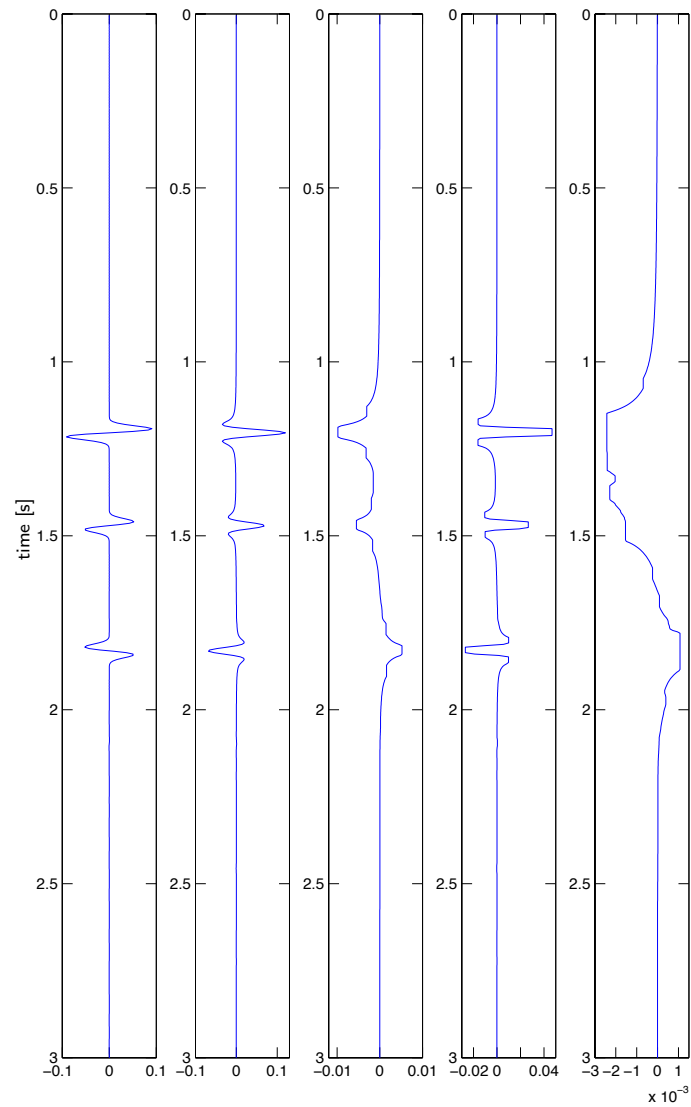


Figure 5.15: From left to right: The original synthetic trace, the zero-phased trace, the zero-phased trace after filtering with the right window size, after filtering with a too small window size, and on the right after filtering with a too big window size.

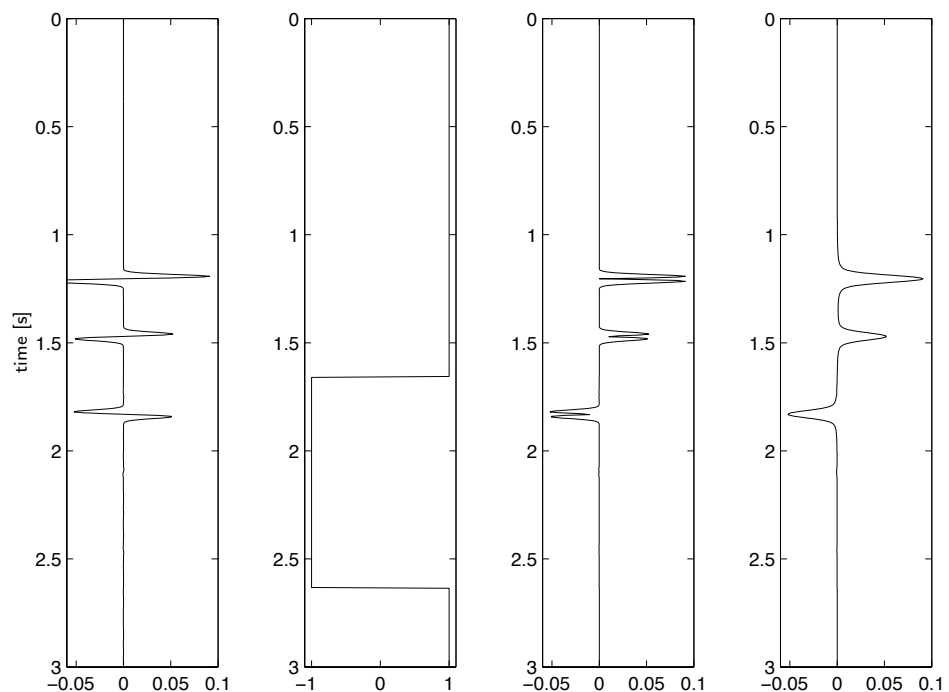


Figure 5.16: The picture on the left shows the synthetic upgoing wavefield. The trace containing the sign of the data which was found by filtering the original upgoing wavefield is shown on the middle left. The picture in the middle right shows the reflected wavefield after manipulation with the correct sign, used for the absolute value method. The picture on the right shows the same but now for the envelope method.

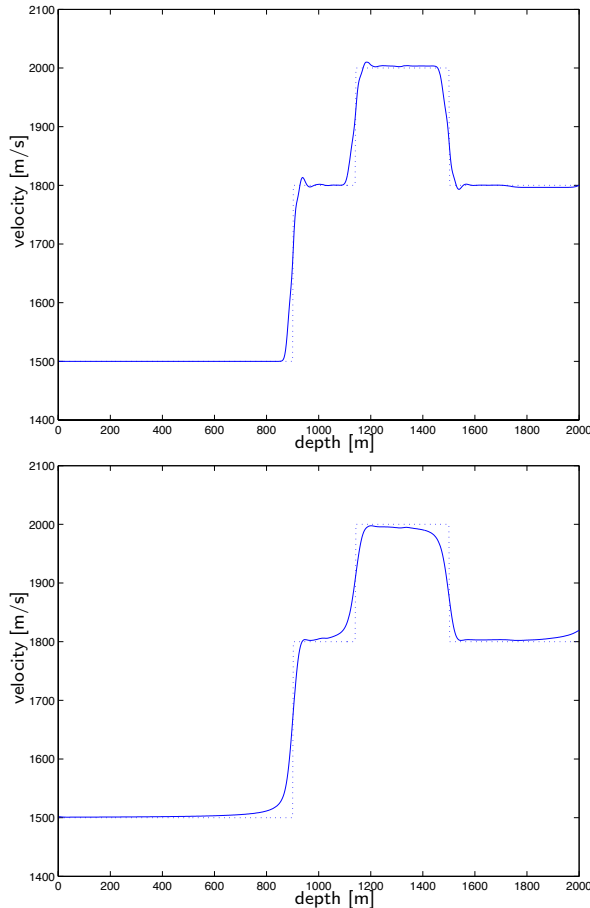


Figure 5.17: Imaging result for the both the absolute value-method (top) and envelope method (bottom) together with the actual velocity model (dashed) which contains a negative velocity contrast. The reflected wavefields were filtered to find a trace containing the sign of the original data which was applied to the data. The derivative of a Gaussian was used as input wavelet.

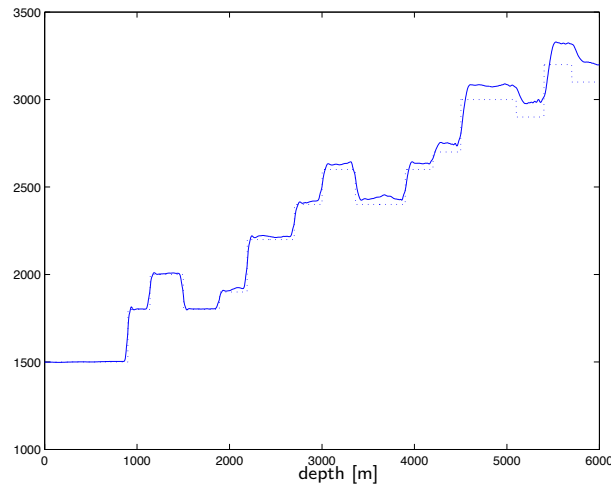


Figure 5.18: Imaging result for the absolute-value method after correction for the sign. The dotted line denotes the true velocities.

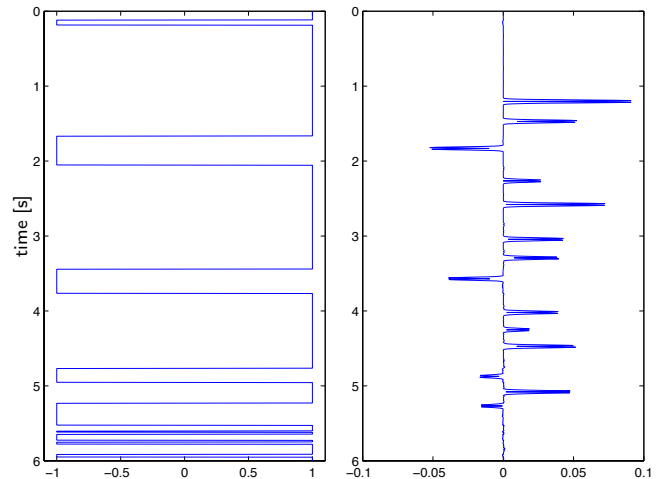


Figure 5.19: The left picture shows the trace containing the sign of the original data which was found by filtering the original upgoing wavefield. The picture on the right shows the reflected wavefield after manipulation with the right sign for the absolute value method.

6

Some applications of the layer-stripping method.

In this chapter we discuss some applications of the layer-stripping method. We give some examples of how the method can be applied to time-lapse problems. This is followed by the inversion of a two-dimensional model making use of common midpoint techniques.

6.1 An application in time-lapse seismic imaging

In this section we give an example of how the causality-based imaging method can be applied to time-lapse seismic imaging. We also show that for this method there are no constraints on the repeatability of the wavelet. We finish the chapter with an example of how the causality-based imaging method can be applied to 4D problems by subtracting the inversion results.

The causality-based imaging method is applied to a difference term representing the time-lapse changes in a reservoir. Fokkema, Dillen and Wapenaar [16] have presented the idea to apply the reciprocity theorem to the two different measurement states in 4D seismics. We make use of a method based on this idea derived by Dillen [14] and Wapenaar, Dillen and Fokkema [36]. This method applies the reciprocity theorems for the one-way wave equations as derived by Wapenaar and Grimbergen [37]. These reciprocity theorems relate the up- and downgoing wavefields in two different acoustic states. In time-lapse seismics it is common to make use of the difference section between two seismic sections measured at different moments in time. This difference section contains information on the change in the subsurface that arose during the time interval between measurements. The amplitudes in the difference section are however disturbed as a result of traveltime shifts due to the velocity changes in the subsurface. Therefore, the amplitudes in the difference section are not a good representation of the quantitative velocity change in the subsurface.

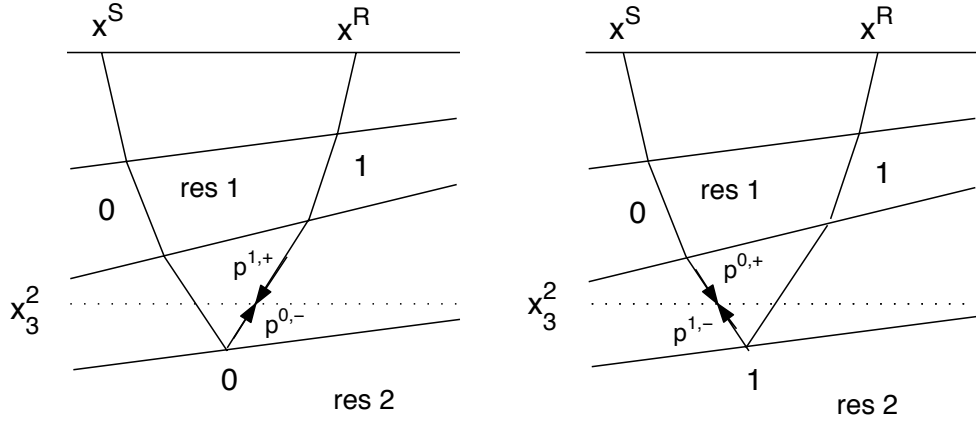


Figure 6.1: The up-and downgoing wavefields in the interaction integral.

Dillen [14] derived an interaction integral between the wavefields in the two different measurement states at an arbitrary reference level in the subsurface. He showed that in this interaction integral the amplitude disturbances mentioned earlier do not occur. The interaction integral derived by Wapenaar, Dillen and Fokkema [36] has the same properties but now allows an interpretation in terms of downgoing and upgoing wavefields. The interaction integral has the following form:

$$\int_{x_3=x_3^2} \{\hat{p}^{0,-}(\mathbf{x}|\mathbf{x}^S)\hat{p}^{1,+}(\mathbf{x}|\mathbf{x}^R) - \hat{p}^{0,+}(\mathbf{x}|\mathbf{x}^S)\hat{p}^{1,-}(\mathbf{x}|\mathbf{x}^R)\}dA, \quad (6.1)$$

where $\hat{p}^{0,-}$ represents the upgoing wavefield (travelling in the negative depth direction) in state 0, $\hat{p}^{1,+}$ represents the downgoing wavefield in state 1 etc., and x_3^2 is the reference level. State 0 is the measurement state before changes occurred (the reference state), state 1 is the state after the changes in the subsurface have occurred (the monitor state). The wavefields in the integral are visualized in Figure 6.1.

The first reservoir in which time-lapse changes take place is denoted by 'res 1' and the second reservoir in which changes take place is denoted by 'res 2'. The left part of the integral, $\int_{x_3=x_3^2} \hat{p}^{0,-}(\mathbf{x}|\mathbf{x}^S)\hat{p}^{1,+}(\mathbf{x}|\mathbf{x}^R)dA$, represents a virtual experiment where the wavefield travels down through state 0 and then travels back to the surface through the medium in

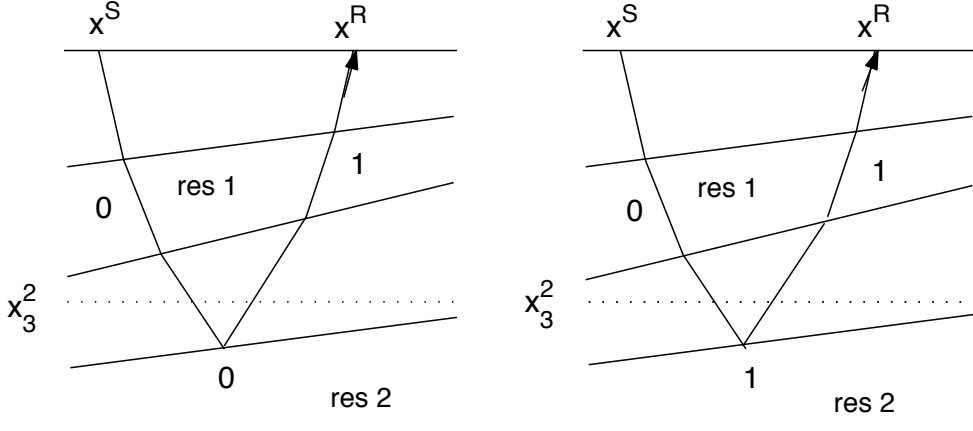


Figure 6.2: Virtual experiments, corresponding to Figure 6.1.

state 1. A similar interpretation can be given for the right part of the integral, $\int_{x_3=x_3^2} \hat{p}^{0,+}(\mathbf{x}|\mathbf{x}^S) \hat{p}^{1,-}(\mathbf{x}|\mathbf{x}^R) \{dA\}$. In this case, the reflection at the second reservoir takes place in state 1. This interpretation is visualized in Figure 6.2. The traveltimes in both virtual experiments are the same, so the amplitudes in the difference term are not disturbed and are representative for the quantitative velocity change in the second reservoir. We will determine this velocity change using the result of the interaction integral in the layer-stripping procedure. To this end we will consider the interaction integral as the reflected wavefield in the layer-stripping procedure. For the downgoing wavefield we will use the wavefield initiated in the same medium as are the wavefields in the interaction integral, but now travelling through a homogeneous background medium with the velocity of the second reservoir in state 0.

Figure 6.3 shows the velocity model we used for synthetic modelling of the wavefields. We modelled a plane wave using a finite difference method and analyzed the interaction integral for the one-dimensional case, in which the interaction integral reduces to an interaction term at x_3^2 :

$$\hat{p}^{0,-}(x_3^2|\mathbf{x}^S) \hat{p}^{1,+}(x_3^2|\mathbf{x}^R) - \hat{p}^{0,+}(x_3^2|\mathbf{x}^S) \hat{p}^{1,-}(x_3^2|\mathbf{x}^R) \quad (6.2)$$

Figure 6.4 shows the modelled downgoing wavefield in state 1, the modelled upgoing wavefield in state 0, the result of the convolution of these two and the interaction

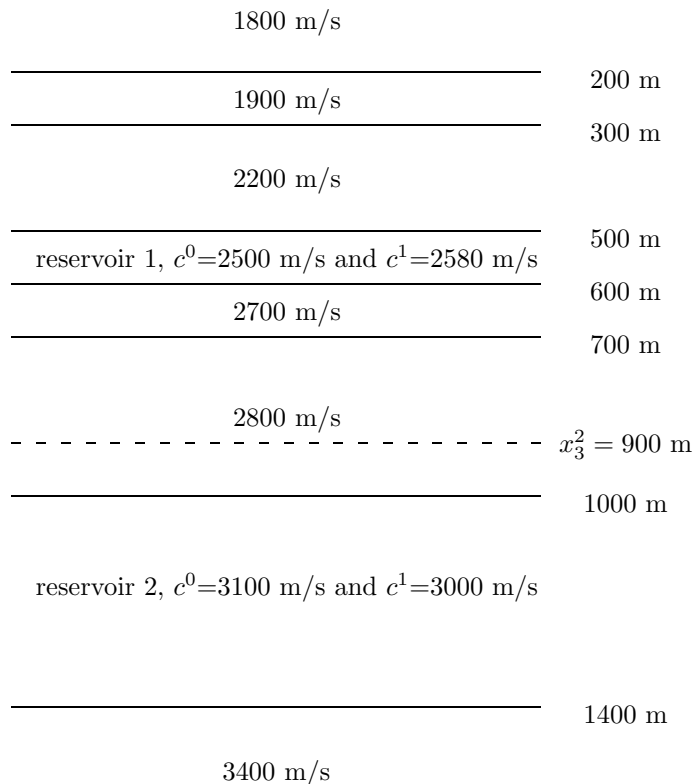


Figure 6.3: The subsurface model, with two reservoirs in which time-lapse changes take place. In the first reservoir $c^0=2500$ m/s and $c^1=2580$ m/s and in the second reservoir $c^0=3100$ m/s and $c^1=3000$ m/s. The interaction term is determined at $x_3^2=900$ m.

term in the time domain. The event at about 1 s is used as reflected wavefield in the causality-based layer-stripping method and the imaging result is shown beneath the time traces. The velocity difference from 3100 m/s to 3000 m/s is imaged accurately. Note that we invert a virtual experiment were the upper half-space has a background velocity of 3100 m/s and we perform the layer-stripping using this background velocity. Since the real upper half-space has different wave speeds, the depth at which the contrast is imaged is an apparent depth which is not the same as the true depth of the reservoir. The wavelet in this virtual experiment was computed by performing an auto-convolution of the original wavelet. The event at approximately 1.3 s has a disturbed amplitude due to the traveltime difference from the second reservoir. In a subsequent step, the reference level could be lowered to a new level below the second reservoir. Note that the wavelet we used for modelling the wavefields is a Ricker wavelet. Due to the limited bandwidth of this wavelet we analyzed the absolute value of the data. This method is explained in Chapter 5.

In time-lapse seismic surveys the repeatability of the measurements separated by the time-lapse is very important for the correct evaluation of the difference section. The repeatability concerns the exact location of source and receiver but also the wavelet. It is difficult to reproduce the exact same wavelet in two different surveys. The method we introduced in this section is not influenced by the repeatability of the wavelet. Figure 6.5 shows the imaging result for the same subsurface models as in the previous example but now two different wavelets were used. It is clear that the difference between the wavelets hardly influences the imaging result. Since the difference term we image contains a convolution of both wavelets it is not necessary for these wavelets to be the same.

Another approach to time-lapse inversion, as apposed to inverting a difference section, is to invert the reference state and the monitor state separately and then subtracting the inversion results. This approach is for instance described by Abubakar *et al.* [1] for the contrast source inversion method. An advantage of this approach is that the method is much less dependant on the repeatability of the measurements than when the difference between the seismic measurements is inverted. The source and receiver configurations of the measurements may be different for instance. A disadvantage of the method is that the inversion scheme has to be run twice, for both states, and therefore requires more computation time. Imaging results for this approach are shown in Figure 6.6. We used the same velocity model as for the previous example, shown in Figure 6.3. The top picture of Figure 6.6 shows the difference between the two separate velocity models. The middle picture shows the difference between the two imaging results obtained by inverting the synthetic data for the monitor state and the reference state separately. For both inversions the same

Gaussian wavelet was used. The bottom picture shown the difference between the two imaging results when for modelling the reference state a different wavelet was used then for the monitor state. For the reference state we now used the derivative of a Gaussian while for the monitor state we used a Ricker wavelet. The absolute value of the wavefields was used. The difference result for the different wavelets shows some small deviations that are not visible when similar wavelets were used. This is a result of the fact that the resolution of the imaging result is strongly influenced by the frequency content of the wavelet. The frequency spectra of the two

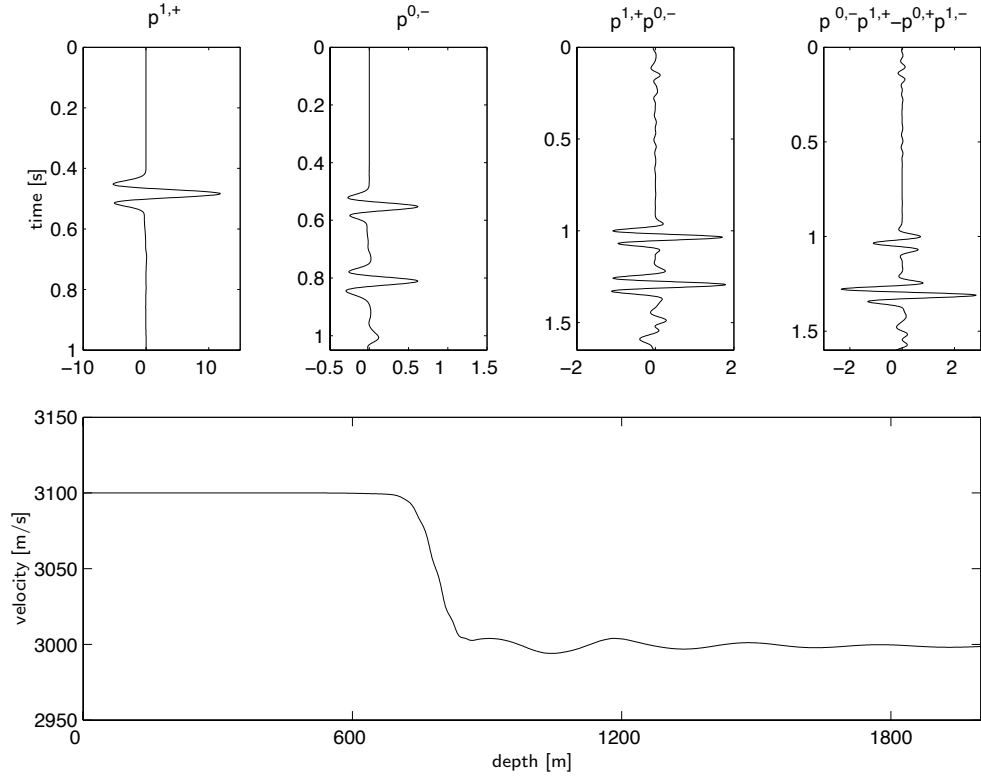


Figure 6.4: Top, from left to right: $p^{1,+}(x_3^2|x^R), p^{0,-}(x_3^2|x^S), \hat{p}^{0,-}(x_3^2|x^S)\hat{p}^{1,+}(x_3^2|x^R)$, transformed back to the time domain, and $\hat{p}^{0,-}(x_3^2|x^S)\hat{p}^{1,+}(x_3^2|x^R) - \hat{p}^{0,+}(x_3^2|x^S)\hat{p}^{1,-}(x_3^2|x^R)$, transformed back to the time domain. Below that the imaging result of the interaction integral. The modelled velocity in the second reservoir varies from 3100 m/s to 3000 m/s.

wavelets used for this example are shown in the top pictures (left and middle) in Figure 6.7. The frequency content is almost the same. If this frequency content is not the same, differences will be visible around the interfaces in the velocity model. This is visible in the bottom picture of Figure 6.7. A Ricker wavelet, similar to the one in the previous example, is used for the monitor state, and a derivative of a Gaussian wavelet is used for the reference state. The frequency content is now lower than for the previous example. This is shown in the top right picture of Figure 6.7 (reference state 2). The difference result now shows many deviations from the actual difference, as shown in the top picture of Figure 6.6.

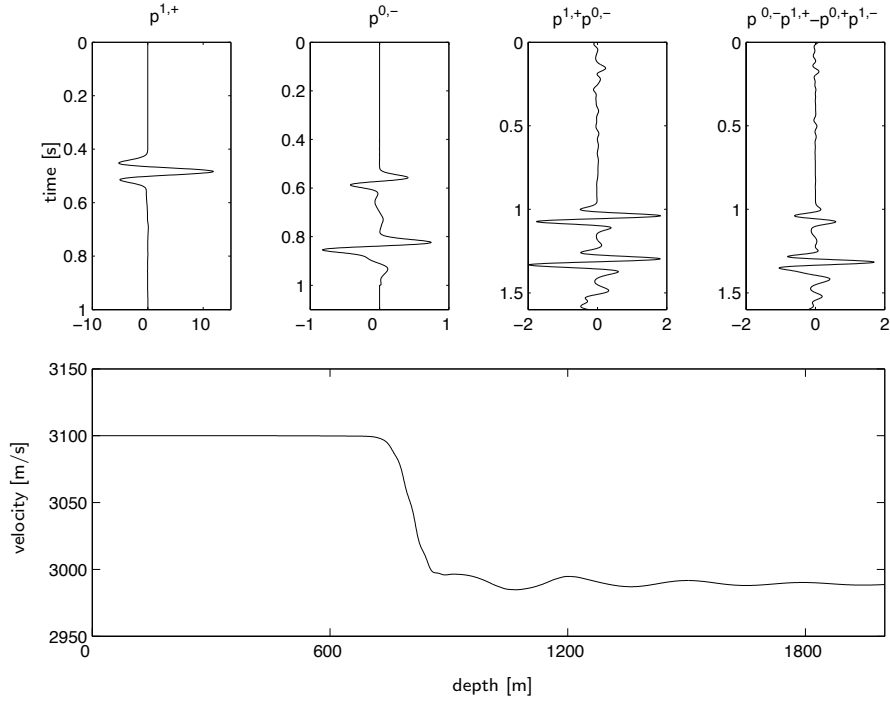


Figure 6.5: Top, from left to right: $p^{1,+}(x_3^2|x^R), p^{0,-}(x_3^2|x^S), \hat{p}^{0,-}(x_3^2|x^S)\hat{p}^{1,+}(x_3^2|x^R)$, transformed back to the time domain, and $\hat{p}^{0,-}(x_3^2|x^S)\hat{p}^{1,+}(x_3^2|x^R) - \hat{p}^{0,+}(x_3^2|x^S)\hat{p}^{1,-}(x_3^2|x^R)$, transformed back to the time domain. Note that two different wavelets were used. Below that the imaging result of the interaction integral.

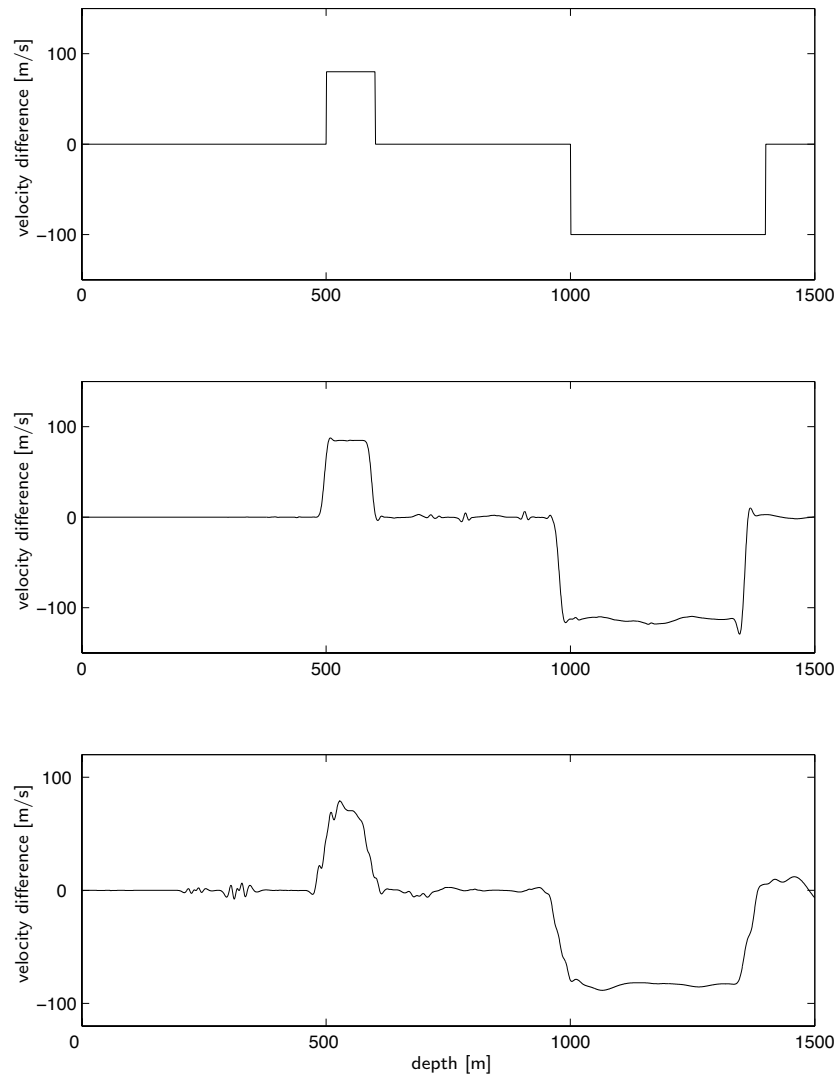


Figure 6.6: Top: difference between velocity models for monitor state and reference state. Middle: Difference between imaging results obtained by inverting the monitor state and the reference state separately. Both states were modelled with the same wavelet. Bottom: Difference section between imaging results, now the separate states were modelled with a different wavelet. The frequency spectra of these wavelets are shown in Figure 6.7

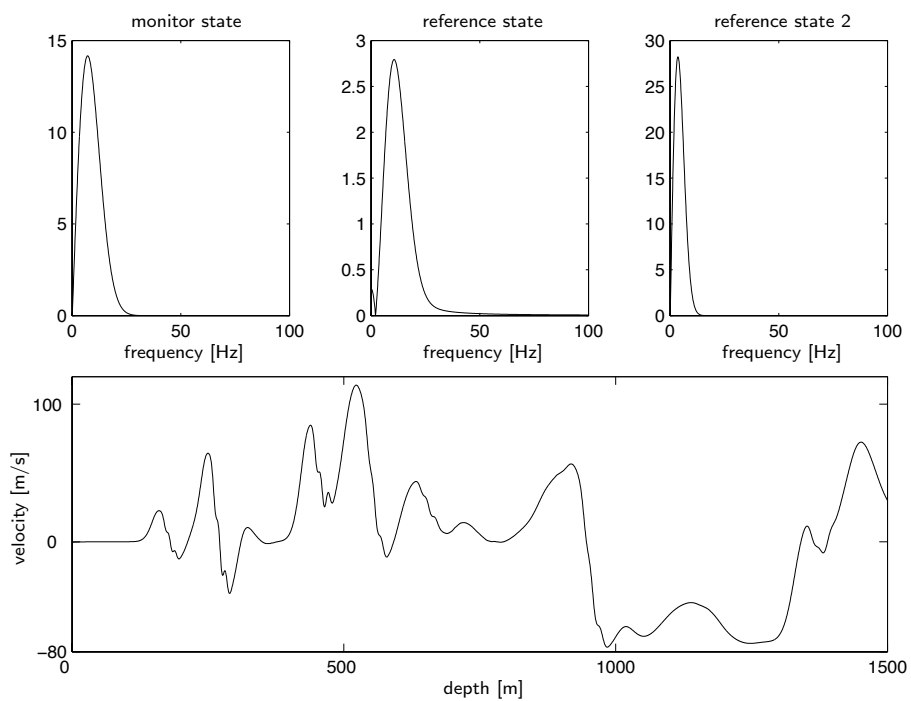


Figure 6.7: The frequency spectra for the different states. Top left and top middle are the frequency spectra of the wavelets used for the monitor and reference state leading to the bottom difference result in Figure 6.6. The spectra top left and top right are the frequency spectra of the wavelets used for the monitor and reference state leading to the difference result shown on the bottom.

6.2 An example for a two-dimensional medium

So far, we have examined the behavior and characteristics of the method for the one-dimensional case. In this section we use common midpoint gathers to invert a 2D example, as a first step towards extension of the method to the more-dimensional problem.

The velocity model is shown in the top picture of Figure 6.9. The model has one interface with variable depth, the velocity varies from 1500 m/s to 2500 m/s. The model is 2500 m wide and 1050 m deep. Using a 2D finite-difference code we modelled 126 shots with 126 receivers at the surface, each 20 meters apart. We used a Ricker wavelet as input wavelet. This is a bandlimited wavelet not containing the lowest frequencies. The problems arising when these frequencies are missing together with a solution method are described in Chapter 5. For the examples in this section we used the absolute value method described in section 5.3. The synthetic upgoing wavefield for shot position at 1200m is shown in the top picture of Figure 6.10. In the presence of dip it is more profitable to deal with common midpoint gathers than with shot gathers. A comprehensive review of the use of common midpoint data is given by Diebold and Stoffa [13]. The synthetic data were therefore sorted to CMP-gathers, the gather for common midpoint position 1200 m is shown in the middle picture of Figure 6.10. Every 20th CMP-gather was then transformed to the intercept time and ray parameter (τ -p) domain. An overview of τ -p mapping of seismic data is given by Stoffa *et al.* [30]. The CMP-gather in the τ -p domain for common midpoint position 1200m is shown in the bottom picture of Figure 6.10. Since the trace for $p=0$ s/m after transformation to the τ -p domain corresponds to normal incidence we can apply our imaging procedure to this trace. The processing sequence for this procedure is depicted in Figure 6.8. Decomposition of the total wavefield into an upgoing and a downgoing part was performed by modelling both the heterogeneous and a homogeneous subsurface and subtracting the two data sets. The step where the absolute value of the wavefields is used is necessary due to the limited bandwidth of the data and is explained in Chapter 5. The imaging result for several CMP-positions is shown in the middle picture of Figure 6.9. The imaging result gives stable and accurate results for the left part of the model, which is horizontally layered. The result starts to show deviations when the reflector in the velocity model starts to dip. Furthermore the dip at the right side of the model is too steep to be modelled correctly. This method, where we use plane-wave decomposition of CMP-gathers is known to be applicable only to media varying smoothly in the horizontal direction. The reason for this limitation is that by using only the data for $p = 0$ s/m, we do not make use of a huge part of the information in the

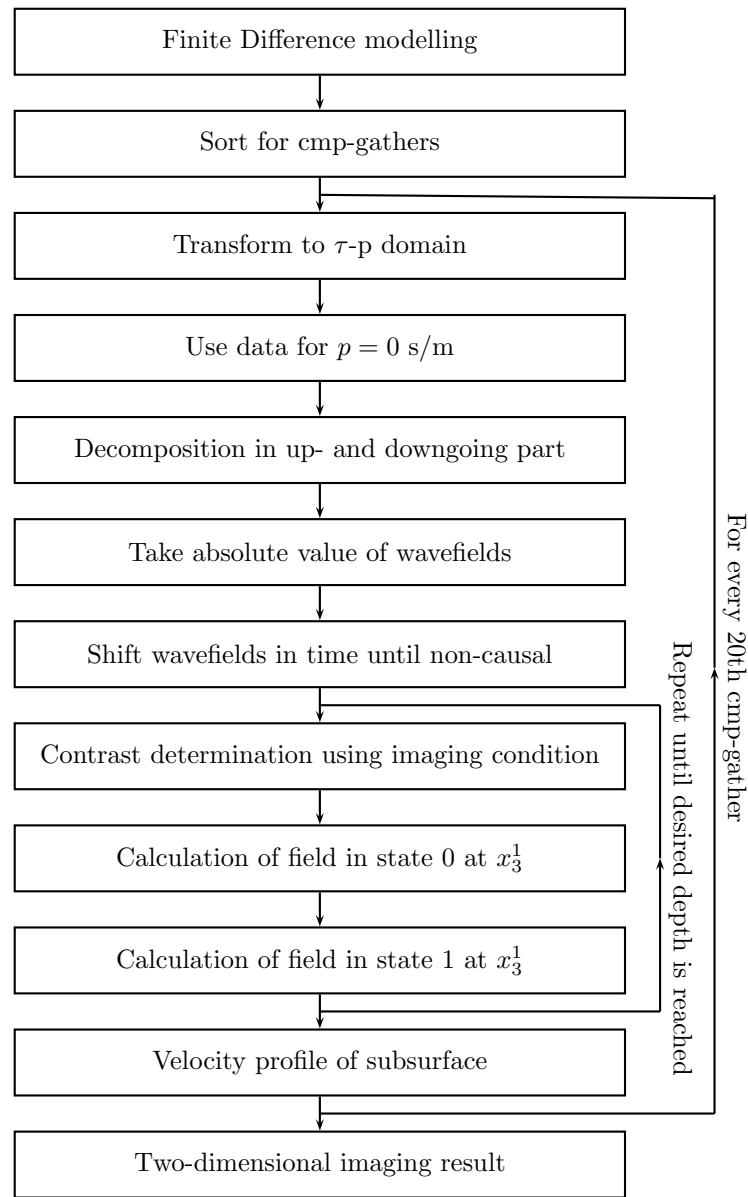


Figure 6.8: Flow diagram of layer-stripping algorithm using *cmp-gathers*.

data. This will of course have consequences for the accuracy of the inversion result. When the theory as described in Chapter 2 will be implemented, this restriction on variations in the horizontal direction will not have to be made. We will then make use of all values for the angular slowness α of the pressure wavefields in the double spatial Fourier domain.

The imaging result for a slightly more complicated velocity model is given in Figure 6.11. The imaging result still closely resembles the velocity model. The artifacts caused by the τ - p transform were manually removed before applying the layer-stripping. Stoffa *et al.* [30] describe how this removal can be performed using a semblance derived window function.

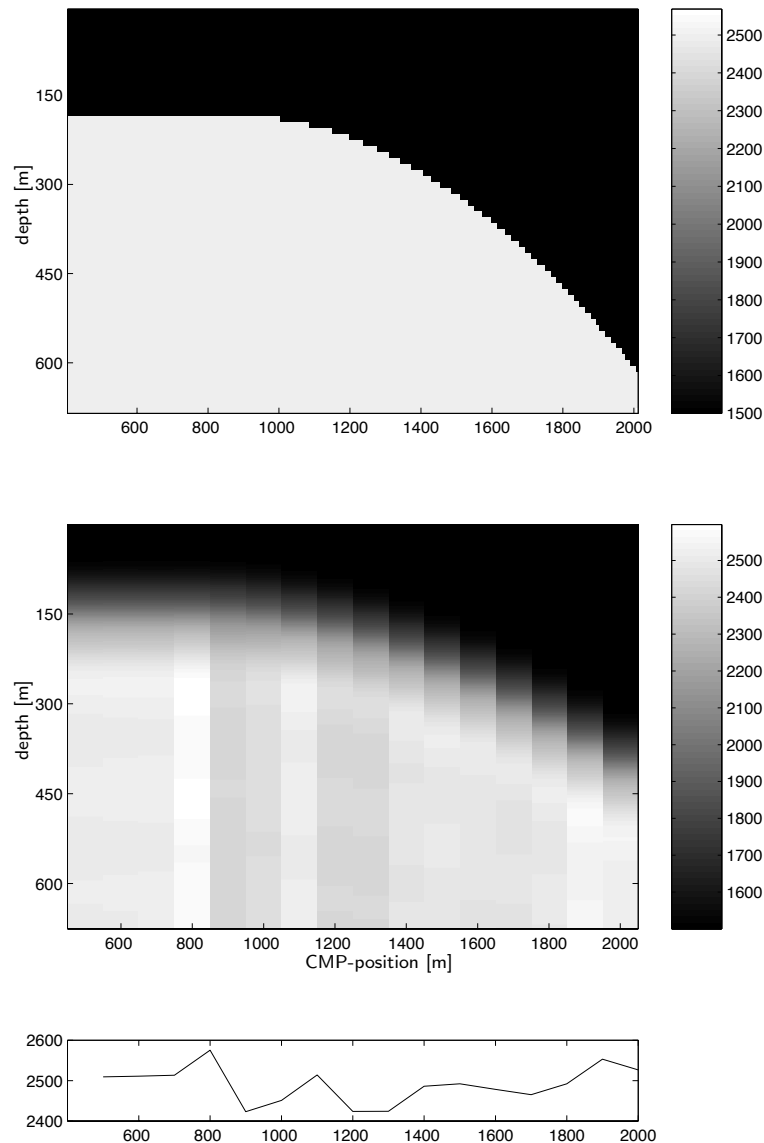


Figure 6.9: 2D velocity model (top) together with imaging result per CMP-position (middle). The bottom picture shows the value of the imaging result at 450 m depth. The model velocity at this position is 2500 m/s.

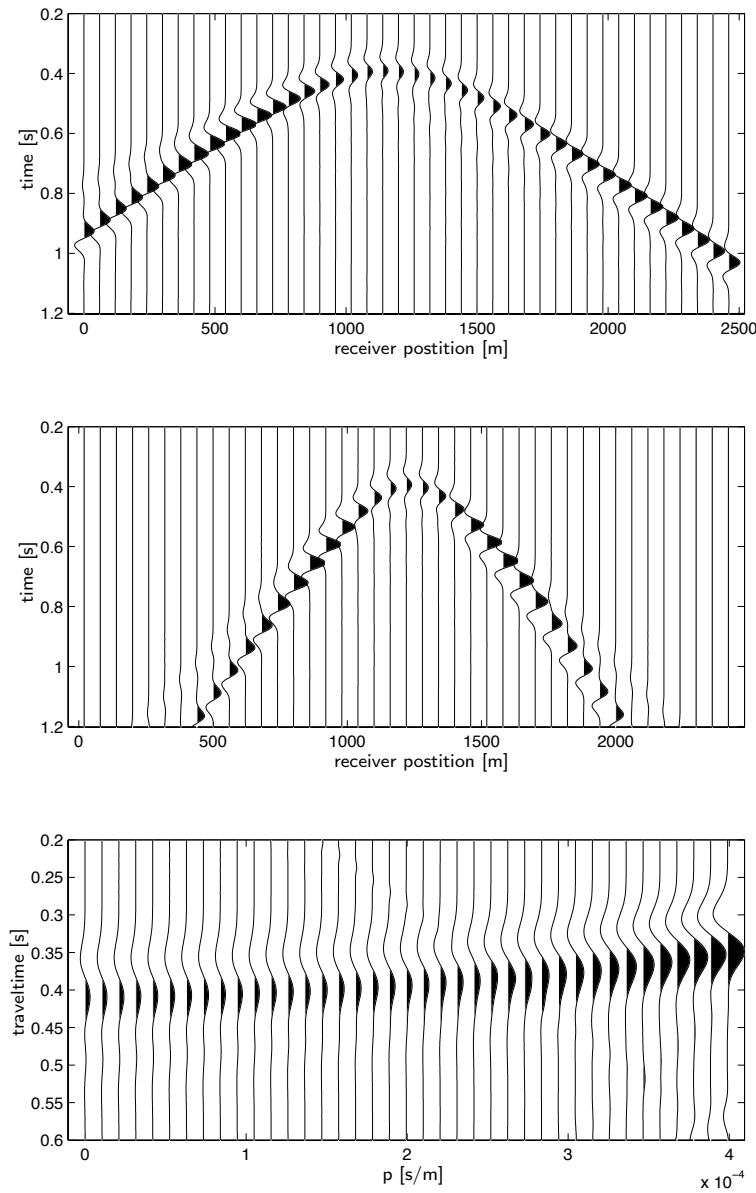


Figure 6.10: Synthetic upgoing wavefield, for shot position at 1200 m (top), for CMP-position 1200 m (middle) and the τ - p transform (bottom) for this CMP-position.

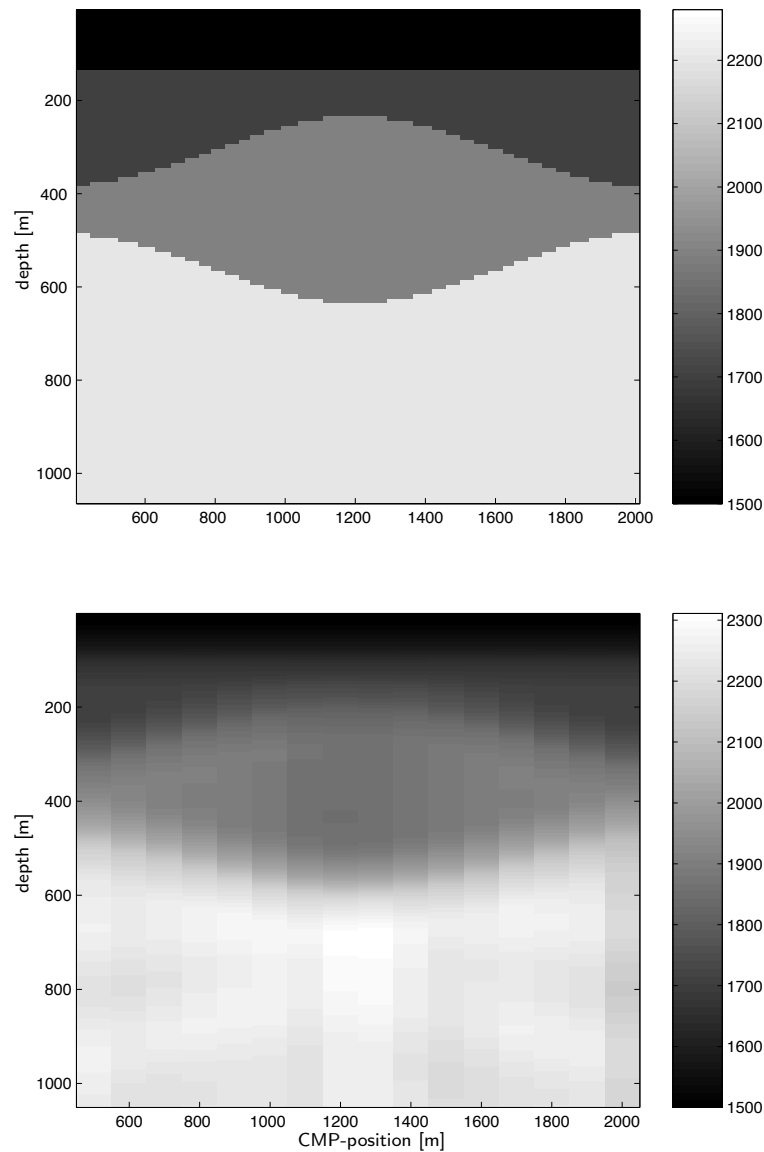


Figure 6.11: Imaging result (bottom) per CMP-position for more complicated velocity model (top).

Conclusions

In this thesis we have introduced a layer-stripping method based on the reciprocity theorem and the causality principle. The surplus value of this method is that the theory is applicable to laterally varying media and that no a priori velocity information is required. Even though there are many different seismic imaging and inversion methods, a direct nonlinear method determining the subsurface properties directly from the data, for any subsurface configuration, still remained to be developed. The method described in this thesis is a step towards the development of such a method.

The first chapters of this thesis focused on the theory behind the method. We have shown that the velocity contrast over an interface between a homogeneous and a laterally varying medium can be expressed in terms of the up- and downgoing pressure wavefields in the homogeneous medium above this interface. We have called this expression the imaging condition. The causality principle plays a key role since the derivation is based on the assumption that the wavefield below the interface consists of just downgoing waves. Due to causality we know that there will always be a (short) interval in time for which this assumption is true. We have shown that the imaging condition can be combined with a velocity replacement method based on reciprocity in order to determine the properties of the subsurface. The wavefield for the case where a thin laterally varying top layer is replaced by a layer with the properties of a homogeneous background medium can be expressed in terms of the wavefields before replacement of this layer. We have shown that it is theoretically possible by repetitive layer replacement in combination with the imaging condition to determine the velocity profile of a laterally varying, three-dimensional subsurface. Implementation of the theory involves large matrix calculations and solving pseudo-differential equations. The only assumptions on the subsurface we made are that the wave propagation is adequately described by the acoustic wave equation and that the density in the subsurface is a constant. In Chapter 3 we have shown that the three-dimensional case can be simplified for the general two-dimensional case, followed by the case for 2D wave propagation in a horizontally layered medium and the one-dimensional case.

We have investigated the properties of the method in the last chapters of the thesis, beginning with the one-dimensional case and using synthetically generated data. By starting with the one-dimensional case we have been able to closely evaluate and understand the different characteristics of the method. It can be concluded that a one-dimensional subsurface model can be very accurately inverted when the energy of the wavefields are considered in the imaging condition. We have shown that the internal multiples in the data are handled correctly, which was to be expected for a non-linear solution method. The choice for the thickness of the stripped layers is connected to the time sampling of the data and the velocity of the homogeneous background medium. The resolution of the method depends on the bandwidth of the data. Since the method is entirely data driven, only information contained in the data can be recovered. Accurate results can be obtained for obliquely incident plane waves on a one-dimensional medium, however the method does not hold for post-critical incidence. For high angles of incidence and high velocities the method breaks down for precritical incidence as well. This is a result of noise being generated during the layer-stripping procedure.

By comparing the layer-stripping method to another layer-stripping method based on the Schur algorithm we have shown that more accurate results are obtained using the causality-based imaging method, especially in the presence of noise. The use of the energy of the wavefields in the imaging condition has a stabilizing effect on the imaging result which is not available for the Schur method. Another big difference between the methods is the fact that the Schur algorithm is applicable to laterally invariant media only.

The limited bandwidth of seismic data is a problem for seismic inversion which should not be underestimated. In Chapter 5 we have shown that in order to reconstruct a velocity profile, the spectral information of which contains small wavenumber components, the presence of all low frequencies in the data is required. This frequency content is however not realistic for seismic data. This problem is usually dealt with by adding a priori velocity information. We have proposed an alternative solution method using the absolute value or the envelope of the data which gives good results as long as the events in the data are not overlapping. The loss of the sign of the data due to taking the absolute value or the envelope can be dealt with by constructing a sign-file using median filters. As a result of the adaptation of the data the imaging result becomes less accurate than for the case a wavelet containing all low frequencies is used.

We have shown that the method can be applied to time-lapse seismic imaging. The

method can be used to determine the changes in a reservoir by inverting a difference term over the reservoir. The method we propose does not require the wavelets of the two different measurements to be equal. In the final section of the chapter we have shown that good imaging results can be obtained for two-dimensional subsurface models using common midpoint gathers. This technique is applicable only to media varying smoothly in the horizontal direction. The imaging result for the two-dimensional case shows the potential of the method for these kind of problems. By fully implementing our layer-stripping method for the multi-dimensional case we expect to find more accurate imaging results for laterally varying media.

As an overall conclusion we can state that promising results have been obtained by designing and partly implementing a completely data driven inversion method which is theoretically applicable to laterally varying media.

In order to be able to apply the method to real data some steps have to be made. The first step is the implementation of the multi-dimensional case. As stated before, this requires large matrix calculations in the layer replacement and solving pseudo-differential equations in the imaging condition. The work by van Borselen [35] can be a guideline for implementing the layer replacement. The second step is to find a way to deal with the noisy character of real data. It was shown in section 4.2 that our layer-stripping method is relatively stable in the presence of noise. The bandlimited nature of the seismic data might however lead to complications. When we work with the absolute value or envelope of the data the noise will receive a positive sign and will therefore have a large influence on the energy of the wavefields in the evaluation of the imaging condition. To be able to apply the absolute value or envelope method to real data the negative signs of the noise in the data have to be recovered, for example by median filtering the noisy data with a different window size. Please note that no matter how stable the method, it still is completely data driven, which means that when there are mistakes in the data these mistakes will show up in the imaging result and influence the rest of the imaging result. Some other practical considerations are the fact that knowledge of the source wavelet is required and that the velocity of the top layer (the velocity of the homogeneous background medium) has to be known. Taking into account that by measuring both the pressure and the velocity wavefield the wavelet can be determined, and the fact that the top layer in seismic surveys is often sea water, these restrictions do not seem insurmountable. Loosening the constraint on the density of the subsurface and extension of the method to the elastic case can be a subject of further research. Both adjustments of the method will lead to more complicated formulations and calculations.

The result in section 6.1 gives examples of the application of the method to time-lapse seismics. The strength and surplus value of the causality-based imaging method for industry might well be its potential to be used for accurately imaging parts of the subsurface which need focussing on. We have shown that this is for instance possible for time-lapse problems by imaging only the difference term representing the changes that occurred in a reservoir over time. Our method can be combined with any other method which can be used to determine the wavefields at a certain depth in the subsurface. Also note that in this thesis we have combined a layer replacement method based on the reciprocity theorem with the causality-based imaging condition. This combination is not obligatory and one can think of applications involving only one of the two separate methods, such as for example an optimization method using an a priori background model and the velocity replacement method or a method combining the causality-based imaging method with a different way of extrapolating the wavefields.

A

Proof of symmetry of pseudo-differential operator

In the derivation of the imaging condition for laterally varying media, as described in section (2.3.1), Eq. (2.64), the property that the operator $\sqrt{(\Gamma_0^R)^2 - \mathcal{K}}$ is a symmetric operator is used. Note that this operator is a pseudo-differential operator in the spatial Fourier domain. In this section the proof of symmetry of this pseudo-differential operator is given. We start with the expression for the wave-equation for pressure in the (\mathbf{x}_T, s) -domain:

$$(\nabla^2 - \frac{s^2}{c_1^2(\mathbf{x}_T)})\hat{p}(\mathbf{x}_T) = 0. \quad (\text{A.1})$$

Using this we can write (Helmholtz equation):

$$\partial_3^2 \hat{p}(\mathbf{x}_T) = \left(\frac{s^2}{c_1^2(\mathbf{x}_T)} - \partial_\gamma \partial_\gamma \right) \hat{p}(\mathbf{x}_T) = \mathcal{H}_2 \hat{p}(\mathbf{x}_T), \quad (\text{A.2})$$

where operator $\mathcal{H}_2 = s^2 \left(\frac{1}{c_1^2(\mathbf{x}_T)} - \frac{1}{s^2} \partial_\gamma \partial_\gamma \right)$, and $\gamma = \{1, 2\}$. Now we rewrite this as follows:

$$\mathcal{H}_2 = \mathcal{H}_{2,0} - s^2 K(\mathbf{x}_T), \quad (\text{A.3})$$

where

$$\mathcal{H}_{2,0} = s^2 \left(\frac{1}{c_0^2} - \frac{1}{s^2} \partial_\gamma \partial_\gamma \right). \quad (\text{A.4})$$

Now write:

$$\mathcal{H}_2(\mathbf{x}_T) \hat{p}(\mathbf{x}_T) = \int_{\mathbf{x}'_T \in \mathbb{R}^2} H_2(\mathbf{x}_T, \mathbf{x}'_T) \hat{p}(\mathbf{x}'_T) dA, \quad (\text{A.5})$$

where $H_2(\mathbf{x}_T, \mathbf{x}'_T)$ is called the kernel of operator \mathcal{H}_2 . It expresses the action of the operator on wavefield $\hat{p}(\mathbf{x}'_T)$ in a generalized convolution integral. Consequently, it can be written as:

$$H_2(\mathbf{x}_T, \mathbf{x}'_T) = \mathcal{H}_2(\mathbf{x}_T) \delta(\mathbf{x}_T - \mathbf{x}'_T). \quad (\text{A.6})$$

When we consider a medium with only one interface, there is only a downgoing field beneath the interface. In this case we can write:

$$\partial_3 \hat{p}(\mathbf{x}_T) = -\mathcal{H}_1 \hat{p}(\mathbf{x}_T), \quad (\text{A.7})$$

where:

$$\begin{aligned} \mathcal{H}_1 &= \sqrt{\mathcal{H}_2} \\ &= s \sqrt{\frac{1}{c_1^2(\mathbf{x}_T)} - \frac{1}{s^2} \partial_q \partial_q} \end{aligned} \quad (\text{A.8})$$

$$= s \sqrt{\frac{1}{s^2} \mathcal{H}_{2,0} - K(\mathbf{x}_T)}. \quad (\text{A.9})$$

The operator \mathcal{H}_2 is a partial differential operator. We call the square-root operator \mathcal{H}_1 a pseudo-differential operator since it contains implicitly (via \mathcal{H}_2) the lateral differentiation operators but it also contains a non-polynomial operation. Analogously to Eq. (A.5) we can write:

$$\mathcal{H}_1(\mathbf{x}_T) \hat{p}(\mathbf{x}_T) = \int_{\mathbf{x}'_T \in \mathbb{R}^2} H_1(\mathbf{x}_T, \mathbf{x}'_T) \hat{p}(\mathbf{x}'_T) dA, \quad (\text{A.10})$$

with

$$H_1(\mathbf{x}_T, \mathbf{x}'_T) = \mathcal{H}_1(\mathbf{x}_T) \delta(\mathbf{x}_T - \mathbf{x}'_T). \quad (\text{A.11})$$

Now we will focus on the symmetry behavior of the operators. The bilinear form is defined as:

$$\langle f, g \rangle_b = \int_{\mathbf{x}_T \in \mathbb{R}^2} f(\mathbf{x}_T) g(\mathbf{x}_T) dA. \quad (\text{A.12})$$

We introduce an operator \mathcal{A} and its transposed operator \mathcal{A}^t for which the following is valid:

$$\langle \mathcal{A}f, g \rangle_b = \langle f, \mathcal{A}^t g \rangle_b. \quad (\text{A.13})$$

The operator \mathcal{A} is symmetric when the transpose of \mathcal{A} equals \mathcal{A} itself:

$$\begin{aligned} \mathcal{A}^t &= \mathcal{A} \\ \Leftrightarrow \mathcal{A}(\mathbf{x}_T, \mathbf{x}'_T) &= \mathcal{A}(\mathbf{x}'_T, \mathbf{x}_T). \end{aligned} \quad (\text{A.14})$$

So for \mathcal{H}_2 and \mathcal{H}_1 to be symmetric the following conditions have to be satisfied:

$$\mathcal{H}_2^t = \mathcal{H}_2 \Leftrightarrow H_2(\mathbf{x}_T, \mathbf{x}'_T) = H_2(\mathbf{x}'_T, \mathbf{x}_T), \quad (\text{A.15})$$

$$\mathcal{H}_1^t = \mathcal{H}_1 \Leftrightarrow H_1(\mathbf{x}_T, \mathbf{x}'_T) = H_1(\mathbf{x}'_T, \mathbf{x}_T), \quad (\text{A.16})$$

Wapenaar has shown in [37] that this is the case for both operators in the \mathbf{x}_T domain. Now we have to show the same for the spatial Fourier domain. In order to do this, we write:

$$\begin{aligned}\mathcal{F}_x(\mathcal{H}_2 \hat{p}(\mathbf{x}_T)) &= \mathcal{F}_x[(\mathcal{H}_{2,0} - s^2 K(\mathbf{x}_T)) \hat{p}(\mathbf{x}_T)] \\ &= s^2(\Gamma_0^2 - \mathcal{K}(js\alpha_T)) \bar{P}(js\alpha_T).\end{aligned}\quad (\text{A.17})$$

The operator \mathcal{F}_x performs the spatial Fourier transform. Using Eq. (A.5) we can write:

$$\begin{aligned}\mathcal{F}(\mathcal{H}_2 \hat{p}(\mathbf{x}_T)) &= \mathcal{F}\left[\int_{\mathbf{x}'_T \in \mathbb{R}^2} H_2(\mathbf{x}_T, \mathbf{x}'_T) \hat{p}(\mathbf{x}'_T) dA\right] \\ &= \int_{\mathbf{x}_T \in \mathbb{R}^2} \exp(j s \alpha_T \cdot \mathbf{x}_T) \int_{\mathbf{x}'_T \in \mathbb{R}^2} H_2(\mathbf{x}_T, \mathbf{x}'_T) \hat{p}(\mathbf{x}'_T) dAdA \\ &= \left(\frac{1}{2\pi}\right)^2 \int_{\mathbf{x}_T \in \mathbb{R}^2} \int_{\mathbf{x}'_T \in \mathbb{R}^2} \int_{s\alpha'_T \in \mathbb{R}^2} \exp(j s \alpha_T \cdot \mathbf{x}_T - j s \alpha'_T \cdot \mathbf{x}'_T) \\ &\quad \times H_2(\mathbf{x}_T, \mathbf{x}'_T) \bar{P}(js\alpha'_T) dAdAdA \\ &= \left(\frac{1}{2\pi}\right)^2 \int_{s\alpha'_T \in \mathbb{R}^2} \bar{H}_2(js\alpha_T, -js\alpha'_T) \bar{P}(js\alpha'_T) dA,\end{aligned}\quad (\text{A.18})$$

where

$$\begin{aligned}\bar{H}_2(js\alpha_T, js\alpha'_T) &= \\ &\int_{\mathbf{x}_T \in \mathbb{R}^2} \int_{\mathbf{x}'_T \in \mathbb{R}^2} H_2(\mathbf{x}_T, \mathbf{x}'_T) \exp(j s \alpha_T \cdot \mathbf{x}_T) \exp(j s \alpha'_T \cdot \mathbf{x}'_T) dAdA.\end{aligned}\quad (\text{A.19})$$

From this it can be concluded that:

$$H_2(\mathbf{x}_T, \mathbf{x}'_T) = H_2(\mathbf{x}'_T, \mathbf{x}_T) \Leftrightarrow \bar{H}_2(js\alpha_T, js\alpha'_T) = \bar{H}_2(js\alpha'_T, js\alpha_T).$$

Now use Eq. (A.18) to write:

$$\begin{aligned}\mathcal{F}(\mathcal{H}_2 \hat{p}(\mathbf{x}_T)) &= \bar{H}_2(js\alpha_T) \bar{P}(js\alpha_T) \\ &= s^2(\Gamma_0^2 - \mathcal{K}(js\alpha_T)) \bar{P}(js\alpha_T) \\ &= \left(\frac{1}{2\pi}\right)^2 \int_{s\alpha'_T \in \mathbb{R}^2} \bar{H}_2(js\alpha_T, -js\alpha'_T) \bar{P}(js\alpha'_T) dA.\end{aligned}\quad (\text{A.20})$$

Similarly, we can write:

$$\begin{aligned}
\mathcal{F}(\mathcal{H}_1 \hat{p}(\mathbf{x}_T)) &= \bar{\mathcal{H}}_1(j s \boldsymbol{\alpha}_T) \bar{p}(j s \boldsymbol{\alpha}_T) \\
&= s \sqrt{\Gamma_0^2 - \mathcal{K}(j s \boldsymbol{\alpha}_T)} \bar{p}(j s \boldsymbol{\alpha}_T) \\
&= \left(\frac{1}{2\pi}\right)^2 \int_{s \boldsymbol{\alpha}'_T \in \mathbb{R}^2} \bar{\mathcal{H}}_1(j s \boldsymbol{\alpha}_T, -j s \boldsymbol{\alpha}'_T) \bar{p}(j s \boldsymbol{\alpha}'_T) dA.
\end{aligned} \tag{A.21}$$

Since:

$$\begin{aligned}
\bar{\mathcal{H}}_1(j s \boldsymbol{\alpha}_T, j s \boldsymbol{\alpha}'_T) &= \\
&\int_{\mathbf{x}_T \in \mathbb{R}^2} \int_{\mathbf{x}'_T \in \mathbb{R}^2} H_1(\mathbf{x}_T, \mathbf{x}'_T) \exp(j s \boldsymbol{\alpha}_T \cdot \mathbf{x}_T) \exp(j s \boldsymbol{\alpha}'_T \cdot \mathbf{x}'_T) dA dA,
\end{aligned} \tag{A.22}$$

the following is valid:

$$H_1(\mathbf{x}_T, \mathbf{x}'_T) = H_1(\mathbf{x}'_T, \mathbf{x}_T) \Leftrightarrow \bar{\mathcal{H}}_1(j s \boldsymbol{\alpha}_T, j s \boldsymbol{\alpha}'_T) = \bar{\mathcal{H}}_1(j s \boldsymbol{\alpha}'_T, j s \boldsymbol{\alpha}_T). \tag{A.23}$$

The inner product is defined as:

$$\langle \bar{f}, \bar{g} \rangle = \left(\frac{1}{2\pi}\right)^2 \int_{s \boldsymbol{\alpha}_T \in \mathbb{R}^2} \bar{f}(j s \boldsymbol{\alpha}_T) \bar{g}(-j s \boldsymbol{\alpha}_T) dA. \tag{A.24}$$

Using this definition we arrive at the expression which is used in Eq. (2.64) in the derivation of the imaging condition:

$$\begin{aligned}
\langle \bar{\mathcal{H}}_1 \bar{f}, \bar{g} \rangle &= \\
&\left(\frac{1}{2\pi}\right)^4 \int_{s \boldsymbol{\alpha}_T \in \mathbb{R}^2} \int_{s \boldsymbol{\alpha}'_T \in \mathbb{R}^2} \bar{\mathcal{H}}_1(j s \boldsymbol{\alpha}_T, -j s \boldsymbol{\alpha}'_T) \bar{f}(j s \boldsymbol{\alpha}'_T) \bar{g}(-j s \boldsymbol{\alpha}_T) dA dA = \\
&\left(\frac{1}{2\pi}\right)^4 \int_{s \boldsymbol{\alpha}_T \in \mathbb{R}^2} \int_{s \boldsymbol{\alpha}'_T \in \mathbb{R}^2} \bar{f}(j s \boldsymbol{\alpha}'_T) \bar{\mathcal{H}}_1(-j s \boldsymbol{\alpha}'_T, j s \boldsymbol{\alpha}_T) \bar{g}(-j s \boldsymbol{\alpha}_T) dA dA = \\
&\left(\frac{1}{2\pi}\right)^2 \int_{s \boldsymbol{\alpha}'_T \in \mathbb{R}^2} \bar{f}(j s \boldsymbol{\alpha}'_T) \bar{\mathcal{H}}_1(-j s \boldsymbol{\alpha}'_T) \bar{g}(-j s \boldsymbol{\alpha}'_T) dA = \\
&\langle \bar{f}, \bar{\mathcal{H}}_1 \bar{g} \rangle.
\end{aligned} \tag{A.25}$$

B

Proposed solution strategy for layer replacement

The two basic equations for the three-dimensional case, Eqs (2.42) and (2.45) are:

$$\begin{aligned}
& s^2 \hat{W} \int_{x_3^0}^{x_3^1} \frac{\exp(-s\Gamma_0^R(x_3 - x_3^0))}{2s\Gamma_0^R} \mathcal{K}\{\bar{p}^0\}(js\alpha_T^R, x_3| - js\alpha_T^S, x_3^S) dx_3 \\
& + \frac{\exp(-s\Gamma_0^R \Delta x_3)}{(2\pi)^2} \int_{s\alpha_T \epsilon \mathbb{R}^2} \bar{p}^{1,r}(js\alpha_T^R, x_3^1| - js\alpha_T^S, x_3^S) dA \times \\
& s^2 \int_{x_3^0}^{x_3^1} \exp(s\Gamma_0(x_3 - x_3^S)) \mathcal{K}\{\bar{p}^0\}(js\alpha_T, x_3| - js\alpha_T^S, x_3^S) dx_3 \\
& = \hat{W}[\bar{p}^{0,r}(js\alpha_T^R, x_3^0| - js\alpha_T^S, x_3^S) \\
& \quad - \bar{p}^{1,r}(js\alpha_T^R, x_3^1| - js\alpha_T^S, x_3^S) \exp(-s\Gamma_0^R \Delta x_3)], \tag{B.1}
\end{aligned}$$

and

$$\begin{aligned}
& \bar{p}^0(js\alpha_T^R, x_3^1| - js\alpha_T^S, x_3^S) = \bar{p}^{0,r}(js\alpha_T^R, x_3^0| - js\alpha_T^S, x_3^S) \exp(s\Gamma_0^R \Delta x_3) \\
& + \bar{p}^{0,i}(js\alpha_T^R, x_3^0| - js\alpha_T^S, x_3^S) \exp(-s\Gamma_0^R \Delta x_3) \\
& + s^2 \int_{x_3^0}^{x_3^1} \frac{\sinh(s\Gamma_0^R(x_3 - x_3^1))}{s\Gamma_0^R} \mathcal{K}\{\bar{p}^0\}(js\alpha_T^R, x_3| - js\alpha_T^S, x_3^S) dx_3, \tag{B.2}
\end{aligned}$$

where $\Delta x_3 = x_3^1 - x_3^0$. Since the expression $\mathcal{K}\bar{p}$ is a convolutional operator in case of a laterally varying medium, a straightforward numerical solution of these equations (as in section 3.1.1) is not possible. The evaluation of the equations involves dealing with large matrices and will be time-consuming. In this appendix we propose a solution method to solve the basic equations numerically. We use Taylor expansions

to simplify the equations. In the first part of this solution method we follow the theory by Smit [29]. Equation (B.2) is used to determine the total pressure wavefield at depth x_3^1 , just below the top layer, from the known wavefields at depth x_3^0 . We call this equation the consistence equation. Equation (B.1) is used to determine the upgoing wavefield $p^{1,r}$ after replacement of the top layer by a homogeneous layer. In order to evaluate Eq. (B.2) we use a Taylor expansion for the total wavefield in state 0:

$$\begin{aligned} \bar{p}^0(j s \alpha_T^R, x_3 | - j s \alpha_T^S, x_3^S) = & \quad (B.3) \\ & \left[\{(x_3 - x_3^0) \partial_3^{\downarrow}\}^0 + \{(x_3 - x_3^0) \partial_3^{\downarrow}\}^1 + \frac{1}{2} \{(x_3 - x_3^0) \partial_3^{\downarrow}\}^2 \right] \\ & \times \bar{p}^0(j s \alpha_T^R, x_3^0 | - j s \alpha_T^S, x_3^S) + \mathcal{O}((x_3 - x_3^0)^3), \quad \text{for } x_3^0 \leq x_3 \leq x_3^1, \end{aligned}$$

in which we use by definition:

$$\begin{aligned} & \{(x_3 - x_3^0) \partial_3^{\downarrow}\}^n \bar{p}^0(j s \alpha_T^R, x_3^0 | - j s \alpha_T^S, x_3^S) \\ & = (x_3 - x_3^0)^n \lim_{x_3 \downarrow x_3^0} \partial_3^n \bar{p}^0(j s \alpha_T^R, x_3 | - j s \alpha_T^S, x_3^S). \end{aligned} \quad (B.4)$$

To rewrite the first two terms on the right-hand side of Eq. (B.2) we use the following definitions:

$$\begin{aligned} & \partial_3^{\uparrow} \bar{p}^0(j s \alpha_T^R, x_3^0 | - j s \alpha_T^S, x_3^S) \\ & = s \Gamma_0^R [\bar{p}^{0,r}(j s \alpha_T^R, x_3^0 | - j s \alpha_T^S, x_3^S) - \bar{p}^{0,i}(j s \alpha_T^R, x_3^0 | - j s \alpha_T^S, x_3^S)], \end{aligned} \quad (B.5)$$

and,

$$\begin{aligned} \exp(\pm s \Gamma_0^R \Delta x_3) = & \quad (B.6) \\ & 1 \pm s \Gamma_0^R \Delta x_3 + \frac{s^2 (\Gamma_0^R)^2 (\Delta x_3)^2}{2} \pm \frac{s^3 (\Gamma_0^R)^3 (\Delta x_3)^3}{6} \\ & + \frac{s^4 (\Gamma_0^R)^4 (\Delta x_3)^4}{24} + \mathcal{O}[(\Delta x_3)^5]. \end{aligned}$$

This enables us to write the following:

$$\begin{aligned} & \bar{p}^{0,r}(j s \alpha_T^R, x_3^0 | - j s \alpha_T^S, x_3^S) \exp(s \Gamma_0^R \Delta x_3) \\ & + \bar{p}^{0,i}(j s \alpha_T^R, x_3^0 | - j s \alpha_T^S, x_3^S) \exp(-s \Gamma_0^R \Delta x_3) \\ & = \left[\{\Delta x_3 \partial_3^{\uparrow}\}^0 + \{\Delta x_3 \partial_3^{\uparrow}\}^1 + \frac{1}{2} \{\Delta x_3 \partial_3^{\uparrow}\}^2 + \frac{1}{6} \{\Delta x_3 \partial_3^{\uparrow}\}^3 + \frac{1}{24} \{\Delta x_3 \partial_3^{\uparrow}\}^4 \right] \\ & \times \bar{p}^0(j s \alpha_T^R, x_3^0 | - j s \alpha_T^S, x_3^S) + \mathcal{O}[(\Delta x_3)^5], \end{aligned} \quad (B.7)$$

with

$$\{\Delta x_3 \partial_3^{\uparrow}\}^n \bar{p}^0(j s \alpha_T^R, x_3^0 | - j s \alpha_T^S, x_3^S) = \Delta x_3^n \lim_{x_3 \uparrow x_3^0} \partial_3^n \bar{p}^0(j s \alpha_T^R, x_3 | - j s \alpha_T^S, x_3^S). \quad (B.8)$$

Application of the Taylor approximations for exponential terms to the integral term on the right hand side of Eq. (B.2) leads to:

$$\begin{aligned}
& s^2 \int_{x_3^0}^{x_3^1} \frac{\sinh(s\Gamma_0^R(x_3 - x_3^1))}{s\Gamma_0^R} \mathcal{K}\{\bar{p}^0\}(js\alpha_T^R, x_3| - js\alpha_T^S, x_3^S) dx_3 \\
&= s^2 \int_{x_3^0}^{x_3^1} \left[(x_3 - x_3^1) + \frac{(s\Gamma_0^R)^2}{6}(x_3 - x_3^1)^3 + \mathcal{O}[(\Delta x_3)^5] \right] \\
&\quad \times \left[1 + (x_3 - x_3^0)\partial_3^{\frac{1}{2}} + \frac{1}{2}\{(x_3 - x_3^0)\partial_3^{\frac{1}{2}}\}^2 + \mathcal{O}[(\Delta x_3)^3] \right] dx_3 \\
&\quad \times \mathcal{K}\{\bar{p}^0\}(js\alpha_T^R, x_3^0| - js\alpha_T^S, x_3^S).
\end{aligned} \tag{B.9}$$

Using the last two expressions we can rewrite Eq. (B.2) as:

$$\begin{aligned}
& \bar{p}^0(js\alpha_T^R, x_3^1| - js\alpha_T^S, x_3^S) = \\
& \quad \left[\{\Delta x_3 \partial_3^{\frac{1}{2}}\}^0 + \{\Delta x_3 \partial_3^{\frac{1}{2}}\}^1 + \frac{1}{2}\{\Delta x_3 \partial_3^{\frac{1}{2}}\}^2 + \frac{1}{6}\{\Delta x_3 \partial_3^{\frac{1}{2}}\}^3 + \frac{1}{24}\{\Delta x_3 \partial_3^{\frac{1}{2}}\}^4 \right] \\
& \quad \times \bar{p}^0(js\alpha_T^R, x_3^0, -js\alpha_T^S, x_3^S) + \mathcal{O}[(\Delta x_3)^5] \\
& + s^2 \int_{x_3^0}^{x_3^1} \left[(x_3 - x_3^1) + \frac{(s\Gamma_0^R)^2}{6}(x_3 - x_3^1)^3 + \mathcal{O}[(\Delta x_3)^5] \right] \\
& \quad \times \left[1 + (x_3 - x_3^0)\partial_3^{\frac{1}{2}} + \frac{1}{2}\{(x_3 - x_3^0)\partial_3^{\frac{1}{2}}\}^2 + \mathcal{O}[(\Delta x_3)^3] \right] dx_3 \\
& \quad \times \mathcal{K}\{\bar{p}^0\}(js\alpha_T^R, x_3^0| - js\alpha_T^S, x_3^S).
\end{aligned} \tag{B.10}$$

In Eq. (B.7) only terms up to the fourth order of Δx_3 are considered, and analogously we will consider the terms inside the integral up to the fourth order of x_3 . This leaves

us three integral terms to be solved:

$$s^2 \mathcal{K} \{ \bar{p}^0 \} (js\alpha_T^R, x_3^0 | - js\alpha_T^S, x_3^S) \int_{x_3^0}^{x_3^1} (x_3 - x_3^1) dx_3 = \\ - \frac{(x_3^1 - x_3^0)^2}{2} s^2 \mathcal{K} \{ \bar{p}^0 \} (js\alpha_T^R, x_3^0 | - js\alpha_T^S, x_3^S), \quad (\text{B.11})$$

$$s^2 \partial_3^{\frac{1}{3}} \mathcal{K} \{ \bar{p}^0 \} (js\alpha_T^R, x_3^0 | - js\alpha_T^S, x_3^S) \int_{x_3^0}^{x_3^1} (x_3 - x_3^0)(x_3 - x_3^1) dx_3 = \\ - \frac{(x_3^1 - x_3^0)^3}{6} s^2 \partial_3^{\frac{1}{3}} \mathcal{K} \{ \bar{p}^0 \} (js\alpha_T^R, x_3^0 | - js\alpha_T^S, x_3^S), \quad (\text{B.12})$$

$$s^2 \mathcal{K} \{ \bar{p}^0 \} (js\alpha_T^R, x_3^0 | - js\alpha_T^S, x_3^S) \int_{x_3^0}^{x_3^1} \frac{(s\Gamma_0^R)^2}{6} (x_3 - x_3^1)^3 dx_3 + \\ s^2 \partial_3^{\frac{1}{3}2} \mathcal{K} \{ \bar{p}^0 \} (js\alpha_T^R, x_3^0 | - js\alpha_T^S, x_3^S) \int_{x_3^0}^{x_3^1} \frac{(x_3 - x_3^0)^2(x_3 - x_3^1)}{2} dx_3 = \\ - \frac{(s\Gamma_0^R)^2(x_3^1 - x_3^0)^4}{24} s^2 \mathcal{K} \{ \bar{p}^0 \} (js\alpha_T^R, x_3^0 | - js\alpha_T^S, x_3^S) \\ - \frac{(x_3^1 - x_3^0)^4}{24} s^2 \partial_3^{\frac{1}{3}2} \mathcal{K} \{ \bar{p}^0 \} (js\alpha_T^R, x_3^0 | - js\alpha_T^S, x_3^S). \quad (\text{B.13})$$

Substituting all approximations in Eq. (B.2) results in:

$$\bar{p}^0 (js\alpha_T^R, x_3^1 | - js\alpha_T^S, x_3^S) = \left[\{ \Delta x_3 \partial_3^{\frac{1}{3}} \}^0 + \{ \Delta x_3 \partial_3^{\frac{1}{3}} \}^1 \right. \\ + \frac{1}{2} (\Delta x_3)^2 \{ (\partial_3^{\frac{1}{3}})^2 - s^2 \mathcal{K}(js\alpha_T^R) \} + \frac{1}{6} (\Delta x_3)^3 \{ (\partial_3^{\frac{1}{3}})^3 - s^2 \mathcal{K}(js\alpha_T^R) \partial_3^{\frac{1}{3}} \} \\ \left. + \frac{1}{24} (\Delta x_3)^4 \{ (\partial_3^{\frac{1}{3}})^4 - s^2 \mathcal{K}(js\alpha_T^R) ((\partial_3^{\frac{1}{3}})^2 + (\partial_3^{\frac{1}{3}})^2) \} \right] \\ \times \bar{p}^0 (js\alpha_T^R, x_3^0 | - js\alpha_T^S, x_3^S) + \mathcal{O}[(\Delta x_3)^5], \quad (\text{B.14})$$

where $\Delta x_3 = x_3^1 - x_3^0$. Note that in this notation $\mathcal{K}(js\alpha_T^R)$ is a convolutional operator working only on $\bar{p}(js\alpha_T^R, x_3^0 | - js\alpha_T^S, x_3^S)$. We take a closer look at the

known Taylor expansion of \bar{p}^0 :

$$\begin{aligned} \bar{p}^0 (js\alpha_T^R, x_3^1) - js\alpha_T^S, x_3^S) &= \left[\{\Delta x_3 \partial_3^\downarrow\}^0 + \{\Delta x_3 \partial_3^\downarrow\}^1 + \frac{1}{2} \{\Delta x_3 \partial_3^\downarrow\}^2 \right. \\ &\quad \left. + \frac{1}{6} \{\Delta x_3 \partial_3^\downarrow\}^3 + \frac{1}{24} \{\Delta x_3 \partial_3^\downarrow\}^4 \right] \bar{p}^0 (js\alpha_T^R, x_3^0) - js\alpha_T^S, x_3^S) + \mathcal{O}[(\Delta x_3)^5]. \end{aligned} \quad (\text{B.15})$$

Comparing the same powers of Δx_3 for both approximations we find the following three expressions:

$$\begin{aligned} (\partial_3^\uparrow)^0 \bar{p}^0 &= (\partial_3^\downarrow)^0 \bar{p}^0, \\ (\partial_3^\uparrow)^1 \bar{p}^0 &= (\partial_3^\downarrow)^1 \bar{p}^0, \\ \{(\partial_3^\uparrow)^2 - s^2 \mathcal{K}\} \bar{p}^0 &= (\partial_3^\downarrow)^2 \bar{p}^0. \end{aligned} \quad (\text{B.16})$$

The first equation states the well-known boundary condition that the pressure field is continuous over a boundary. The second equation is recognized as the boundary condition of continuity of the particle velocity over a boundary. The third equation shows a jump in the second derivative of the pressure field proportional to the contrast over the boundary. This term is used in the derivation of the imaging condition in section 2.3.1. Note that all these conclusions are still under the assumption that the mass density is a constant. We can rewrite the last conclusion as:

$$\{(\partial_3^\uparrow)^2 - (\partial_3^\downarrow)^2\} \bar{p}^0 = s^2 \mathcal{K} \bar{p}^0. \quad (\text{B.17})$$

Using the three equations (B.16) we can rewrite Eq. (B.14) as:

$$\begin{aligned} \bar{p}^0 (js\alpha_T^R, x_3^1) - js\alpha_T^S, x_3^S) &= \left[\{\Delta x_3 \partial_3^\uparrow\}^0 + \{\Delta x_3 \partial_3^\uparrow\}^1 \right. \\ &\quad \left. + \frac{1}{2} s^2 (\Delta x_3)^2 \{(\Gamma_0^R)^2 - \mathcal{K}(js\alpha_T^R)\} + \frac{1}{6} s^2 (\Delta x_3)^3 \{(\Gamma_0^R)^2 - \mathcal{K}(js\alpha_T^R)\} \partial_3^\uparrow \right. \\ &\quad \left. + \frac{1}{24} s^4 (\Delta x_3)^4 \{(\Gamma_0^R)^2 - \mathcal{K}(js\alpha_T^R)\}^2 \right] \\ &\quad \times \bar{p}^0 (js\alpha_T^R, x_3^0) - js\alpha_T^S, x_3^S) + \mathcal{O}[(\Delta x_3)^5], \end{aligned} \quad (\text{B.18})$$

where we used $(\partial_3^\uparrow)^2 = s^2 (\Gamma_0^R)^2$. We now introduce the square-root operator \mathcal{H} according to:

$$\mathcal{H}(js\alpha_T^R) = \sqrt{(\Gamma_0^R)^2 - \mathcal{K}(js\alpha_T^R)}, \quad (\text{B.19})$$

where $\mathcal{K}(js\alpha_T^R)$ is still a convolutional operator working only on $\bar{p}(js\alpha_T^R, x_3^0) - js\alpha_T^S, x_3^S)$. Substituting this in Eq. (B.18) we recognize the Taylor

expansions of sinh and cosh:

$$\sinh(x) = x + \frac{x^3}{3!} + \mathcal{O}[x^5], \quad (\text{B.20})$$

$$\cosh(x) = 1 + \frac{x^2}{2!} + \frac{x^4}{4!} + \mathcal{O}[x^6], \quad (\text{B.21})$$

and we can write:

$$\begin{aligned} \bar{p}^0(j s \alpha_T^R, x_3^1 | - j s \alpha_T^S, x_3^S) &= \\ &\cosh(s \mathcal{H}(j s \alpha_T^R) \Delta x_3) \bar{p}^0(j s \alpha_T^R, x_3^0 | - j s \alpha_T^S, x_3^S) \\ &+ \frac{\sinh(s \mathcal{H}(j s \alpha_T^R) \Delta x_3)}{s \mathcal{H}(j s \alpha_T^R)} \partial_3^\uparrow \bar{p}^0(j s \alpha_T^R, x_3^0 | - j s \alpha_T^S, x_3^S). \end{aligned} \quad (\text{B.22})$$

Now we will follow Fokkema *et al.* in [18] by taking a closer look at how to solve Eq. (B.1):

$$\begin{aligned} s^2 \hat{W} \int_{x_3^0}^{x_3^1} \frac{\exp(-s \Gamma_0^R(x_3 - x_3^0))}{2s \Gamma_0^R} \mathcal{K}\{\bar{p}^0\}(j s \alpha_T^R, x_3 | - j s \alpha_T^S, x_3^S) dx_3 \\ + \frac{\exp(-s \Gamma_0^R \Delta x_3)}{(2\pi)^2} \int_{s \alpha_T \epsilon \mathbb{R}^2} \bar{p}^{1,r}(j s \alpha_T^R, x_3^1 | - j s \alpha_T^S, x_3^S) dA \times \\ s^2 \int_{x_3^0}^{x_3^1} \exp(s \Gamma_0(x_3 - x_3^S)) \mathcal{K}\{\bar{p}^0\}(j s \alpha_T, x_3 | - j s \alpha_T^S, x_3^S) dx_3 \\ = \hat{W}[\bar{p}^{0,r}(j s \alpha_T^R, x_3^0 | - j s \alpha_T^S, x_3^S) \\ - \bar{p}^{1,r}(j s \alpha_T^R, x_3^1 | - j s \alpha_T^S, x_3^S) \exp(-s \Gamma_0^R \Delta x_3)]. \end{aligned} \quad (\text{B.23})$$

This equation is used to determine the upgoing wavefield after velocity replacement. When we substitute the result of the wavefield extrapolation, Eq. (B.22) in Eq. (B.23) we find an integral equation of the second kind. We will write this in the following compact notation:

$$\begin{aligned} X(j s \alpha_T^R, j s \alpha_T^S) + \frac{1}{(2\pi)^2} \int_{s \alpha_T \epsilon \mathbb{R}^2} L(j s \alpha_T, j s \alpha_T^S) X(j s \alpha_T^R, j s \alpha_T) dA \\ = Y(j s \alpha_T^R, j s \alpha_T^S), \end{aligned} \quad (\text{B.24})$$

with

$$X(j s \alpha_T^R, j s \alpha_T^S) = \bar{p}^{1,r}(j s \alpha_T^R, x_3^1 | - j s \alpha_T^S, x_3^S), \quad (\text{B.25})$$

$$\begin{aligned}
Y(j s \alpha_T^R, j s \alpha_T^S) &= \bar{p}^{0,r}(j s \alpha_T^R, x_3^0 | -j s \alpha_T^S, x_3^S) \exp(s \Gamma_0^R \Delta s_3) \quad (B.26) \\
&- s^2 \exp(s \Gamma_0^R \Delta s_3) \int_{x_3^0}^{x_3^1} \frac{\exp(-s \Gamma_0^R (x_3 - x_3^0))}{2 s \Gamma_0^R} \left[\cosh(s \mathcal{H}(j s \alpha_T^R) \Delta x_3) \right. \\
&\left. + \frac{\sinh(s \mathcal{H}(j s \alpha_T^R) \Delta x_3)}{s \mathcal{H}(j s \alpha_T^R)} \partial_3^\uparrow \right] \mathcal{K}\{\bar{p}^0\}(j s \alpha_T^R, x_3^0 | -j s \alpha_T^S, x_3^S) dx_3
\end{aligned}$$

and

$$\begin{aligned}
L(j s \alpha_T, j s \alpha_T^S) &= \quad (B.27) \\
&\hat{W} \int_{x_3^0}^{x_3^1} \exp(s \Gamma_0(x_3 - x_3^S)) \left[\cosh(s \mathcal{H}(j s \alpha_T^R) \Delta x_3) + \frac{\sinh(s \mathcal{H}(j s \alpha_T^R) \Delta x_3)}{s \mathcal{H}(j s \alpha_T^R)} \partial_3^\uparrow \right] \\
&\times \mathcal{K}\{\bar{p}^0\}(j s \alpha_T^R, x_3^0 | -j s \alpha_T^S, x_3^S) dx_3
\end{aligned}$$

The expression for $L(j s \alpha_T, j s \alpha_T^S)$ is called the kernel function. To compute $\partial_3^\uparrow \bar{p}^0$ in Eqs. (B.26) and (B.27) we make use of:

$$\partial_3^\uparrow \bar{p}^0 = s \Gamma_0(\bar{p}^{0,r} - \bar{p}^{0,i}), \quad (B.28)$$

where the minus sign accounts for the difference in propagation of the incident and reflected wavefield in the upper half-space. Eq. (B.24) is the proposed equation that is to be used for the velocity replacement in laterally variant media. A way to solve this equation is the Neumann expansion. We rewrite Eq (B.24) as:

$$X(j s \alpha_T^R, j s \alpha_T^S) = Y(j s \alpha_T^R, j s \alpha_T^S) \quad (B.29)$$

$$\begin{aligned}
&- \frac{1}{(2\pi)^2} \int_{s \alpha_T \epsilon \mathbb{R}^2} L(j s \alpha_T, j s \alpha_T^S) X(j s \alpha_T^R, j s \alpha_T) dA. \\
&\quad (B.30)
\end{aligned}$$

This can be solved using a Neumann iterative solution:

$$\begin{aligned}
X^{(n)}(j s \alpha_T^R, j s \alpha_T^S) &= Y(j s \alpha_T^R, j s \alpha_T^S) \quad (B.31) \\
&- \frac{1}{(2\pi)^2} \int_{s \alpha_T \epsilon \mathbb{R}^2} L(j s \alpha_T, j s \alpha_T^S) X^{(n-1)}(j s \alpha_T^R, j s \alpha_T) dA, \\
&\quad n = 1, 2, \dots
\end{aligned}$$

and

$$X^{(0)}(j s \alpha_T^R, j s \alpha_T^S) = Y^{(0)}(j s \alpha_T^R, j s \alpha_T^S). \quad (B.32)$$

$X^{(n)}$ is the approximate solution after n iteration steps.

In order to solve the basic equations, data has to be available for each source and receiver position. This means that each source position is also a receiver position and the other way around.

C

Mathematical relations: Parseval's theorem and Hilbert transform

C.1 Parseval's theorem

In the derivation of the wavefield extrapolation method we make use of Parseval's theorem. In most texts, Parseval's theorem is defined as:

$$\int_{-\infty}^{\infty} x^2(t)dt = \frac{1}{2\pi} \int_{-\infty}^{\infty} |\hat{x}(\omega)|^2 d\omega, \quad (\text{C.1})$$

where ω is the frequency. We derive a more general form of Parseval's theorem, for the spatial coefficients \mathbf{x}_T . We start with the functions $\phi(\mathbf{x}_T)$, $\psi(\mathbf{x}_T)$ and their Fourier transforms $\hat{\phi}(js\alpha_T)$ and $\hat{\psi}(js\alpha_T)$:

$$\hat{\phi}(js\alpha_T) = \int_{\mathbf{x}_T \in \mathbb{R}^2} \exp(js\alpha_\gamma x_\gamma) \phi(\mathbf{x}_T) dA, \quad (\text{C.2})$$

$$\phi(\mathbf{x}_T) = \frac{1}{(2\pi)^2} \int_{s\alpha_T \in \mathbb{R}^2} \exp(-js\alpha_\gamma x_\gamma) \hat{\phi}(js\alpha_T) dA, \quad (\text{C.3})$$

$$\hat{\psi}(js\alpha'_T) = \int_{\mathbf{x}_T \in \mathbb{R}^2} \exp(js\alpha'_\gamma x_\gamma) \psi(\mathbf{x}_T) dA, \quad (\text{C.4})$$

$$\psi(\mathbf{x}_T) = \frac{1}{(2\pi)^2} \int_{s\alpha'_T \in \mathbb{R}^2} \exp(-js\alpha'_\gamma x_\gamma) \hat{\psi}(js\alpha'_T) dA, \quad (\text{C.5})$$

where $\gamma = \{1, 2\}$. We proceed as follows:

$$\begin{aligned} \int_{\mathbf{x}_T \in \mathbb{R}} \phi(\mathbf{x}_T) \psi(\mathbf{x}_T) dA &= \int_{\mathbf{x}_T \in \mathbb{R}} \frac{1}{(2\pi)^4} \int_{s\alpha_T \in \mathbb{R}^2} \exp(-js\alpha_q x_q) \hat{\phi}(js\alpha_T) dA \\ &\quad \times \int_{s\alpha'_T \in \mathbb{R}^2} \exp(-js\alpha'_\gamma x_\gamma) \hat{\psi}(js\alpha'_T) dA dA. \end{aligned} \quad (\text{C.6})$$

Rewriting this we find:

$$\int_{\mathbf{x}_T \in \mathbb{R}^2} \phi(\mathbf{x}_T) \psi(\mathbf{x}_T) dA = \frac{1}{(2\pi)^4} \int_{s\boldsymbol{\alpha}_T \in \mathbb{R}^2} \hat{\phi}(js\boldsymbol{\alpha}_T) dA \int_{s\boldsymbol{\alpha}'_T \in \mathbb{R}} \hat{\psi}(js\boldsymbol{\alpha}'_T) dA \\ \times \int_{\mathbf{x}_T \in \mathbb{R}^2} \exp(-jx_\gamma(s\boldsymbol{\alpha}'_\gamma + s\boldsymbol{\alpha}_\gamma)) dA. \quad (\text{C.7})$$

We will solve the last integral of Eq. (C.7) using a familiar integration result:

$$\int_{x \in \mathbb{R}^2} \exp(jsx) dA = 2\pi\delta(jsx), \quad (\text{C.8})$$

and we find:

$$\int_{\mathbf{x}_T \in \mathbb{R}^2} \phi(\mathbf{x}_T) \psi(\mathbf{x}_T) dA = \frac{1}{(2\pi)^2} \int_{s\boldsymbol{\alpha}_T \in \mathbb{R}^2} \hat{\phi}(js\boldsymbol{\alpha}_T) dA \int_{s\boldsymbol{\alpha}'_T \in \mathbb{R}^2} \hat{\psi}(js\boldsymbol{\alpha}'_T) \delta(s\boldsymbol{\alpha}'_T + s\boldsymbol{\alpha}_T) dA. \quad (\text{C.9})$$

This leaves a general Parseval relation:

$$\int_{\mathbf{x}_T \in \mathbb{R}^2} \phi(\mathbf{x}_T) \psi(\mathbf{x}_T) dA = \frac{1}{(2\pi)^2} \int_{s\boldsymbol{\alpha}_T \in \mathbb{R}^2} \hat{\phi}(js\boldsymbol{\alpha}_T) \hat{\psi}(-js\boldsymbol{\alpha}_T) dA. \quad (\text{C.10})$$

We use this relation in Equation (2.26) in the derivation of the wavefield extrapolation method.

C.2 The Hilbert transform

Following Aki and Richards [2] the Hilbert transform is defined as:

$$\mathcal{F}(\mathcal{H}[f(t)]) = -i \times \text{sgn}(\omega) f(\omega), \quad (\text{C.11})$$

where $\text{sgn}(\omega) = \pm 1$ as $\omega \gtrless 0$, \mathcal{F} is the Fourier transform and \mathcal{H} denotes the Hilbert transform. To compute the Hilbert transform, $f(t)$ is transformed to the frequency domain, where the real and imaginary parts are interchanged, with for the positive frequencies a sign change in the resulting imaginary part. This is equivalent to a phase shift over $\frac{\pi}{2}$. The Hilbert transform $\mathcal{H}[f(t)]$ is then found by an inverse Fourier transform.

D

The Schur algorithm

The Schur algorithm [27] is known as a fast algorithm suited for high-speed data processing. The algorithm uses a layer-stripping procedure to reconstruct a lossless scattering medium described by symmetric two-component wave equations. The method can be applied to solve the inverse problem for a layered acoustic medium [39] but can also be used for many other problems such as the reconstruction of nonuniform lossless transmission lines or the linear least-squares estimation of stationary stochastic processes [40]. We will follow Yagle and Levy [39] to show how the Schur algorithm can be applied for inversion of a layered acoustic medium. This will be followed by an alternative solution and some imaging results using this solution.

D.1 Inversion of a layered acoustic medium

The acoustic medium to be reconstructed consists of a homogeneous upper half-space with known density ρ_0 and sound speed c_0 extending over $x_3 < 0$, and of a horizontally layered inhomogeneous lower half-space with unknown density $\rho(x_3)$ and unknown propagation velocity $c(x_3)$. An impulsive plane pressure wave, propagating in the x_3 direction, is incident on the inhomogeneous lower half-space at $t = 0$. Using the acoustic equation and the stress-strain equation (Berkhout [3]) the following system is obtained:

$$\begin{aligned}\partial_3 p + \rho \partial_t v &= 0, \\ \partial_3 v + \kappa \partial_t p &= 0,\end{aligned}\tag{D.1}$$

in which:

$$\kappa = \frac{1}{\rho c^2}.\tag{D.2}$$

A change of variables is made from depth x_3 to travel-time τ using

$$\tau = \int_0^{x_3} \frac{1}{c(x'_3)} dx'_3.\tag{D.3}$$

We can now write for the system of wave equations:

$$\begin{aligned}\partial_\tau p &= -Z(\tau)\partial_t v, \\ \partial_\tau v &= -Z^{-1}(\tau)\partial_t p,\end{aligned}\quad (\text{D.4})$$

where $Z(\tau) = \rho(\tau)c(\tau)$ is the acoustic impedance. Now we define the following normalized quantities:

$$\psi(\tau, t) = Z^{-\frac{1}{2}}(\tau)p(\tau, t) = \text{normalized pressure} \quad (\text{D.5})$$

$$\phi(\tau, t) = Z^{\frac{1}{2}}(\tau)v(\tau, t) = \text{normalized velocity}, \quad (\text{D.6})$$

We now make the following change of variables

$$p^{\text{down}}(\tau, t) = \frac{1}{2}(\psi + \phi), \quad (\text{D.7})$$

$$p^{\text{up}}(\tau, t) = \frac{1}{2}(\psi - \phi), \quad (\text{D.8})$$

where p^{up} is the normalized upgoing wave and p^{down} the normalized downgoing wave. A similar definition for the up- and downgoing wavefields is given by Claerbout [10]. Eqs. (D.4) can now be transformed into the two-component wave system

$$\begin{aligned}\partial_\tau p^{\text{down}}(\tau, t) + \partial_t p^{\text{down}}(\tau, t) &= -r(\tau)p^{\text{up}}(\tau, t), \\ \partial_\tau p^{\text{up}}(\tau, t) - \partial_t p^{\text{up}}(\tau, t) &= -r(\tau)p^{\text{down}}(\tau, t),\end{aligned}\quad (\text{D.9})$$

where the reflectivity function $r(\tau)$ is given by

$$r(\tau) = \frac{1}{2}\partial_\tau \ln Z(\tau). \quad (\text{D.10})$$

After normalization, the up- and downgoing waves for the normal-incidence problem can be written as:

$$p^{\text{down}}(\tau, t) = \delta(t - \tau) + \tilde{p}(t)\chi(t - \tau), \quad (\text{D.11})$$

$$p^{\text{up}}(\tau, t) = \tilde{p}(t)\chi(t - \tau), \quad (\text{D.12})$$

where the tilde denotes a smooth function. We will take a closer look at the definition of p^{up} and p^{down} in the next section. Substituting Eqs. (D.11) in Eqs. (D.9) we find that

$$r(\tau) = 2\tilde{p}^{\text{up}}(\tau, \tau). \quad (\text{D.13})$$

Together with Eqs. (D.9) this forms the so-called Cholesky recursion system. The starting points for the recursion are the up- and downgoing wavefields $p^{\text{up}}(0, t)$ and $p^{\text{down}}(0, t)$ which are measured on the surface of the inhomogeneous medium. The

partial derivatives in Eqs. (D.9) are solved using an Euler-Cauchy approximation. To calculate the impedance for each layer leading to the results shown in section 4.2.1 we used

$$r(\tau) = \frac{Z(\tau + \Delta) - Z(\tau)}{Z(\tau + \Delta) + Z(\tau)}, \quad (\text{D.14})$$

where Δ is the discretization step. We also took the density ρ to be constant.

D.2 Alternative Schur solution

We now propose a theoretically more accurate solution, where we use a more exact way of determining the reflectivity function. The following 1D wave problem is considered:

$$\begin{aligned} \partial_\tau p^{\text{down}} + \partial_t p^{\text{down}} &= S - rp^{\text{up}}, \\ \partial_\tau p^{\text{up}} - \partial_t p^{\text{up}} &= -rp^{\text{down}}, \end{aligned} \quad (\text{D.15})$$

with the normalized downgoing wave

$$p^{\text{down}} = p^{\text{down}}(\tau, t)\chi(t - \tau). \quad (\text{D.16})$$

We have now defined the source term separately, as opposed to section D.1, Eq. (D.11), where the downgoing wavefield was defined to contain a probing impulse initiating the waves. The source term S is defined as

$$S(\tau, t) = w(t - \tau)\delta(\tau), \quad (\text{D.17})$$

where w is the wavelet which is preceded by an impulse. The normalized upgoing wave is given by

$$p^{\text{up}} = p^{\text{up}}(\tau, t)\chi(t - \tau), \quad (\text{D.18})$$

and the reflectivity function $r(\tau)$ is given by

$$r(\tau) = \frac{1}{2Z}\partial_\tau Z, \quad (\text{D.19})$$

where $Z(\tau)$ is the impedance. We split the downgoing wavefield in an incident wavefield p_i^{down} and a scattered wavefield p_s^{down} in the following way:

$$\begin{aligned} \partial_\tau p_i^{\text{down}} + \partial_t p_i^{\text{down}} &= S, \\ \partial_\tau p_s^{\text{down}} + \partial_t p_s^{\text{down}} &= -rp^{\text{up}}, \end{aligned} \quad (\text{D.20})$$

where we have:

$$p^{\text{down}}(\tau, t) = p_i^{\text{down}}(\tau, t) + p_s^{\text{down}}(\tau, t). \quad (\text{D.21})$$

To solve this scattering problem we use the general solution of the following differential equation

$$\partial_\tau a \pm \partial_t a = b, \quad (D.22)$$

with $a = a(\tau, t)$ and $b = b(\tau, t)$ and the condition that $t \geq \tau$. The general solution is given by:

$$a(\tau, t) = \int_0^\tau b(\tau', \tau \mp \tau \pm \tau') d\tau'. \quad (D.23)$$

With the aid of Eq. (D.23) the incident field is given by:

$$\begin{aligned} p_i^{\text{down}}(\tau, t) &= \int_0^\tau S(\tau', t - \tau + \tau') d\tau' \\ &= \int_0^\tau w(t - \tau + \tau') \delta(\tau') d\tau' \\ &= w(t - \tau) \int_0^\tau \delta(\tau') d\tau' \\ &= w(t - \tau) \chi(t - \tau) \chi(\tau). \end{aligned} \quad (D.24)$$

Using the same general solution the scattered downgoing wavefield is given by:

$$p_s^{\text{down}}(\tau, t) = - \int_0^\tau r(\tau') p_i^{\text{down}}(\tau', t - \tau + \tau') d\tau'. \quad (D.25)$$

By using this general solution in the second expression of Eq. (D.15) we find for the upgoing wavefield:

$$\begin{aligned} p_i^{\text{up}}(\tau, t) &= - \int_0^\tau r(\tau') p_i^{\text{down}}(\tau', t + \tau - \tau') d\tau' \\ &\quad - \int_0^\tau r(\tau') p_s^{\text{down}}(\tau', t + \tau - \tau') d\tau'. \end{aligned} \quad (D.26)$$

Then, using the solution for the incident downgoing wavefield, Eq. (D.24), in the solution for the upgoing wavefield, Eq. (D.26), we find the following set of equations:

$$\begin{aligned} p_s^{\text{down}}(\tau, t) &= - \int_0^\tau r(\tau') p^{\text{up}}(\tau', t - \tau + \tau') d\tau', \\ p^{\text{up}}(\tau, t) &= - \int_0^\tau r(\tau') w(t + \tau - 2\tau') \chi(t + \tau - 2\tau') d\tau' \\ &\quad - \int_0^\tau r(\tau') p_s^{\text{down}}(\tau', t + \tau - \tau') d\tau'. \end{aligned} \quad (\text{D.27})$$

For causal wavefields ($t \geq \tau$) we observe that we can write Eqs. (D.27) as:

$$\begin{aligned} p_s^{\text{down}}(\tau, t) &= - \int_0^\tau r(\tau') p^{\text{up}}(\tau', t - \tau + \tau') d\tau', \\ p^{\text{up}}(\tau, t) &= - \int_0^\tau r(\tau') w(t + \tau - 2\tau') d\tau' - \int_0^\tau r(\tau') p_s^{\text{down}}(\tau', t + \tau - \tau') d\tau'. \end{aligned} \quad (\text{D.28})$$

The aim of inversion is to determine the reflectivity function $r = r(\tau)$ from the surface measurement of the upgoing wavefield $p^{\text{up}} = p^{\text{up}}(0, t)$. Therefore we introduce $w(t - \tau) = \Delta\delta(t - \tau)$ where $\Delta = \Delta t = \Delta\tau$ is the sampling rate. Then the system (D.28) can be written as:

$$\begin{aligned} p_s^{\text{down}}(\tau, t) &= - \int_0^\tau r(\tau') p^{\text{up}}(\tau', t - \tau + \tau') d\tau', \\ p^{\text{up}}(\tau, t) &= \frac{1}{2} \Delta r(\tau) \left(\frac{t + \tau}{2} \right) - \int_0^\tau r(\tau') p_s^{\text{down}}(\tau', t + \tau - \tau') d\tau', \end{aligned} \quad (\text{D.29})$$

where we used:

$$\begin{aligned} \Delta \int_0^\tau r(\tau') \delta(t + \tau - 2\tau') d\tau' &= \frac{\Delta}{2} \int_0^\tau r(\tau') \delta\left(\tau' - \left(\frac{t + \tau}{2}\right)\right) d\tau' \\ &= -\frac{\Delta}{2} r\left(\frac{t + \tau}{2}\right). \end{aligned} \quad (\text{D.30})$$

Since the increment of τ and t are the same, and denoted by Δ , it follows from Eqs. (D.29):

$$\begin{aligned} p_s^{\text{down}}(\tau + \Delta, t + \Delta) &= - \int_0^{\tau + \Delta} r(\tau') p^{\text{up}}(\tau', t - \tau + \tau') d\tau', \\ &= p_s^{\text{down}}(\tau, t) - \int_{\tau}^{\tau + \Delta} r(\tau') p^{\text{up}}(\tau', t - \tau + \tau'), \end{aligned} \quad (\text{D.31})$$

and:

$$\begin{aligned} p^{\text{up}}(\tau + \Delta, t - \Delta) &= \frac{1}{2} \Delta r\left(\frac{t + \tau}{2}\right) - \int_0^{\tau + \Delta} r(\tau') p_s^{\text{down}}(\tau', t + \tau - \tau') d\tau', \\ &= p^{\text{up}}(\tau, t) - \int_{\tau}^{\tau + \Delta} r(\tau') p_s^{\text{down}}(\tau', t + \tau - \tau') d\tau'. \end{aligned} \quad (\text{D.32})$$

From Eq. (D.31) it directly follows that:

$$p_s^{\text{down}}(\tau, t) = p_s^{\text{down}}(\tau - \Delta, t - \Delta) - \int_{\tau - \Delta}^{\tau} r(\tau') p^{\text{up}}(\tau', t - \tau + \tau') d\tau', \quad (\text{D.33})$$

and from Eq. (D.32):

$$p^{\text{up}}(\tau, t) = p^{\text{up}}(\tau - \Delta, t + \Delta) - \int_{\tau - \Delta}^{\tau} r(\tau') p_s^{\text{down}}(\tau, t + \tau - \tau') d\tau'. \quad (\text{D.34})$$

We observe from Eqs. (D.33) and (D.34) that $p_s^{\text{down}}(\tau, t)$ and $p^{\text{up}}(\tau, t)$ can be determined from $p_s^{\text{down}}(\tau - \Delta, t - \Delta)$ and $p^{\text{up}}(\tau - \Delta, t + \Delta)$. To obtain the recursion scheme that enables this operation we discretize Eqs. (D.33) and (D.34) and use the trapezoidal rule. We define:

$$\begin{aligned} \tau &= m\Delta & m &= 0, 1, 2, \dots, \\ t &= (m + n)\Delta & n &= 0, 1, 2, \dots. \end{aligned} \quad (\text{D.35})$$

Using this discretization we obtain:

$$\begin{aligned} p_s^{\text{down}}(m, m + n) &= p_s^{\text{down}}(m - 1, m + n - 1) \\ &\quad - \frac{1}{2} \bar{r}(m - 1) p^{\text{up}}(m - 1, m + n - 1) \\ &\quad - \frac{1}{2} \bar{r}(m) p^{\text{up}}(m, m + n), \end{aligned} \quad (\text{D.36})$$

and

$$\begin{aligned} p^{\text{up}}(m, m+n) &= p^{\text{up}}(m-1, m+n+1) \\ &\quad - \frac{1}{2} \bar{r}(m-1) p_s^{\text{down}}(m-1, m+n+1) \\ &\quad - \frac{1}{2} \bar{r}(m) p_s^{\text{down}}(m, m+n), \end{aligned} \quad (\text{D.37})$$

in which:

$$\begin{aligned} \bar{r}(m) &= \frac{1}{2} \Delta \frac{1}{Z(m)} \frac{\partial}{\partial \tau} Z(m) \Big|_{\tau=m\Delta} \\ &= \frac{1}{2} \Delta \frac{1}{Z(m)} \frac{Z(m+1) - Z(m)}{Z(m)} \\ &= \frac{1}{2} \frac{Z(m+1) - Z(m)}{Z(m)} \approx \frac{Z(m+1) - Z(m)}{Z(m+1) + Z(m)}. \end{aligned} \quad (\text{D.38})$$

From Eqs. (D.36) and (D.37) we can deduce the following system:

$$\begin{pmatrix} 1 & \frac{1}{2} \bar{r}(m) \\ \frac{1}{2} \bar{r}(m) & 1 \end{pmatrix} \begin{pmatrix} p_s^{\text{down}}(m, m+n) \\ p^{\text{up}}(m, m+n) \end{pmatrix} = \begin{pmatrix} p_s^{\text{down}}(m-1, m+n-1) - \frac{1}{2} \bar{r}(m-1) p^{\text{up}}(m-1, m+n-1) \\ -\frac{1}{2} \bar{r}(m-1) p_s^{\text{down}}(m-1, m+n+1) + q(m-1, m+n+1) \end{pmatrix}. \quad (\text{D.39})$$

Hence we have:

$$\begin{pmatrix} p_s^{\text{down}}(m, m+n) \\ p^{\text{up}}(m, m+n) \end{pmatrix} = \frac{1}{1 - \frac{1}{4} \bar{r}(m)^2} \begin{pmatrix} 1 & -\frac{1}{2} \bar{r}(m) \\ -\frac{1}{2} \bar{r}(m) & 1 \end{pmatrix} \times \mathbf{B}, \quad (\text{D.40})$$

for $m = 0, 1, 2, 3, \dots$, and $n = 0, 1, 2, 3, \dots$.

where

$$\mathbf{B} = \begin{pmatrix} p_s^{\text{down}}(m-1, m+n-1) - \frac{1}{2} \bar{r}(m-1) p^{\text{up}}(m-1, m+n-1) \\ -\frac{1}{2} \bar{r}(m-1) p_s^{\text{down}}(m-1, m+n+1) + q(m-1, m+n+1) \end{pmatrix}. \quad (\text{D.41})$$

In the paper by Bruckstein and Levy [5] the square rule was used instead of the trapezoidal rule. In that case Eqs. (D.36) and (D.37) are:

$$\begin{aligned} p_s^{\text{down}}(m, m+n) &= p_s^{\text{down}}(m-1, m+n-1) \\ &\quad - \bar{r}(m-1) p^{\text{up}}(m-1, m+n-1), \end{aligned} \quad (\text{D.42})$$

$$\begin{aligned} p^{\text{up}}(m, m+n) &= p^{\text{up}}(m-1, m+n-1) \\ &\quad - \bar{r}(m-1) p_s^{\text{down}}(m-1, m+n+1). \end{aligned} \quad (\text{D.43})$$

These equations form a simplified version of Eq. (D.40). In order to solve system (D.40) we need to know the reflectivity $\bar{r}(m)$. To that end we consider Eq. (D.29) and considering $p^{\text{up}}(\tau, \tau)$ we arrive at:

$$p^{\text{up}}(\tau, \tau) = \frac{1}{2}\bar{r}(\tau) - \int_0^\tau r(\tau')p_s^{\text{down}}(\tau', 2\tau - \tau')d\tau', \quad (\text{D.44})$$

or

$$\frac{1}{2}\bar{r}(\tau) = p^{\text{up}}(\tau, \tau) - \int_0^\tau r(\tau')p_s^{\text{down}}(\tau', 2\tau - \tau')d\tau'. \quad (\text{D.45})$$

Note that the integral contribution on the right-hand side of this equation to the reflection function $\bar{r}(\tau)$ is of the order $\bar{r}(\tau)^2$ since also p_s^{down} depends linearly on $\bar{r}(\tau)$. In section D.1 $r(\tau)$ was approximated by neglecting the integral contribution leaving:

$$\frac{1}{2}r(\tau) \approx p^{\text{up}}(\tau, \tau), \quad (\text{D.46})$$

which is not correct in the strict sense. From Eq. (D.34) it follows that:

$$p^{\text{up}}(\tau, \tau) = p^{\text{up}}(\tau - \Delta, \tau + \Delta) - \int_{\tau - \Delta}^\tau r(\tau')p_s^{\text{down}}(\tau', 2\tau - \tau')d\tau'. \quad (\text{D.47})$$

Substitution of Eq. (D.47) into Eq. (D.45) yields:

$$\frac{1}{2}\bar{r}(\tau) = p^{\text{up}}(\tau - \Delta, \tau + \Delta) - \int_0^{\tau - \Delta} r(\tau')p_s^{\text{down}}(\tau', 2\tau - \tau')d\tau', \quad (\text{D.48})$$

and when we discretize this equation we obtain:

$$\begin{aligned} \frac{1}{2}\bar{r}(m) &= p_s^{\text{up}}(m - 1, m + 1) - \frac{1}{2}\bar{r}(m - 1)p_s^{\text{down}}(m - 1, m + 1) \\ &\quad - \sum_{n=1}^{m-2} \bar{r}(n)p_s^{\text{down}}(n, 2m - n), \end{aligned} \quad (\text{D.49})$$

which together with the system (D.40) is a consistent computational scheme. We use Eq. (D.49) to determine the reflectivity, and Eq. (D.40) to extrapolate the wavefield. The evaluation is started for $r(0) = 0$ in Eq. (D.49). $p^{\text{up}}(0, t)$ is the upgoing wavefield

measured at the surface. To give an impression we write the expansion:

$$\begin{aligned}
 \frac{1}{2}\bar{r}(1) &= p^{\text{up}}(0, 2), \\
 \frac{1}{2}\bar{r}(2) &= p^{\text{up}}(1, 3) - \frac{1}{2}\bar{r}(1)p_s^{\text{down}}(1, 3), \\
 \frac{1}{2}\bar{r}(3) &= p^{\text{up}}(2, 4) - \frac{1}{2}\bar{r}(2)p_s^{\text{down}}(2, 4) - \bar{r}(1)p_s^{\text{down}}(1, 5), \\
 \frac{1}{2}\bar{r}(4) &= p^{\text{up}}(3, 5) - \frac{1}{2}\bar{r}(3)p_s^{\text{down}}(3, 5) - \bar{r}(1)p_s^{\text{down}}(1, 7) \\
 &\quad - \bar{r}(2)p_s^{\text{down}}(2, 6), \\
 \text{etc.} &
 \end{aligned} \tag{D.50}$$

Note that for this algorithm the only field required as input is the upgoing field measured at the surface. The reflected downgoing field is of course zero at the surface. Since we introduced $w(t - \tau) = \Delta\delta(t - \tau)$ the measured reflected wavefield consists of pulses only. The imaging result for this method together with the actual velocity model is shown in figure D.1. The first interfaces are imaged accurately but with increasing depth the mistake also increases.

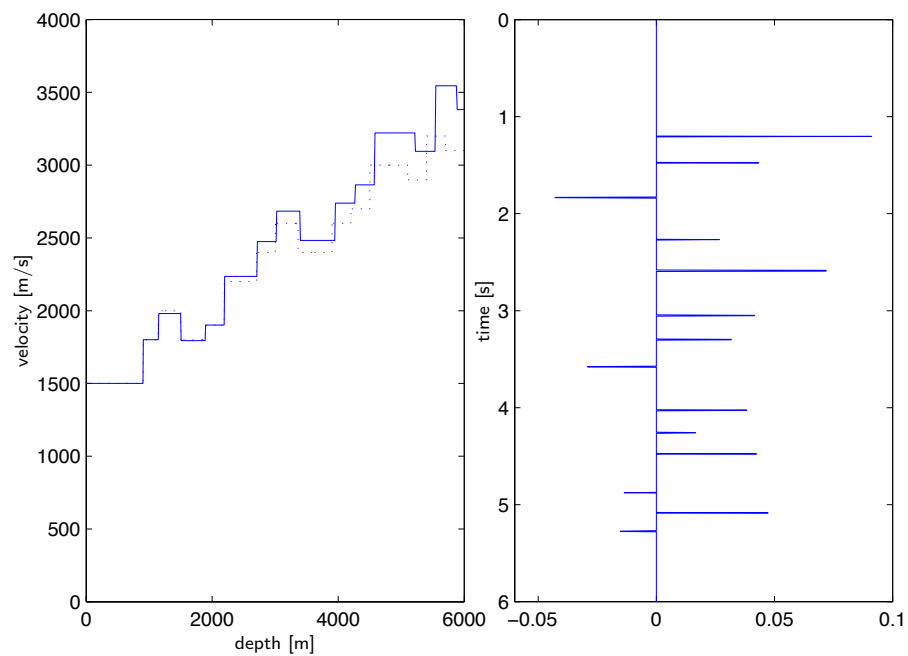


Figure D.1: Velocity model (dashed line) together with the calculated velocities (solid line). On the right the input upgoing wavefield before normalization.

Bibliography

- [1] Abubakar, A. and van den Berg, P. and Fokkema, J.T. *A feasibility study on nonlinear inversion of time-lapse seismic data*, Expanded abstracts SEG 2001, San Antonio, Texas, USA, September 9-14, 2001, pp. 1164-1167
- [2] Aki, K. and Richards, P. G. *Quantitative Seismology*, University Science Books, 1979
- [3] Berkhout, A.J. *Applied seismic wave theory*, Elsevier, 1987
- [4] Berkhout, A.J. *Seismic migration*, Elsevier, 1980
- [5] Bruckstein, A.M. and Levy, B.C. and Kailath, T. *Differential methods in inverse scattering*, SIAM J. Applied Math., 1983
- [6] Carrion, P.M. and Kuo, J.T. *A method for computation of velocity profiles by inversion of large-offset records*, Geophysics, 49, pp. 1249-1258, 1984
- [7] Cheney, M. *Inverse boundary-value problems*, American Scientist, 85, pp. 448-455, 1997
- [8] Claerbout, J. F. *Toward a unified theory of reflector mapping*, Geophysics, 36, pp. 467-481, 1971
- [9] Claerbout, J.F. and Muir, F. *Robust modeling with erratic data*, Geophysics, 38, pp. 826-844, 1973
- [10] Claerbout, J.F. *Fundamentals Geophysical Data Processing*, McGraw-Hill, 1976
- [11] Cohen, J.K. and Bleistein, N. *Velocity inversion procedure for acoustic waves*, Geophysics, 44, pp. 1077-1087, 1979
- [12] Cohen, J.K. and Bleistein, N. *Direct inversion procedure for Claerbout's equations*, Geophysics, 44, pp. 1034-1040, 1979
- [13] Diebold, J.B. and Stoffa, P.L. *The traveltime equation, tau-p mapping, and inversion of common midpoint data*, Geophysics, 46, pp. 238-254, 1981

[14] Dillen, W.P. *Time-lapse seismic monitoring of subsurface stress dynamics*, , Ph.D. thesis, Delft University of Technology, Delft, 2000

[15] Duncan, G. and Beresford, G. *Median filter behaviour with seismic data*, Geophysical Prospecting, 43, pp. 329-345, 1995

[16] Fokkema, J.T. and Dillen, M.P. and Wapenaar, C.P.A. *A proposal for 4D seismic imaging*, 59th mtg., Eur. Assoc. Expl. Geophys., Extenden Abstracts, session B041, 1997

[17] Fokkema, J.T. and van den Berg, P.M. *Seismic applications of acoustic reciprocity*, Elsevier, Amsterdam, 1993.

[18] Fokkema, J.T. and Smit, R. and Wapenaar, C.P.A. *Velocity replacement techniques in inhomogeneous media*, Delphi Consortium, 9, 1998

[19] Habashy, T.M. and Mittra, R. *On Some Inverse Methods in Electromagnetics*, Journal of Electromagnetic waves and Applications, 1, pp. 25-58, 1987

[20] Kennett, B.L.N. *Seismic wave propagation in stratified media*, Cambridge University Press, 1983

[21] Koster, J.K. *A direct layer-stripping approach to the inversion of marine seismic data*, Ph.D. thesis, Delft University of Technology, Delft, 1991

[22] Leyds, F.B. and Fokkema, J.T. *A Discrete-time inverse scattering algorithm for plane wave incidence in a one-dimensional inhomogeneous acoustic medium*, Geophysical transactions, 33, pp. 69-87, 1987

[23] Lumley, D.E. *Time-lapse seismic reservoir monitoring*, Geophysics, 66, pp 50-53, 2001

[24] Morse, P.M. and Feshbach, H. *Methods of theoretical physics*, McGraw-Hill Book Co., New York, 1953

[25] Raz, S. *Direct reconstruction of velocity and density profiles from scattered field data*, Geophysics, 46, pp. 832-86, 1981

[26] Reiter, E.C. and Toksoz, M. N. and Purdy, G. M. *A semblance-guided median filter*, Geophysical Prospecting, 41, pp. 15-41, 1993

[27] Schur, I. *Über Potenzreihen, die in innern des einheitskrises beschränkt sind*, J. für die reine und angewandte mathematik, vol. 147, pp. 205-232, 1917

[28] Sen, M. and Stoffa, P.L. *Global optimization methods in geophysical inversion*, Elsevier, 1995

- [29] Smit, R. *Homogenization through velocity replacement in acoustic media*, Msc. thesis, TU Delft, 1998
- [30] Stoffa, P.L. and Buhl, P. and Diebold, J.B. and Wenzel, F. *Direct mapping of seismic data to the domain of intercept time and ray parameter-A plane-wave decomposition*, Geophysics, 46, pp. 255-267, 1981
- [31] Tarantola, A. *Linearized inversion of seismic reflection data*, Geophysical Prospecting, 32, pp. 998-1015, 1984
- [32] Tarantola, A. *Inversion of seismic reflection data in the acoustic approximation*, Geophysics, 49, pp. 1259-1266, 1984
- [33] Treitel, S. and Lines, L. and Ruckgaber, A. *Geophysical inversion and applications*, Society of Exploration Geophysicists, 1993
- [34] Van den Berg, P.M. and van Broekhoven, A.L. and Abubakar, A. *Extended contrast source inversion*, Inverse Problems, 15, pp. 1325-1344, 1999
- [35] Van Borselen, R.G. *Removal of Surface-Related Multiples from Marine Seismic Data*, Ph.D. Thesis, Delft University of Technology, Delft, 1995
- [36] Wapenaar, C.P.A and Dillen, M.W.P. and Fokkema, J.T. *Applying one-way reciprocity theorems in time-lapse seismic imaging*, J. Seism. Expl., 10, pp. 165-181, 2002
- [37] Wapenaar, C.P.A. and Grimbergen, J.L.T. *Reciprocity theorems for one-way wavefields*, Geophysical Journal Int., 127, pp. 169-177, 1996
- [38] Weglein, A.B. and Secrest, B.G. *Wavelet estimation for a multidimensional acoustic or elastic earth*, Geophysics, 55, pp. 902-913, 1990
- [39] Yagle, A.E. and Levy, B.C. *Application of the Schur algorithm to the inverse problem for a layered acoustic medium*, J.Acoust.Soc.Am, 76, pp.301-308, 1983
- [40] Yagle, A.E. and Levy, B.C. *The Schur algorithm and its applications*, Tech. Rep. Lab. for Information and Decision Systems and the Dept. of Electrical Engineering and Computer Science, Mass. Inst. of Tech., 1984

Summary

Slicing the Earth:
A layer-stripping method employing a causality-based imaging condition.

Hedi Poot

During the last decades many different seismic inversion algorithms have been developed. Since the problem to be solved is non-linear and does not have a unique solution, every method makes use of its own approximations and assumptions. As a step towards a new approach to the inversion of seismic data we have designed and partly implemented a layer-stripping method applicable to laterally varying media that does not require a priori model information and determines the velocity properties of the subsurface directly from the input data.

The derivation of the three-dimensional layer-stripping method is based on the combination of a layer replacement method based on the reciprocity theorem and an imaging condition based on causality. The imaging condition expresses the relationship between the up- and downgoing wavefields just above an interface and the contrast over this interface. In the derivation of the imaging condition we make use of the boundary conditions over the interface and the principle of causality. For this reason the imaging condition is only valid for the short interval of time that there are no upgoing waves beneath the interface, in other words for the lapse of time before the downgoing waves beneath the interfaces have reached other interfaces and have had time to be reflected. Using the causality condition we can determine the propagation velocity in a virtual horizontal layer thin enough to justify the assumption that the velocity in the layer is varying only in horizontal direction. Using the reciprocity theorem we can express the acoustic wavefields in a certain state to the acoustic wavefields in a state with a different medium configuration. In our case we define one state to be the actual state and the second state to have the same configuration except for the top thin layer which is removed and replaced by a layer with known, homogeneous background velocity. When we start with the measured wavefields at the surface, which can be decomposed in an upgoing and a downgoing

part, we can apply the imaging condition and determine the velocity in the top virtual layer. By using the reciprocity theorem we can remove this layer, replace it by a layer with homogeneous background velocity and determine the wavefields below this layer. Now we can repeat the procedure by applying the imaging condition again and stripping the layers until the desired velocity profile is found. We have derived the theory for the three-dimensional, laterally varying case and simplified it for the two- and one-dimensional case.

We have first implemented the theory for the one-dimensional case. Accurate results were obtained for different one-dimensional earth models by using the energy of the wavefields in the imaging condition. We have shown that the width of the stripped layer is related to the measurement time step and that the resolution of the method depends mainly on the bandwidth of the data. The internal multiples in the data are handled correctly. We have shown that accurate results can be obtained as well for oblique angles of incidence. We have compared the method to an other layer-stripping method, the Schur algorithm, which is applicable only to horizontally layered media. We have shown that our method gives a more stable imaging result, especially in the presence of noise. Our layer-stripping method was applied to an example of a time-lapse seismic problem. The method has potential to be applied in order to quantitatively determine the difference in the properties of a reservoir between two measurements separated by a lapse of time. We have applied the method to a laterally varying earth model by using common-midpoint techniques. The implementation of our method for the full laterally varying case still remains to be performed.

The limited bandwidth of seismic data is a limiting factor when directly trying to determine the velocity profile of the subsurface. The spectral information of this profile contains low wavenumber components which can only be recovered when the data contains all low frequencies, which is not the case for seismic data. We have proposed a solution method for this problem by taking the absolute value or envelope of the data. Good results are obtained by applying this method when the events in the data are not overlapping. When taking the absolute value or envelope of the data, the events in the data loose their sign. In order to compensate for this we developed a method using median filters that determines the sign of the event before taking the absolute value or envelope and then applies this sign to the all positive result.

We can conclude that promising results have been obtained by designing and partly implementing a completely data driven inversion method which is theoretically applicable to laterally varying media.

Nederlandse Samenvatting

De aarde in plakjes:

Een laag-afpelmethode, gebruik makend van een beeldvormingsvoorwaarde gebaseerd op causaliteit.

Hedi Poot

Gedurende de laatste decennia zijn veel verschillende seismische inversie methodes ontwikkeld. Omdat het hier gaat om een niet-lineair probleem dat geen unieke oplossing heeft, maakt iedere methode gebruik van zijn eigen aannames en benaderingen. Als een stap in de richting van een nieuwe aanpak van inversie van seismische data hebben we een laag-afpelmethode ontwikkeld en deels geïmplementeerd die toepasbaar is op lateraal varierende media, waarvoor geen voorkennis over de ondergrond benodigd is en waarmee direct de snelheidparameters in de ondergrond kunnen worden bepaald uit de gemeten data.

De afleiding van de driedimensionale afpelmethode is gebaseerd op een combinatie van een methode om een laag te vervangen door een ander medium gebaseerd op het reciprociteitstheorema en een beeldvormingsvoorwaarde (imaging condition) die gebaseerd is op causaliteit. De beeldvormingsvoorwaarde bepaalt de verhouding tussen de op- en neergaande golfvelden vlak boven een grensvlak en het snelheidsscontrast over dit grensvlak. In de afleiding van de beeldvormingsvoorwaarde wordt gebruik gemaakt van de randvoorwaarden over het grensvlak en het principe van causaliteit. Om deze reden is de beeldvormingsvoorwaarde alleen geldig in het tijdsinterval waarin er nog geen opgaande golven onder het grensvlak zijn, in andere woorden voor het tijdsinterval waarin de neergaande golven onder het grensvlak nog geen andere reflecterende grensvlakken hebben bereikt. Gebruik makend van de beeldvoormingsvoorwaarde kunnen we de voortplantingssnelheid bepalen in een virtuele horizontale laag die dun genoeg is om te kunnen aannemen dat de materiaaleigenschappen van deze laag alleen varieren in horizontale richting en niet in verticale richting. Met behulp van het reciprociteitstheorema kunnen we de akoestische golfvelden in een bepaalde staat relateren aan de akoestische golfvelden in een andere staat met een andere mediumconfiguratie. In dit geval definieren we een

staat die overeenkomt met de ware situatie en een staat waarin de bovenste dunne laag is vervangen door een laag met een bekende en homogene voortplantingssnelheid. Beginnend met de gemeten velden op het aardoppervlak, die kunnen worden opgedeeld in een opgaand een neergaand gedeelte, kunnen we de beeldvormingsvoorwaarde toepassen en de snelheid in de bovenste virtuele laag bepalen. Door het reciprociteitstheorema toe te passen kunnen we deze bovenste laag verwijderen en vervangen door een laag met homogene achtergrondsnelheid en de golfvelden vlak onder deze laag bepalen. Nu kunnen we de hele procedure herhalen en de lagen één voor één afdelen totdat we het gewenste snelheidsprofiel hebben gevonden. We hebben de theorie afgeleid voor het driedimensionale, lateraal varierende geval en hebben het vereenvoudigd voor het tweedimensionale geval, het tweedimensionale, horizontaal gelaagde geval en tenslotte voor het ééndimensionale geval.

De theorie voor het ééndimensionale geval is als eerste geïmplementeerd. Nauwkeurige resultaten zijn behaald voor verschillende ééndimensionale ondergrondsmodellen door de energie van de golfvelden in de beeldvormings voorwaarde te gebruiken. We hebben laten zien dat de dikte van de afgelde laag verband houdt met de tijdstap van de metingen en dat de resolutie van de methode voornamelijk afhangt van de bandbreedte van de data. De interne meervoudige reflecties in de data worden op de juiste manier behandeld. We hebben laten zien dat er ook nauwkeurige resultaten kunnen worden behaald voor schuine hoeken van inval. De methode is vergeleken met een andere laag-afpelmethode, het Schur algoritme, dat alleen toepasbaar is op horizontaal gelaagde media. We hebben aangetoond dat onze methode een stabieler resultaat geeft, vooral in de aanwezigheid van ruis. Onze afpelmethode is toegepast op een 'time-lapse' probleem. De methode heeft potentieel om toegepast te worden om de kwantitatieve veranderingen in een reservoir te bepalen, die zijn ontstaan tijdens een bepaalde tijdsspanne. Dit wordt gedaan met behulp van twee verschillende metingen, gescheiden door die tijdsspanne. We hebben onze methode ook toegepast op een lateraal varierend ondergrondsmodel met behulp van common-midpoint technieken. De implementatie van de methode voor het meer-dimensionale, lateraal varierende geval dient nog te worden uitgevoerd.

De beperkte bandbreedte van seismische data is een limiterende factor wanneer er geprobeerd wordt direct uit de data het snelheidsprofiel van de ondergrond te bepalen. De spectrale informatie van dit profiel bevat kleine golfgetal componenten, die alleen kunnen worden bepaald als er ook laag frequente informatie in de data zit. Dit is echter niet het geval voor seismische data. We hebben een methode voorgesteld om dit probleem om te lossen door middel van het nemen van de absolute waarde of omhullende van de data. Goede resultaten zijn behaald door deze methode toe te passen zolang de events in de data elkaar niet overlappen. Als de

absolute waarde of omhullende van de data wordt genomen verliest de data haar teken, alles heeft dan een positieve waarde. Om dit te compenseren hebben we een methode ontwikkeld die gebruik maakt van mediaan filters. Met deze methode wordt het teken van een event bepaald voordat de absolute waarde of omhullende wordt genomen en dit teken wordt dan toegepast op het geheel positieve resultaat.

We kunnen concluderen dat veelbelovende resultaten zijn behaald met het ontwerpen en deels implementeren van een volledig data-gedreven methode die theoretisch toepasbaar is op lateraal varierende media.

Acknowledgments

This research was conducted at the faculty of Applied Earth Sciences, section of Applied Geophysics of the TU Delft. I have always enjoyed being a member of this section and would like to thank everyone, student or staff, who has been or still is part of this section for their input.

There are some people I would like to thank in particular:

Jacob Fokkema, for giving me the opportunity to perform this research in combination with my rowing career, for accompanying me in the process in his own pleasant way and for creating the scientific basis for this research.

Kees Wapenaar, for taking over Jacob's role in the middle of the research, for the indispensable input and advice, for the thorough reading of the thesis and for never raising an eyebrow on my strange rowing habits and working hours.

My parents, for their unconditional faith.

Curriculum Vitae

PERSONAL

Name Hedi Poot
Born December 16, 1975, Vlaardingen, the Netherlands
Nationality Dutch

EDUCATION

1987 - 1993 Stedelijk Gymnasium, Schiedam

1993 - 1998 Technische Universiteit Delft, the Netherlands
Mijnbouwkundig ingenieur (MSc in Mining)
Part of the research for Msc. thesis was performed at UT Texas,
Austin, USA
Msc. thesis: *2D Finite Difference modelling for Georadar*

1998 - 2004 Delft, University of Technology, The Netherlands
Departement of Applied Earth Sciences
PhD research: *Slicing the Earth: A layer-stripping method
employing a causality-based imaging condition*
Part of the research project was performed part-time due
to rowing at international level.

EMPLOYMENT

2004 - NWO (the Netherlands organization for Scientific Research)
Program coordinator computer science